# 論文 / 著書情報
# Article / Book Information

| | |
|---|---|
| 題目(和文) | |
| Title(English) | A METHOD FOR ESTIMATION OF 2D LAYERED MEDIUM BY A SIMPLE LINEAR ARRAY IN MICROTREMOR WAVEFIELD |
| 著者(和文) | Zhang Xin-rui |
| Author(English) | Zhang Xin-rui |
| 出典(和文) | 学位:博士（学術）,<br>学位授与機関:東京工業大学,<br>報告番号:甲第9901号,<br>授与年月日:2015年3月26日,<br>学位の種別:課程博士,<br>審査員:盛川　仁,翠川　三郎,古谷　寛,松岡　昌志,山中　浩明 |
| Citation(English) | Degree:,<br>Conferring organization: Tokyo Institute of Technology,<br>Report number:甲第9901号,<br>Conferred date:2015/3/26,<br>Degree Type:Course doctor,<br>Examiner:,,,, |
| 学位種別(和文) | 博士論文 |
| Type(English) | Doctoral Thesis |

**DOCTOR THESIS:**

# A METHOD FOR ESTIMATION OF 2D LAYERED MEDIUM BY A SIMPLE LINEAR ARRAY IN MICROTREMOR WAVEFIELD

Feb. 13, 2015

Interdisciplinary Graduate School of Science and Engineering
Built Environment
Morikawa Laboratory ZHANG Xin-rui

**Abstract**

In geological survey using microtremor, array method is popular for its low cost and simple data process. However, it is practically difficult to satisfy the strict array shape required by array methods like spatial auto-correlation (SPAC) method. On the other hand, in order to detect a 2-D profile, array methods are unavailable and it always requires an enormous cost, many sensors and complicated post process, using other methods like refraction microtremor (ReMi) method. Herein, we proposed a method using very simple array shape, a linear array with 3 sensors as the least requirement, which is able to give an estimation of 2-D layered medium with simple post-process. This method is based on the basic concept of SPAC method and the seismic interferometry (SI) theory. The availability and effective scope is confirmed and discussed using both the numerical simulation by finite difference method (FDM) and the field tests.

# Table of Contents

# List of Figures

# List of Tables

# 1

# Introduction

## 1.1 Review of past research

### 1.1.1 Research about the microtremor survey

Local amplification due to the irregularities of ground structure close to ground surface is very significant in large earthquake motion. In order to mitigate the damage caused by earthquake, the upper-ground structure needs to be designed carefully according to the seismic characteristics of the under ground structure below it because different ground structure would cause different site response. That claims the demand to estimate the ground structure, or S-wave velocity strucure as the main indicator used for engineering objectives. Compared to many high-cost methods like boring methods, refraction method, reflection method which either need active source or would cause permanent damage to the ground, methods using microtremor are very inexpensive and easy to conduct. Normally, the subsurface velocity structure is obtained from the phase velocity dispersion curve of surface wave such as Rayleigh wave and Love wave. [1, 2]

The frequency-wavenumber spectral (f-k) method [3] has been a very popular tool for the estimation of phase velocity, it can decompose a wavefield in the frequency-wavenumber domain and detects the power of each wave component. It does not demand certain strict shape of arrays but usually requires quite many sensors arranged 2D dimentionally. Similar is for semblance analysis method [4, 5].

The horizontal-to-vertical spectral ratio (H/V) method has been proposed by Nakamura [6], which has opened a new perspective in microtremor survey. Under the simple assumption that (1) The spectral ratio of horizontal and vertical component at the base layer is zero; (2) only local sources contribute to the microtremor. The ratio between horizontal and vertical Fourier function at the surface has been used as the indication of the site effect, thus can be applied to estimate the corresponding S-wave velocity structure of the underground structure. To be exact, this ratio is interpreted as representing the S-wave amplification factor directly. Also, it has been explained as the Rayleigh wave ellipticity [7–9]. The significance of the ratio, especially the amplitude, is still under discussing and cannot be interpreted very well.

After Aki [10] proposed the spatial auto-correlation (SPAC) method, the long history of over 50 years of array method's development has begun. He proposed a totally different approach to estimate phase velocity of Rayleigh wave. All the information about the ground structure is summarized into one quantity called the azimuthal average of the spatial autocorrelation function. Using mathematical tools, this quantity is equal to a very simple form, the zero order of first kind of Bessel function $J_0$. Hence, it becomes very convenient to do the post-process about observation records and develop an inversion technique to obtain the phase velocity $v$ from it. It requires a circular array of evenly spaced sensors and a central sensor [11].

After that, Henstridge reformulated Aki's theory using a spectral representation and attempted to develop a more general theory which regards Aki's theory as a special case [12]. Based on it, Cho et al. [13, 14] improved this concept of Henstridge and developed a more systematic and comprehensive framework about estimating Love or Rayleigh phase velocity using three-component records of microtremors from a circular array of sensors. And this theory directly gave the birth to the centerless circular array (CCA) method. The CCA method improves the resolution limit of the original SPAC method and is more accurate in estimating phase velocity in long wavelength range. There are also many other research about the extension of the orignal circular array [15–17].

However, both CCA method and SPAC method requires a strict circular array shape which is, after all, not practical in real observation situation especially in urban area. In order to make the observation more convenient and slacken the strict requirement of the array shape, much reseach have been done [18–27].

Morikawa et al. [18] proposed a “2-site” SPAC method which emphasized that it is available to do the observation between any pair of the center site and the site on the circle individually, that it, there is no need to do the observation at all sites simultaneously. This method decreases the cost and make the observation more flexible. The L-array shape method is also proposed by many reseachers.

In Hayashi and Kita’s work [23], it is mentioned that the L-shaped array in which angle is less than 90 degrees is much better than that is larger than 90 degrees. However, it is still difficult to decide in a particular observation situation the direction and the angle of the L-shape array. This theory even requires the distribution of the wave to be large. Nevertheless, it is still using the original and old concept from SPAC method but discussing the new kind of estimation error. Moreover, it fails to explain the case that the wave power at one paricular direction is dominating the wavefield.

The validity of performing the SPAC method with a linear array has been discussed but the conclusion is empirical and is not backed by theory [28, 29]. In Chavez-Garcia’s theory, it is shown that in the isotropic wavefield (azimuth-independent), only 2-site is enough to estimate the phase velocity.

The possibility of performing ground survey using a linear array is also realized by using refraction microtremor (ReMi) method from Louie [19]. This method is developed from spectral analysis of surface wave (SASW) method proposed by Nazriana and Stokie [30] and the multichannel analysis of surface waves (MASW) method by Park et al. [31].This method is proud for not using active sources and its robustness against the presence of noise and full-wave. However, ReMi method uses refraction recording equipment, whose lower frequency limit is confined, and it uses much more sensors, which is over 12, than normal microtremor survey method to obtain redundant statistics. The phase velocity of Rayleigh wave is decided by picking the lowest velocity envelope. Hence, although this method uses simple form of array, we still consider it improvable because of the large number of sensors and the deficiency in mathematical basis. Be careful here that, though in terms of shape, ReMi method can be regarded as a linear array method here, substantially it applies both Rayleigh wave and refraction wave. Hence it is meaningless to compare ReMi method with microtremor method applying just Rayleigh or Love waves. We just put it here as part of the past research about microtremor method using simple shape.

In Hayashi and Kita's work about using a linear array [23], they demonstrated that the linear array can provide usable phase velocity when propagation direction of the microtremor is distributed at least the range of 120 degrees. However, the same problem as in the L-shape discussion rises that it lacks a systematic theoretical support and starts from a wrong methodology. It also neglects the fact that one wave in certain azimuth may be dominating.

Another method, called the direct estimation method (DEM), has been proposed wherein the sensor arrangement is more flexible by Shiraishi et al. [24]. In DEM, a complex coherence function (CCF) has been used to constitute a new solution for estimating the phase velocity. However, DEM requires at least five sensors and they must be in a symmetrical arrangement. In his research, the CCF is clearly used to describe the error caused by the finite number of sensors in the circular array, the spatial aliasing error. which can be applied both in linear array and L-array shape method above.

### 1.1.2 Assumptions required by microtremor survey method

As described in some papers [32, 33], the assumption about the wavefield effective for conducting microtremor survey method has always been a controversy. Normally, the wavefield is regarded as a random field that is stationary in both time and space. The waves arriving from different directions are mutually uncorrelated and they normally consist of Rayleigh plane wave in the vertical direction.

As a whole, we introduced mainly about array methods above, the objective of microtremor array method is to obtain the dispersion curve and estimate the S-wave velocity structure. All the theories are based on the assumption that the structure is 1-D structures, even if they, the array methods, are performed using 2-D array [34]. However, site effect is complicately affected by the complexity of ground structure, which claims the urgent need to obtain more detailed estimation about the ground structure. Chavez-Garcia et al. [35] summarize that:

> All their inversion allows determining a local 1D model, 2D and 3D structures may then be reconstructed from the interpretation of several 1D profiles.

For non-2D-array methods like H/V method, of course, if we assume the ground structure under each site as a 1D structure, we can obtain the final structure as as 3D structure using some interpolation techniques among those sites. Hence, it can be concluded that either there is no way to estimate a 3D ground structure by array methods or it requires too many sensors and still based on approximate assumptions, which is assuming 1D structure at each site and constiture 3D finally, by methods like f-k or H/V method. Matsushima [36]claims the necessity of developing a conceptual framework about the dependence of H/V method on the lateral heterogenity in a 2D model and has done numerical simulations to confirm that. However, it still only emphasizes the point that there exists influence of the heterogeneity on the H/V spectral ratio. It does not go further on its significance on the estimation of ground structure based on a simple 2D model. In addition, there is still little similar discussion about the array methods like SPAC methods and its extensions.

For microtremor survey method like SPAC methods, they are mostly used to infer phase velocity of Rayleigh waves on the basis of vertical motion records alone. Tada et al. [37] mentions that SPAC method also provides the possibility of infering phase velocities of Love wave using horizontal components. Aki [10] failed to show how to extract out the love wave phase velocity when both types of waves are present. Okada and Matsushima [38], Matsushima and Okada [39] found the way of inferring it using a nonlinear system but it has too many unknowns and requires much effort to minimize the aggregate misfit of the nonlinear equations. Morikawa provide more general representatio than Matsushima and Okada. Tada et al. [37] proposed a simple methodology using circular-array microtremor techniques to infer the velocity independently using just horizontal components. There are other researches about this topic [15, 16]. The application of horizontal components have the potential, of course, to be efficiently used to infer the Love wave while it is quite complicated to seperate two kinds of waves, which are Rayleigh and Love waves, in the horizontal components. Tada et al. [41] mentioned the two-radius circular array method [40], which also applies the horizontal component around two circles of different radii using a technique to cancel out the Rayleigh wave. However, all the five circular array methods discussed in the paper are still all based on the assumption of using only vertical components. That is because vertical component only includes the Rayleigh wave so as to save lots of effort to consider the procedure related with Love waves and decrease the error possibly caused by that. There is another advantage of considering only vertical component is that for a sensor in practical observation, it is more possible to have horizontal channel broken down because there are two horizontal channels out of all three. Using just vertical component decreases this risk and is thus convenient.

As described in Yokoi's work [42], an assumption which is always used by SPAC related methods is that the fundamental mode of Rayleigh/Love wave dominates in the microtremor wavefield. After Aki [10], Henstridge's theory [12] about SPAC method is also based on the strong assumption of dominance of fundamental mode before Cho et al. [13,14] modified and reconstituted Henstridge's theory to situations where higher modes of Rayleigh/Love wave are present [12]. Actually, it is necessary to consider the influence caused by the higher modes. [43, 44]. It is obvious that if higher modes together with the fundamental one can be totally identified and estimated, more accurate dispersion curve about the real fundamental mode of phase velocity can be obtained and thus more convincing S-wave velocity structure can be reckoned as well as the safer structure design. In Feng et al.'s work [45], it lifts an assumption that the dispersion curve indicates one particular mode which has the biggest amplitude at each frequency. However, the complexity of the multimode shows the possibility that the dispersion curve sometimes migrates from one mode to another mode. There are also other researches about this topic [44,46]. However, it is difficult to reach at a consensus about the optimal extraction of different mode. In Yokoi 's work [42], he proposed a new prospective about dealing with the multimode case from a view of seismic interferometry (SI). Yokoi concluded that this new methodology (dual-mode inversion) shows a better performance about the estimation than the conventional method, which considers the fundamental mode only. However, by observing the two cases of inversion result in Yokoi's work, it is difficult to say the multi-mode is obviously better despite the high cost of calculation.

### 1.1.3 Research about the seismic interferometry, its consistency with microtremor methods and its new applications

The Green's function between two points A and B means the response at A when a unit impulse force is exerted at B. The use of random noise to constitute the Green's function has been a hot research topic. Weaver and Lobkis [47] have demonstrated how to apply the diffuse thermal noise at two ultrasonic transducers to obtain the Green's function between them two. Then, the cross correlation process was investigated from the perspective of multiple uncorrelated sources regarded as noise by Campillo and Paul [48]. Wapenaar's reseach [49] sums up all the contributions from sources and the correlation is shown to contain the causal and acausal Green's function. In elastodynamic cases, similar conclusions have been drawn (Wapenaar and Fokkema [50], Sanchez-Sesma et al. [51–53], Snieder [54], Perton [55]). These theories are simply summarized as seismic interferometry (SI).

The consistency between the SI and SPAC method has been shown by Yokoi and Margaryan's work [32]. Moreover, Yokoi [42] successfully applied this characteristic to discuss about the multimode inversion based on Rayleigh wave. The SPAC method can be interpreted as an extension of SI in the long-wavelength range. This relationship is valid under the assumption that the wavefield is a moderately azimuth-dependent wavefield which contains mainly surface wave, namely, not a extreme one. Yokoi and Margaryan [32] also proposed the possiblity of exploration of 2D and 3D ground structures using the discoveries about the relationship between SPAC method and SI, which includes the Green's function indicating the intrinsic property of horizontally/unhorizontally ground structure. There is also other researches about this topic [56].

The consistency of SI and H/V method has also been researched [33]. In the article [33], the Horizontal-vertical spectral ratio is reinterpreted using the ratio between the corresponding imaginary part of Green's function (IOG). This theory is based on the assumption of a diffuse wavefield containing all kinds of wave [55]. Hence though there is many different wavefield assumption for the H/V method itself in different research about it, it seems reasonable to make a common available wavefield effective for both H/V method and SI. Moreover, this theory is confirmed by numerical simulation and field tests. Although in the article [33], horizontally layered medium is assumed, the availability of this concept is actually for any inhomogeneous and anisotropic medium.

Matsushima et al. [36] applied the same concept to explore the applicability of the diffuse field concepts to detect the lateral heterogeneity using microtremor data. Similar as in Sanchez-Sesma et al.'s work [53], it is further said that although the real wavefield would not always satisfy very perfect conditions, the diffuse wavefield provides a unifying background for the combination of SI and microtremor methods like SPAC method and H/V method because it is not limited to 1D structure only. Acutually, in their paper, they applied this perspective to study the real H/V spectral ratio in a 2D model and drawn very significant conclusions about it. They used the spectral element method (SEM) or the finite difference method (FDM) to do study about the lateral heterogeneity in a 2D layered medium.

## 1.2 Objective of this thesis

The main objective of this thesis is: firstly, improve the existing array methods to solve the problem of too strict array shape in order to make the small-scale microtremor observation more convenient; secondly, to propose a very simple method, which extract the most potential of the spectral ratio among sites in small-scale observation, to estimate the 2-D layered medium. Hence, instead of using a large number of sensors with very strictly designed array shapes, we use very simple linear array to reach the same goal based on conventional theories. This research can be regarded as a very brief summary and combination of the essence of the most popular two methodologies in the last years, that is, microtremor array methods and sesimic interferometry. Mainly, our research is illuminated by Sanche-Sesma's research [33] and Shiraishi et al's research [24], which propose the possiblity of making the most use of both SI and CCF. Matsushima et al. [36] carry out similar study with mine about how to deal with the lateral heterogeneity using spectral ratios and SI. In my research, the vertical component, diffuse field, and the dominance of the fundamental mode of Rayleigh wave still works, which are supported by huge amount of researches mentioned above. More introductions and interpretations about these two main objectives will be described more detailedly in the background part of Chapters 2 and 3.

## 1.3 Structures of this thesis

As for the outline of this article, in Chapter 1, we reviewed the past researches of array methods of microtremor survey and seismic interferometry relating to microtremors, introduced the background, and the proposed position of our reseach, and described the objective of our research. There are two parts of basic research in our research which would be demonstrated in Chapters 2 and 3, respectively. We listed the reearch scope of my thesis that we would discuss the applicability of the new method in (1) 2-layerd medium; (2) with the fundamental mode of Rayleigh wave dominated; (3) under the assumption of diffuse and stationary wavefield.

In Chapter 2, we introduce the basic theory about complex coherence function (CCF) and pointed out the relationship between it and original SPAC method proposed by Aki [10]. Then, on the basis of CCF, we proposed the new method which allows using a very simple linear array to estimate the phase velocity of Rayleigh wave. We confirmed the availability using both numerical simulation and field tests. We also discussed the effective scope and compared this method with the $J_0$ method, which is a simplified SPAC method using only two sites without taking azimuthal average as shown in works by Chavez-Garcia et al. [28, 29].

In Chapter 3, we firstly introduce the basic theory about seismic interferometry and emphasized the significance of appling the IOG to identifying the lateral heterogeneity. Then, we discussed the influence of the lateral heterogeneity on IOG and the sensitivity of imaginary part of Green's function (IOG) relative the lateral heterogeneity, which makes the base of the inversion technique to estimate the 2D lateral heterogeneity. After that, numerical simulation would be done to simulate a diffuse wavefield to observe whether the methodology would work.

In Chapter 4, we would combine the results of Chapters 2 and 3 to constitute a comprehensive methodology to range estimate a 2-D 2-layered medium using a linear array with a few sites. We would complete and improve the technique of doing range estimation and apply it to the numerical simulation by finite difference method (FDM) to confirm the availability.

In Chapter 5, we would make a final conclusion about all done in this thesis.

# 2

# A method to estimate the phase velocity of Rayleigh wave using a simple linear array

## 2.1 Background

In order to estimate earthquake ground motion, it is necessary to estimate the ground structure by geophysical exploration. In the field of geophysical exploration, the extensive use of array methods has been done by employing microtremors because they provide an inexpensive means of inferring the phase velocity of surface waves. Among those methods, the frequency-wavenumber (f-k) spectral method [2, 3] and the semblance analysis [4, 5] both require a rather large number of sensors to be set two-dimensionally although their arrangement can be designed freely to some extent.

In the spatial auto-correlation (SPAC) method [10, 11, 14], all the whole information on the wavefield is integrated into a single quantity, which is called the azimuthal average of the spatial autocorrelation function. Its theory is easy understanding and it requires fewer sensors than the f-k method or a semblance analysis. Normally, we analyse records from a circular array of evenly spaced sensors on a circle and a central sensor. However, the strict arrangement of the sensors is difficult to realise especially in urban areas. Research has been done in order to reduce the restriction of the sensor arrangement [24, 28, 29, 37].

The validity of performing the SPAC method with a linear array has been discussed but the conclusion is empirical and is not backed by theory [28, 29]. Another method, called the direct estimation method (DEM), has been proposed wherein the sensor arrangement is more flexible [24]. In DEM, a complex coherence function (CCF) has been used to constitute a new solution for estimating the phase velocity. However, DEM requires at least five sensors and they must be in a symmetrical arrangement. The possibility of performing ground survey using a linear array is also realized by using refraction microtremor (ReMi) method [19]. This method is proud for not using active sources and its robustness against the presence of every kind of wave including microtremor and body waves. However, ReMi method uses refraction recording equipment, whose lower frequency limit is confined, and it uses much more sensors, which is over 12, than normal microtremor survey method to obtain redundant statistics. The phase velocity of Rayleigh wave is decided by picking the lowest velocity envelope. Hence, although this method uses simple form of array, we still consider it improvable because of the large number of sensors and the deficiency in mathematical basis. Moreover, though in terms of shape, ReMi method can be regarded as a linear array method here, substantially it applies both Rayleigh wave and refraction wave. Hence it is meaningless to compare ReMi method with microtremor method applying just Rayleigh or Love waves. We just put it here as part of the past research about microtremor method using simple shape.

On the other hand, we herein propose a technique based on the CCF for estimating the phase velocity of Rayleigh wave. With the help of a genetic algorithm (GA) [57], the phase velocity of Rayleigh wave can be estimated from the CCFs among the sensors in a line, that is, linear array. This makes the arrangement of the sensors easier. Besides, because this method is based on the concept of SPAC method, it has the potential to estimate deeper structure using just fewer sensors and with firmer theoretical basis than ReMi method.

The technique is unavailable when the microtremor is uni-directional (all the wave power comes from only one direction from remote place) and perpendicular to the linear array. This is obvious because in this case the microtremor field cannot produce phase difference between any pair of sites in the linear array. However, in real cases, there is barely extreme case like that. In most cases, only one linear array is enough to estimate Rayleigh wave phase velocity regardless of the azimuth-dependence of the microtremor field. On the other hand, this technique, of course, works in the isotropic wavefield. For SPAC method without taking azimuthal average, using only 2 sites can also obtain acceptable accuracy in the isotropic wavefield [28, 29, 32] but it does not work in the case where the wavefield has some azimuth-dependent component. Hereafter, we call this simplified SPAC method $J_0$ method. However, by using 3 sites on a line in the proposed method, phase velocity can be estimated well even in moderately azimuth-dependent wavefield. Hence, though the proposed method is not as perfect as the original SPAC method, it is expected to have more simple and convenient sensor arrangement and have robustness against azimuth-dependent wavefield to certain extent.

We carry out necessary numerical simulations to demonstrate that (1) this technique works as long as the wavefield is not a strong azimuth-dependent one; (2) it works even in some cases of extremely azimuth-dependent wavefield. The availability of the SPAC method without taking average was also discussed as comparison. Furthermore, we confirmed the availability of this technique using data from a field test.

## 2.2 Theoretical background

In this section, we firstly interpret the concept of the CCF first. Then, we demonstrate, in theory, how to estimate the phase velocity of Rayleigh waves from the records of linear arrays by applying CCFs among sensors in a line.

### 2.2.1 SPAC method

The SPAC method is firstly proposed by Aki [10] to estimate phase velocity of Rayleigh wave.

Most important condition for this method is that the microtremor wavefield is stationary in both time and space domain. Given an equilateral-triangle array and vertical components of microtremor data at four sites, we take the record at center site as $X(t, \overrightarrow{r_0})$ and record on another site on the circle as $X(t, \overrightarrow{r_0} + \overrightarrow{r})$. Using the fourier transformation,

$$X(t) = \int Z(\omega)e^{-i\omega t}d\omega = \int e^{-i\omega t}dZ(\omega) \tag{2.1}$$

$$\begin{aligned} X(t, \overrightarrow{r_0}) &= \iiint exp[-i\omega t - i\overrightarrow{k}\overrightarrow{r_0}]dZ(\omega, \overrightarrow{k}) \\ X(t, \overrightarrow{r_0} + \overrightarrow{r}) &= \iiint exp[-i\omega t - i\overrightarrow{k}(\overrightarrow{r_0} + \overrightarrow{r})]dZ(\omega, \overrightarrow{k}) \end{aligned} \tag{2.2}$$

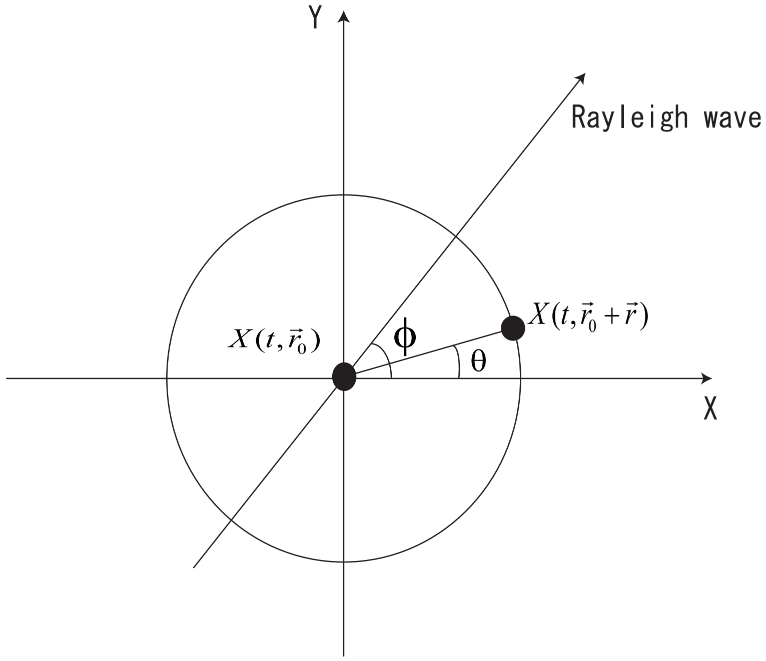


**Figure–2.1** A sketch map of observation using SPAC method.

in which $\overrightarrow{k}$ is the wavenumber vector $(k_x, k_y)$ and $\omega$ the circular frequency. $Z(\omega)$ is the fourier transform of $X(t)$.

Then we calculate the spatial auto-correlation:

$$
\begin{aligned}
&E[X^*(t, \overrightarrow{r_0})X(t, \overrightarrow{r_0} + \overrightarrow{r})] \\
&\quad = E[\textstyle\int\int\int \int\int\int exp[i\omega t + i\overrightarrow{k}\overrightarrow{r_0}]exp[-i\omega' t - i\overrightarrow{k}'(\overrightarrow{r_0} + \overrightarrow{r})]dZ^*(\omega, \overrightarrow{k})dZ(\omega', \overrightarrow{k}')]
\end{aligned}
\tag{2.3}
$$

where the $*$ means the complex conjugate. Because the wavefield is stationary, the below equation is satisfied.

$$
E[dZ^*(\omega)dZ(\omega')] = \begin{cases} E[|dZ(\omega)|^2], \omega = \omega' \\ 0, \omega \neq \omega' \end{cases} \tag{2.4}
$$

$$
E[dZ^*(\omega, \overrightarrow{k})dZ(\omega', \overrightarrow{k}')] = \begin{cases} E[|dZ(\omega, \overrightarrow{k})|^2], \omega = \omega' and \overrightarrow{k} = \overrightarrow{k}' \\ 0, otherwise \end{cases} \tag{2.5}
$$

Hence,

$$E[X^*(t,\overrightarrow{r_0})X(t,\overrightarrow{r_0}+\overrightarrow{r})] \\ = \iiint exp[-i\overrightarrow{k}\overrightarrow{r}]E[|dZ(\omega,\overrightarrow{k})|^2] \quad = \iiint exp[-i\overrightarrow{k}\overrightarrow{r}]h(\omega,\overrightarrow{k})d\omega d\overrightarrow{k} \tag{2.6}$$

where, $h(\omega,\overrightarrow{k})$ indicates the amplitude ratio and phase delay between the vertical and horizontal componets. Seeing the Fig. 2.1 , $\overrightarrow{k}=(k_x,k_y)=(kcos\phi,ksin\phi)$ so that $\overrightarrow{k}\overrightarrow{r}=krcos(\theta-\phi)$ and $d\overrightarrow{k}=kdkd\phi$ in which $r=|\overrightarrow{r}|$.

Then

$$E[X^*(t,\overrightarrow{r_0})X(t,\overrightarrow{r_0}+\overrightarrow{r})] \\ = \iiint exp[-ikrcos(\theta-\phi)]kh(w,k,\phi)d\omega dkd\phi \tag{2.7}$$

Then we create a variable as: $S(r,\omega,\theta)=\int_0^{2\pi} exp[-ikrcos(\theta-\phi)]kh(w,k,\phi)d\phi$
It is called power spectra.

Taking the azimuthal average of $S(r,\omega,\theta)$, we obtain $\bar{s}(r,\omega)$:

$$\bar{S}(r,\omega)=\frac{1}{2\pi}\int_0^{2\pi} S(r,\omega,\theta)d\theta \\ = \frac{1}{2\pi}\int_0^{2\pi} h(\omega,k,\phi)k\int_0^{\pi} exp[-ikrcos(\theta-\phi)]d\theta d\phi]. \tag{2.8}$$

For the center site, $r=0$ so that:

$$S(0,\omega,\theta)=\int_0^{2\pi} h(\omega,k,\phi)kd\phi \equiv S(0,\omega) \tag{2.9}$$

Finally, take the ratio of $\bar{S}(r,\omega)$ and $S(0,\omega)$, we obtain the so-called azimuthal-average of spatial auto-correlation coefficients:

$$\rho(r,\omega)=\frac{\bar{S}(r,\omega)}{S(0,\omega)}=\frac{1}{2\pi}\int_0^{\pi} exp[-ikrcos(\theta-\phi)]d\theta \\ = J_0(kr)=J_0(\frac{\omega r}{c(\omega)}) \tag{2.10}$$

where $c(\omega)$ indicates the phase velocity of Rayleigh wave and $J_0$ is the Bessel function of the first kind of order 0. Hence, after obtaining auto-correlation coefficients, we can calculate the phase velocity using certain reversion computation techniques.

Practically, when we use the simplest array shape of equilateral triangle with 3 sites on the circular and 1 site in the center as shown in Fig. 2.2, the azimuthal-average of spatial auto-correlation coefficients $\rho(\omega,r)$ can be calculated as:

$$\rho(\omega,r)=\frac{1}{3}\sum_{j=1}^{3}\frac{Re(S_{0j}(\omega))}{S_{00}(\omega)S_{jj}(\omega)}, \tag{2.11}$$

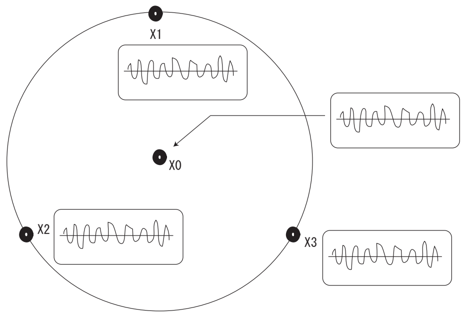


**Figure–2.2** Plan of sites.

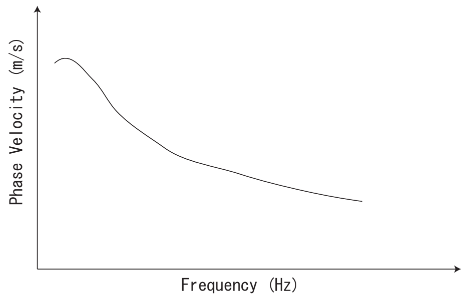


**Figure–2.3** Dispersion curve.

where $\omega$ and $r$ are the angular frequency and radius of the circular array, respectively. $S_{jj}(\omega)$ and $S_{0j}(\omega)$ are the power spectra of vertical component of microtremors at site $j$ ($j = 0, 1, 2, 3$) and the cross spectra of the vertical records between site $j$ and 0. The site 0 is center of the array and sites 1, 2, and 3 are located on the circle.

Practically, $S_{jk}(\omega)$ is obtained by the product of Fourier transformation of records at two sites as

$$S_{jk}(\omega) = F(\omega, X_j)F^*(\omega, X_k), \tag{2.12}$$

where $X_j$ is a location of site $j$ and $^*$ stands for the complex conjugate.

Afterwards, a dispersion curve can be obtained and the property of under-surface layers are estimated using the curve.

In order to demonstrate the simplest procedure to apply the SPAC method, see Fig.2.2, Fig.2.3, Fig.2.4. In Fig.2.2, the four sites $X0$, $X1$, $X2$, $X3$ are observed simultaneously and we obtain the corresponding records. Then, we apply Eq.(2.11) to calculate the dispersion curve as Fig.2.3 shows. Finally, using certain reversion computaion method [58], we obtain the S-wave velocity structure based on the assumption that the layers are horizontal.

The SPAC method interpreted here is the most basic form of it. Many reseachers including Chavez-Garcia et al. [29] and Morikawa et al. [18] has developed and discussed about this method in different ways. Besides, some researchers like Cho et al. [14] even enlarge and generalize Aki's theory [10]. However, here in my research, the details of SPAC method is not the point. Instead, we concentrate on the introduction of seismic interferometry into this method. Hence, knowing the easiest form and basic procedure of it is enough.

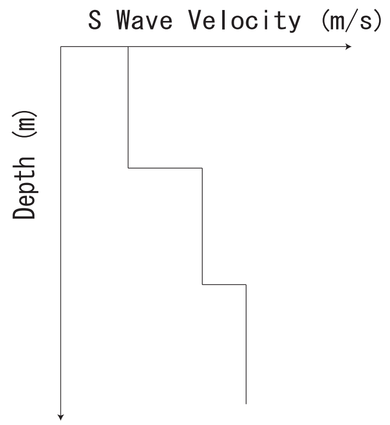


**Figure–2.4** S-wave structure estimated from the dispersion curve.

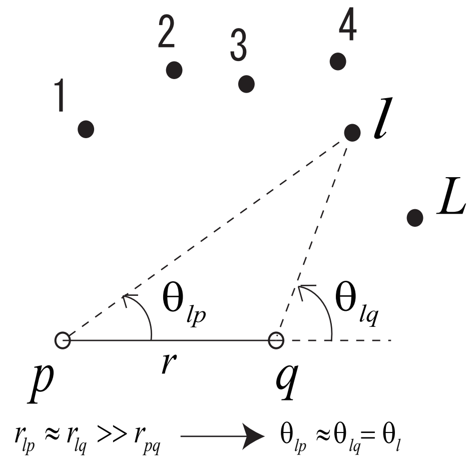


**Figure–2.5** Geometry used in the formulation of complex coherence function (CCF) between two sites p and q.

### 2.2.2 Discrete formula of CCF

Under assumptions: (1) Only the fundamental mode of Rayleigh waves is dominated in microtremors, and (2) Different sources are not correlated, the real part of the discrete formula for CCF can be expressed as [24]:

$$Re(\gamma_{pq}) = J_0(kr) + 2\sum_{n=1}^{\infty}\{(-1)^n J_{2n}(kr)\sum_{l=1}^{L}\lambda_l \cos 2n\theta_l\}, \tag{2.13}$$

in which $Re$ and $J_n$ denote the real part and the $n$th-order Bessel function with the 1st mode. $\gamma_{pq}$ is the CCF between sites $p$ and $q$. $r$ is the distance between sensors $p$ and $q$. $L$ is the number of wave sources. $\lambda_l$ is the rate of the contribution of the $l-$th wave source to the power spectra at the observation point and satisfies $\sum \lambda_l = 1$. $k$ is the wave number

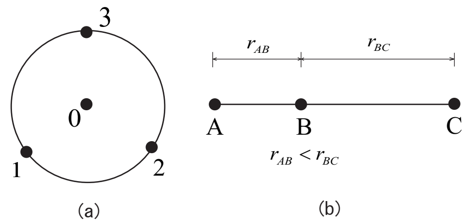


**Figure–2.6** Sensor arrangement of SPAC method and the new method. (a) Equilateral array in the SPAC method (b) Linear array with 3 sites on it.

and $\theta_l$ is the azimuth of the wave source $l$. These parameters are shown in Fig. 2.5.

In the conventional SPAC method [11], Eq. 2.11 is commonly used. $\rho(\omega)$ is the azimuthal average of the spatial autocorrelation coefficient. $S_{ll}(\omega)$ and $S_{0l}(\omega)$ are the power spectra of the vertical component of the microtremors at site $l$ ($l = 1, 2, 3$) and the cross spectra of the vertical records between site $l$ and 0, respectively. Site 0 is the center of the array, and sites 1, 2, and 3 are located on the circle as shown in Fig. 2.6(a). Here, $\frac{Re(S_{0l}(\omega))}{\sqrt{S_{00}(\omega)S_{ll}(\omega)}}$ is actually equal to $\gamma_{0l}$. By taking the azimuthal average, the Bessel functions of orders 2 and 4 of Eq. 2.13 vanish and the Bessel functions of orders larger than 6 are negligibly smaller than $J_0(kr)$ in the range of $kr < \pi$ so that only one term $J_0(kr)$ remains. Then, the phase velocity $c$, $c = \frac{\omega}{k}$, can be obtained using certain inversion techniques.

### 2.2.3 Proposal of a method using a linear array on the basis of the CCF

In the range of $kr < \pi$, the Bessel functions of orders larger than 6 can be ignored [24]. Hence, the real part of the CCF is expressed as:

$$\begin{aligned} Re(\gamma_{pq}) &\approx J_0(kr) - 2J_2(kr)\sum_{l=1}^{L}\lambda_l\cos 2\theta_l \\ &+ 2J_4(kr)\sum_{l=1}^{L}\lambda_l\cos 4\theta_l. \end{aligned} \tag{2.14}$$

In the SPAC method, as interpreted in the previous subsection, the second and third terms vanish when taking the azimuthal average so that the information on wave sources $\sum_{l=1}^{L}\lambda_l\cos 2\theta_{ln}$ and $\sum_{l=1}^{L}\lambda_l\cos 4\theta_{ln}$ do not need to be considered.

On the other hand, we let $\sum_{l=1}^{L}\lambda_l\cos 2\theta_l$ and $\sum_{l=1}^{L}\lambda_l\cos 4\theta_l$ remain and regard them as the second and third unknown variables to be estimated in addition to the phase velocity. It is impossible to solve them using just one single CCF. Hence, we propose a linear array to solve this problem. Suppose there are 3 sites A, B and C in a line as shown in Fig. 2.6(b), there are 3 CCFs, namely, $\gamma_{AB}$, $\gamma_{BC}$, and $\gamma_{AC}$, respectively. The advantage of linear array is that the azimuth of the $n$th source, $\theta_l$, is thought to be the same for each CCF so that the three CCFs share the same three unknown variables.

$$\begin{cases} Re(\gamma_{AB}) \approx J_0(r_{AB}\frac{\omega}{c}) - 2J_2(r_{AB}\frac{\omega}{c})\sum_{l=1}^{L}\lambda_l\cos 2\theta_l + 2J_4(r_{AB}\frac{\omega}{c})\sum_{l=1}^{L}\lambda_l\cos 4\theta_l \\ Re(\gamma_{AC}) \approx J_0(r_{AC}\frac{\omega}{c}) - 2J_2(r_{AC}\frac{\omega}{c})\sum_{l=1}^{L}\lambda_l\cos 2\theta_l + 2J_4(r_{AC}\frac{\omega}{c})\sum_{l=1}^{L}\lambda_l\cos 4\theta_l \\ Re(\gamma_{BC}) \approx J_0(r_{BC}\frac{\omega}{c}) - 2J_2(r_{BC}\frac{\omega}{c})\sum_{l=1}^{L}\lambda_l\cos 2\theta_l + 2J_4(r_{BC}\frac{\omega}{c})\sum_{l=1}^{L}\lambda_l\cos 4\theta_l. \end{cases} \quad (2.15)$$

According to Eq. (2.15), we obtain $\gamma_{AB}$, $\gamma_{BC}$ and $\gamma_{BC}$ from the observation records as knowns. Then we aim to estimate the 3 unknowns, namely, $c$, $\sum_{l=1}^{L}\lambda_l\cos 2\theta_l$, and $\sum_{l=1}^{L}\lambda_l\cos 4\theta_l$. To find out the optimum solution, we apply the bootstrap filter and a genetic algorithm (GA) as the inversion technique [57]. Under the assumption of $kr < \pi$, the CCF with the largest $r$ determines the effective range $kr$ for this method. For example, in the case shown in Fig. 2.6(b), the effective scope is $k < \frac{\pi}{r_{AC}}$.

### 2.2.4 Inversion technique to obtain phase velocity from CCFs

To find out the optimum solution, we apply a GA as the inversion technique to fit each CCF and to estimate the three unknowns $c$, $\sum_{l=1}^{L}\lambda_l\cos 2\theta_l$, and $\sum_{l=1}^{L}\lambda_l\cos 4\theta_l$. For convenience in applying the GA, we use a 30-bit long integer to indicate the 3 unknowns each of which is 10-bit long, namely,

$$x = \begin{bmatrix} x_1 \\ x_2 \\ x_3 \end{bmatrix} = \begin{bmatrix} c \\ \sum_{l=1}^{L}\lambda_l\cos 2\theta_l \\ \sum_{l=1}^{L}\lambda_l\cos 4\theta_l \end{bmatrix}. \quad (2.16)$$

Here, $x_1$ is chosen to be $kr_{max}$ in which $r_{max}$ is the largest array interval. Hence, we set $0 < x_1 < \pi$ so that $x_1$ has the resolution of $\frac{\pi}{2^{10}}$. $-1 < x_2 < 1$ so that $x_2$ has the resolution of $\frac{2}{2^{10}}$ and the same for $x_3$. If we define:

$$g(x, PQ) = Re(r_{PQ}) - J_0(\frac{r_{PQ}}{r_{max}}x_1) + 2J_2(\frac{r_{PQ}}{r_{max}}x_1)x_2 - 2J_4(\frac{r_{PQ}}{r_{max}}x_1)x_3, \quad (2.17)$$

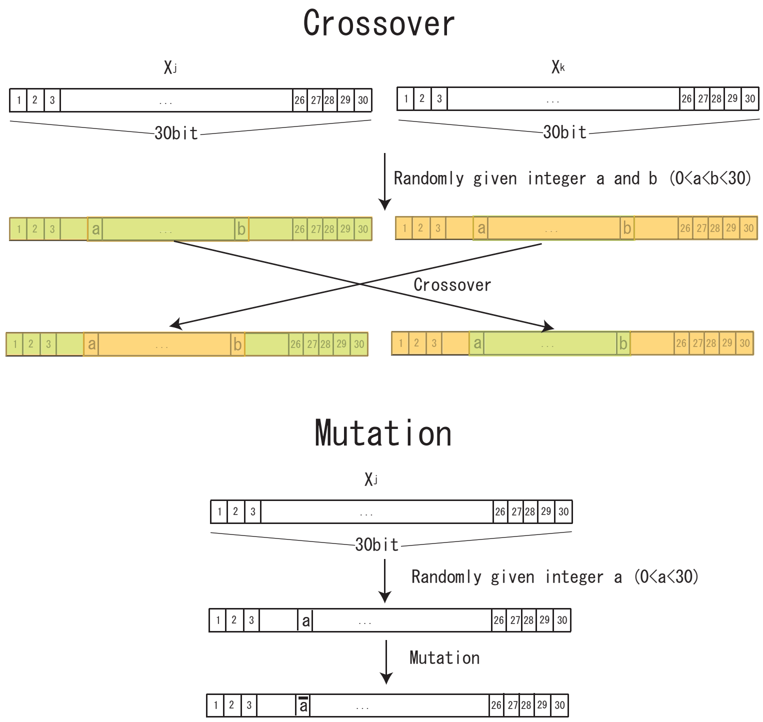


**Figure–2.7** Description of the crossover and mutation in GA

where $PQ$ indicates the 2 sites, namely, AB, AC, or BC, the fitness function ($z$) is defined as:

$$z = exp(\frac{-[g^2(x, AC) + g^2(x, AB) + g^2(x, BC)]}{2 \times 0.05^2})/(\sqrt{2\pi \times 0.05}). \tag{2.18}$$

Good estimation is expected by setting the population $N$ to be 10000 and the evolution times to be 20. In order to generate the next generation of population, the process of crossover and mutation will be done. Any "family" with "mom" $x_j$ and "dad" $x_k$ ($j, k = 1to10000, j \neq k$) is selected from the all the generation according to certain possiblity $w$ decided by the fitness (the larger fitness, the larger possibility):

$$w_k = z_k / \sum_{i=1}^{N} z_i \tag{2.19}$$

.

The crossover and mutation are realized as Fig. 2.7 shows and the symbol $a$ in Fig. 2.7

$$\bar{a} = \begin{cases} 1, a = 0 \\ 0, a = 1 \end{cases} \tag{2.20}$$

After each new whole generation is generated by selection, crossover and mutation, a parameter called the effective sample size [57] is defined to decide whether the generation is of good enough quality:

$$N_{eff} = 1/\sum_{i=1}^{N} w_i^2 \tag{2.21}$$

. In our case, the evolution of the population will continue until $N_{eff} > 100$. And finally, the estimation value would be calculated as:

$$x_f = \sum_{i=1}^{N} x_i w_i \tag{2.22}$$

.

Furthermore, in order to make the inversion process more efficient and quicker, we add a step before every generation, which is called particle swarm optimization (PSO). This method is proposed by Kennedy and Eberhart [59], found to be a very good tool for optimization. It searches in the complex space through collaboration and competition between individuals. Each particle will move toward the optimal particle by some decided direction and speed in the solution space. The final optimal solution would be found by iterative searches. Li et al. [57] pointed out that:

> It is an effective global optimization algorithm based on the all the fitness value of particles. They cooperate and compete to finally reach the best solution. The substance of PSO is that guide the next iteration position of the particles by using their information and the information of their individual extreme and global extreme. The individual and global extreme is two values the particles will track. The individual extreme is the optimal solution that the particle itself finds so far, and the other is the optimal solution that the whole population finds so far.

In our situation, the particle can be seen as in 3-dimension space as Eq. 2.16 shows. The position of $i$th particle can be shown as $X_i = (x_{i1}, x_{i2}, x_{i3})$, the velocity is denoted as $V_i = (v_{i1}, v_{i2}, v_{i3})$. The optimal location the $i$th particle experienced is indicated by $P_i = (p_{i1}, p_{i2}, p_{i3})$. And the optimal location of the particle swarm is expressed as $G = (g_1, g_2, g_3)$. As described in Li et al's work [57], when given the two extreme values, each particle updates its velocity and position according to:

$$v_{ij}(t+1) = wv_{ij}(t) + c_1 r_{1j}[p_{ij}(t) - x_{ij}(t)] + c_2 r_{2j}[g_j(t) - x_{ij}(t)] \tag{2.23}$$

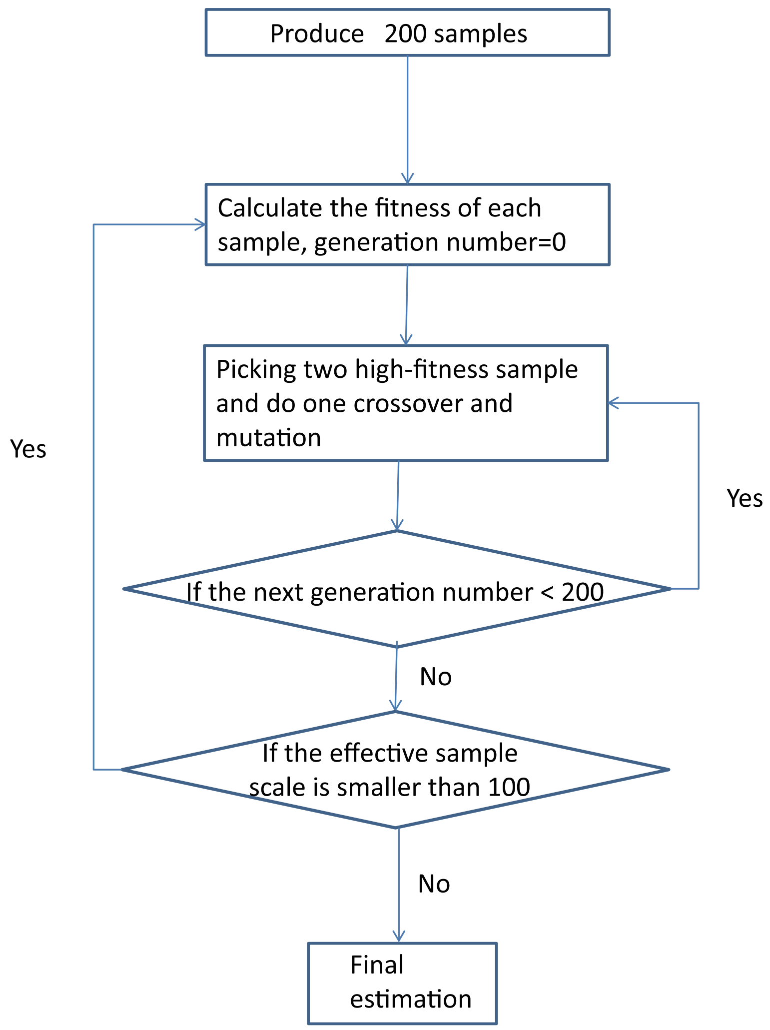


**Figure–2.8** The flow chart of the inversion technique using GA

.

$$x_{ij}(t+1) = x_{ij}(t) + v_{ij}(t+1), \tag{2.24}$$

where $i$ indicates the $i$th particle. $j$ indicates the $j$ dimension of the particles. $t$ indicates the $t$th generation. $w$ is called the inertia factor; the front velocity expresses the current velocity by the inertia factor. The larger $w$ is, the more the global search is strengthed; the smaller $w$ is, the more the local search is strenthened. And obviously, $c_1$ makes the particle fly to its own optimal position; $c_2$ makes the particle fly to the global optimal position. $r_1$ and $r_2$ are the independent random function, which have the value between 0 and 1.

The flow chart of this inversion technique is shown in Fig. 2.8.

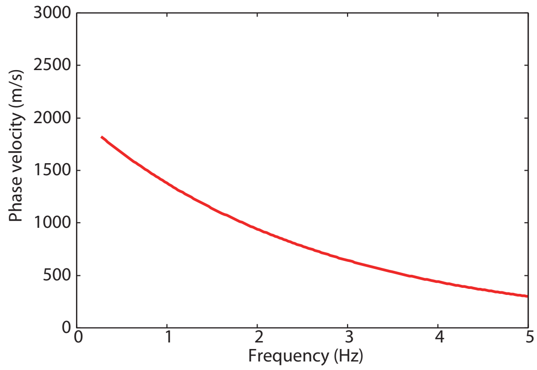


**Figure–2.9** Assumed phase velocity.

## 2.3 Numerical simulation

In this section, we use a numerical simulation to create a simple wavefield composed of plane waves. We demonstrate the process of using the GA to estimate the phase velocity and to examine the accuracy of the estimation in different wavefields.

### 2.3.1 Generating synthetic data

In order to confirm the availability of the new method, an extremely azimuth dependent simple wavefield composed of unidirectional plane waves is numerically simulated. We assume there is a linear array with 3 sensors, namely, A, B, and C. The intervals between adjacent sensors ($r$ and $0.5r$, $r = 30m$) are set to be different so that we can have 3 totally different CCFs ($\gamma_{AB}$, $\gamma_{BC}$, and $\gamma_{AC}$) to solve out the optimal solution. The vertical record for site A is constituted by:

$$Z(t) = \sum_{i=1}^{n} \{a(i)\cos(i\omega_0 t) + b(i)\sin(i\omega_0 t)\}, \tag{2.25}$$

wherein $a(i)$ and $b(i)$ are Gaussian variables given randomly. The time step is set to be 512 and the time interval is 0.08s, so the $\omega_0 = \frac{2\pi}{512\times0.08}(\frac{1}{\text{second}})$. The fundamental mode of the phase velocity of Rayleigh waves is assumed. Hence, under the assumption of plane waves, records for the other two sites can be calculated.

Using these records, the CCFs between each pair of sites can be obtained. The effective scope is $k < \frac{\pi}{r_{AC}} = \frac{\pi}{45}$, namely, $\frac{2f}{v} < \frac{1}{45}$. Given the assumed phase velocity as shown in

Fig. 2.9, the effective scope is around $f < 4.5Hz$. Then, using the inversion technique introduced previously, the estimated phase velocity can be obtained for different cases of a synthetic wavefield.

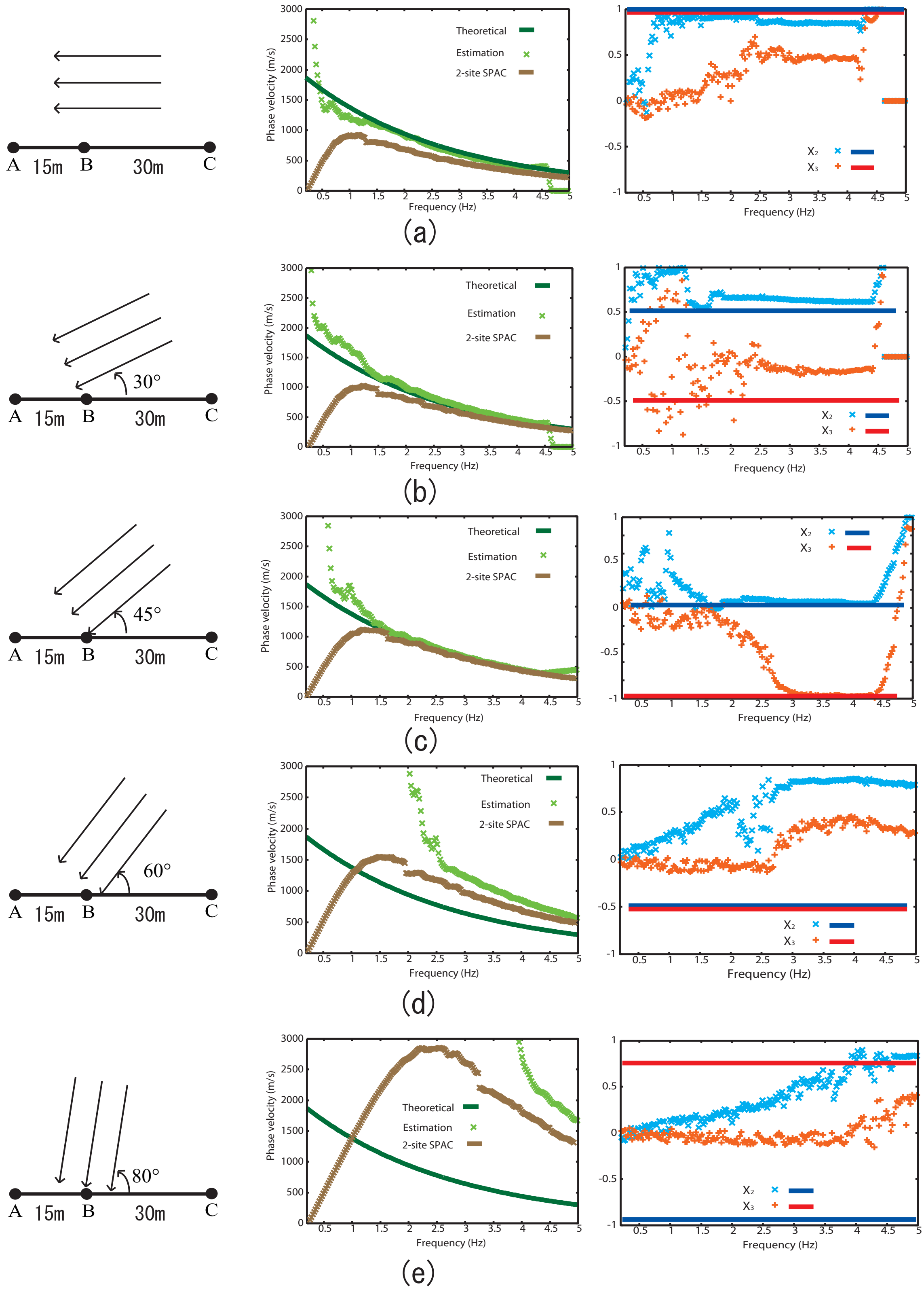


**Figure–2.10** Estimation of phase velocity, $x_2$ and $x_3$ in case of unidirectional plane wave with different direction. The left column shows the direction of the unidirectional wave. The middle column shows the estimation of phase velocity in which the deep green curve indicates the theoretical phase velocity, the light green dot shows the estimation by proposed method and the grey curve indicates the estimation using $J_0$ method. The right column shows the estimation of $x_2$ and $x_3$ in which the solid blue and red line shows the theoretical $x_2$ and $x_3$, respectively and the blue and red dot shows the estimation of $x_2$ and $x_3$ by proposed method, respectively. From above to below shows the estimations in case of different direction of unidirectional wave: (a) 90° (b) 60° (c) 45° (d) 30° (e) 10°.

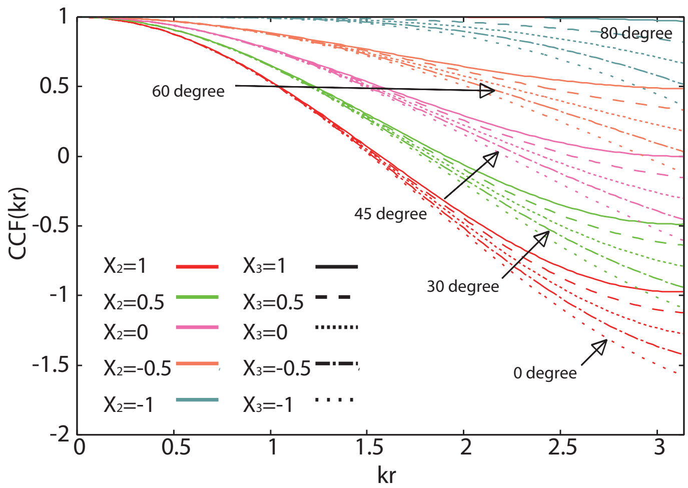


**Figure–2.11** Variation in CCF with respect to $kr$ in case of different $x_2$ and $x_3$. Different color indicates different $x_2$ and the different line style shows different $x_3$. For the unidirectional wave case, the corresponding curve with typical angle which is shown in the left column of Fig. 2.10 is marked out using arrows.

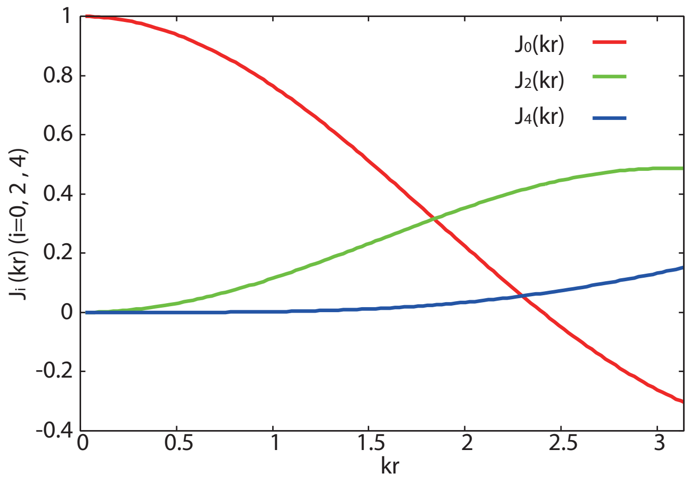


**Figure–2.12** Bessel function. The first type of Bessel function with order 0, 2, and 4 are drawn here.

### 2.3.2 Results and analysis in an extremely azimuth-dependent wavefield

Firstly, we see the estimation of the phase velocity in the case of plane waves in different directions as shown in Fig. 2.10. The left column shows the direction of the unidirectional wave. The middle column shows the estimation of phase velocity in which the deep green curve indicates the theoretical phase velocity, the light green dot shows the estimation by proposed method and the grey curve indicates the estimation using $J_0$ method. The right column shows the estimation of $x_2$ and $x_3$ in which the solid blue and red line shows the theoretical $x_2$ and $x_3$, respectively and the blue and red dot shows the estimation of $x_2$ and $x_3$ by proposed method, respectively. In the case of 0°, 30° and 45°, the estimations match the theoretical ones well in the frequency range of 2.0 to 4.0Hz, or in the $kr_{max}$ range of 0.5 to 3.0, wherein $r_{max}$ denotes the largest interval among the sites. The estimation is poor when the angle is larger than 45° as shown in Fig. 2.10. To understand this, we see how the CCF varies with $x_1$ in the case of different $x_2$ and $x_3$ as shown in Fig. 2.12. Different color indicates different $x_2$ and the different line style shows different $x_3$. For the unidirectional wave case, the corresponding curve with typical angle which is shown in the left column of Fig. 2.10 is marked out using arrows. It demonstrates that the CCFs are more sensitive with respect to $x_1$ when $x_2$ is closer to 1 and/or $x_3$ is closer to $-1$. Hence, it is clear that in the case of 0° in which $x_2 = 0$, $x_3 = -1$, 30° in which $x_2 = 0.5$, $x_3 = -0.5$, and 45° in which $x_2 = 1$, $x_3 = 1$, the sensitivity with respect to $x_1$ is higher than 60° in which $x_2 = -0.5$, $x_3 = -0.5$ and 80° in which $x_2 = -0.94$, $x_3 = 0.77$. Moreover, the first type of Bessel function with order 0, 2, and 4 are drawn in Fig. 2.11 for better understanding. Because $J_2(kr)$ is larger than $J_4(kr)$ when $kr < 3.14$ as shown in Fig. 2.11, the sensitivity of CCFs with respect to $x_2$ is higher than that with respect to $x_3$. This explains that in the case of 0° in which $x_2 = 0$, $x_3 = -1$, 30° in which $x_2 = 0.5$, $x_3 = -0.5$ and 45° in which $x_2 = 1$, $x_3 = 1$, the estimation of $x_3$ is not accurate enough as shown in Fig. 2.10 (a), (b), and (c). From the numerical simulation above, we can draw a conclusion that in such an extremely azimuth-dependent wavefield, the linear array method works when the angle between the dominant wave and the linear array is at least smaller than 60°.

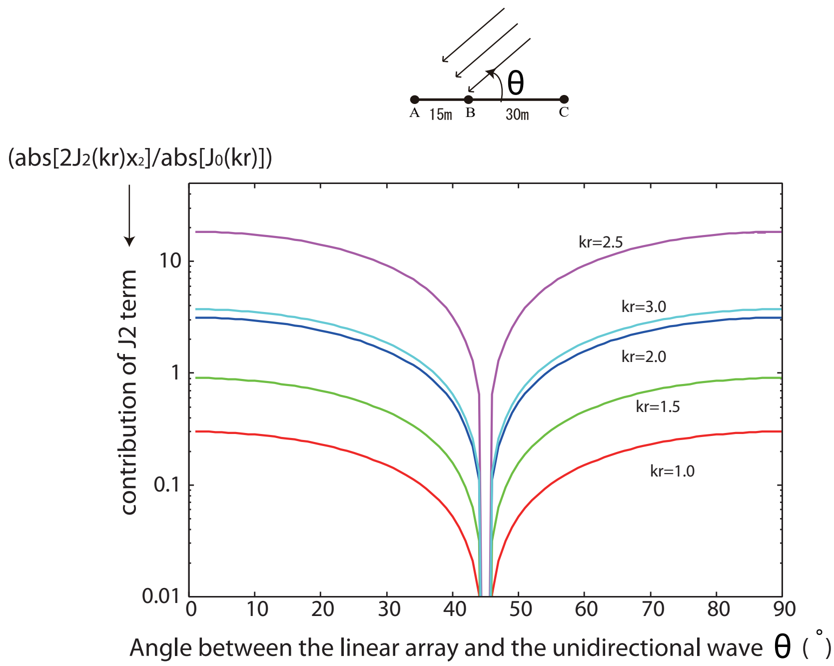


**Figure–2.13** Contribution of $J_2$ term to $J_0$ term defined in Equation (2.26). The horizontal axis indicates the angle $\theta$ which shows the direction of unidirectional wave. The vertical axis indicates the contribution. Different color from red to pink shows the contribution in case of different value of $kr$.

Chávez-García et al. [28, 29] have advocated that the SPAC method without taking azimuthal average could provide acceptable accuracy in certain kind of wavefields. This means that only $J_0$ term of Eq. 2.13 is enough to estimate the phase velocity of Rayleigh wave using a simultaneous observation at only two sites, thus, we call their concept "$J_0$ method", hereafter. However, it is strictly available only under the condition of isotropic wavefield. In the extremely azimuth-dependent wavefield as described above, the $J_0$ method is applied using BC and the estimation is also shown in Fig. 2.10 by the brown dots. We can see that in case (d) and (e), it has quite bad match similar as that from the proposed method, as expected. However, for case (a) and (b), the estimations deviate from the theoretical one while estimation from the proposed method is quite good. This is because the $J_0$ method does not consider the effect of the $J_2$ and $J_4$ terms. Considering the contribution of $J_4$ term is relatively much smaller than $J_2$ as shown in Fig. 2.12, the absolute ratio between $J_2$ term and $J_0$ term:

$$R_{J_2/J_0} = \frac{|2x_2 J_2(kr)|}{J_0(kr)} \tag{2.26}$$

is shown in Fig. 2.13. In the figure, we show the variation of the contribution with respect to the angle between linear array and the uni-directional wave. The horizontal axis indicates the angle $\theta$ which shows the direction of unidirectional wave. The vertical axis indicates the contribution. Different color from red to pink shows the contribution in case of different value of $kr$. We can see that when the degree is $0°$, namely, in case (a), the contribution of $J_2$ term is very large. This explains the reason of the deviation of estimation from $J_0$ method. Moreover, in case (c) whose azimuth is $45°$, the contribution of $J_2$ term is the smallest so the deviation is almost zero. It shows another possible case that $J_0$ method can be well applied except for the isotropic wavefield.

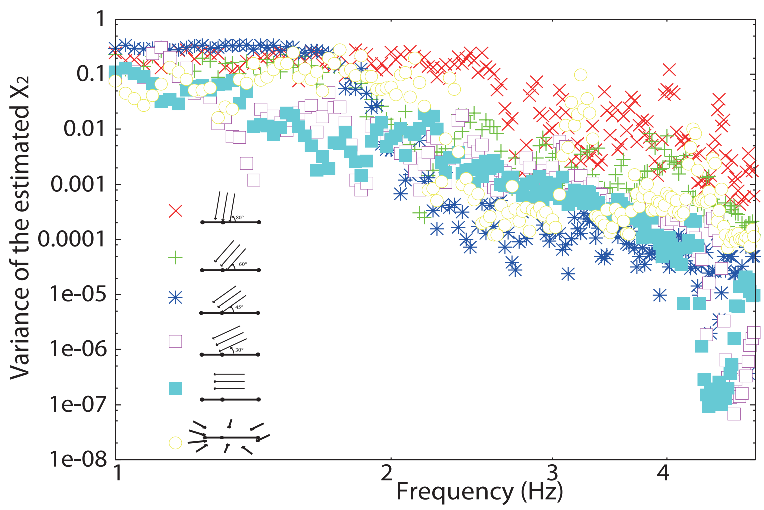


**Figure–2.14** The variance of $x_2$ in each case of the unidirectional wavefield. The horizontal axis indicates frequency and the vertical variance is the variance of $x_2$. Dots of different color from red to yellow indicates different direction of unidirectional wave, which are described using small schemes in the figure.

- **Discussion**

We discussed the estimation error qualitatively above. To be more exact, we would like to propose a parameter to evaluate the estimation accuracy quantitatively. As explained above, the $x_2$ has large sensitivity with respect to CCFs so that the convergence condition of $x_2$ has the potential to indicate the estimation accuracy. In order to see it, the variance in estimated $x_2$ in case of different unidirectional and isotropic wavefields is plotted in Fig. 2.14. The horizontal axis indicates frequency and the vertical variance is the variance of $x_2$. Dots of different color from red to yellow indicates different direction of unidirectional wave, which are described using small schemes in the figure. It is observed that in the cases of 60° and 80°, the variance is obviously larger than that in other cases. It demonstrates the poor convergence condition in the two cases, which coincides with what was observed in the previous section. For the case of an isotropic wavefield, it is observed that the variance decreases down steeply around 2.5Hz and shows a narrower effective scope of estimation than the three cases of 0°, 30°, and 45°. In addition, the fluctuation in the case of the isotropic wavefield is also larger than the others. This phenomenon would be confirmed in the section 2.3.3. From these, we can say that the variance of $x_2$ has a high potential to work as an indicator for evaluating the estimation accuracy.

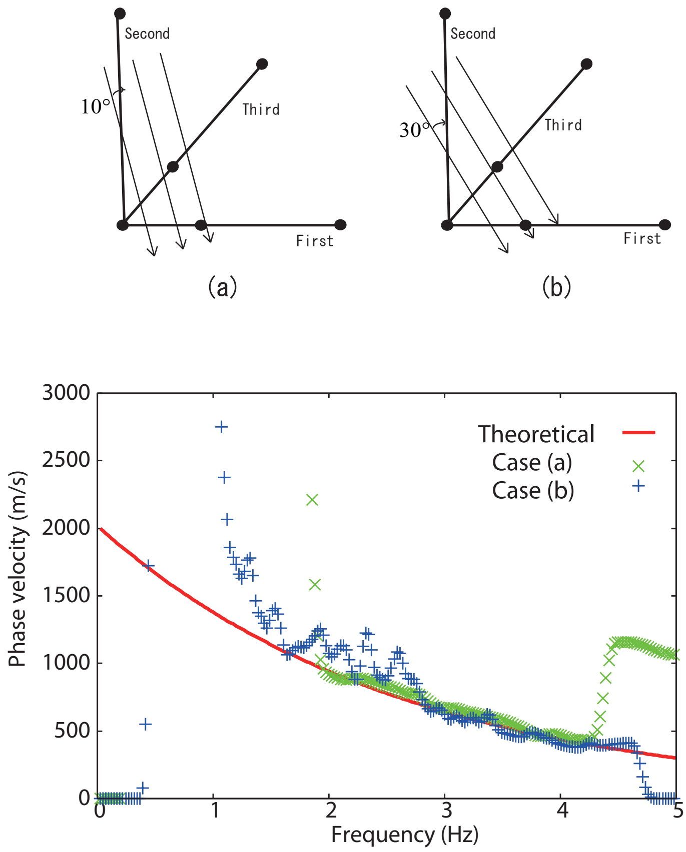


**Figure–2.15** The estimations using 3 linear arrays in unidirectional wavefield. Two cases (a) and (b) with different direction of unidirectional wave are examined. In each case, there are the first, second and third linear arrays. The angle between first and second is 90° and the angle between first and third is 45°. The green and blue dots indicates the estimation in case (a) and (b), respectively. The red curve indicates the theoretical phase velocity.

- **More arrays in extremely bad wavefield**

Therefore, it is risky to use only one linear array to do the estimation in certain cases, such as when $x_2$ is very low. A second linear array is used to support the estimation. In order to get a totally different sensitivity for CCFs with respect to $x_1$, we make the second and first linear arrays form an angle of 90° so that $x_2^{second} = -x_2^{first}$ due to $\cos(\theta \pm (90° \times 2)) = -\cos\theta$ according to Eq. 2.16. $x_2^{second}$ and $x_2^{first}$ indicates the $x_2$ of the first and second array in the same wavefield as shown in Fig. 2.15, respectively. For example, if $x_2^{first} = -1$, $x_2^{second} = 1$. $x_3^{second} = x_3^{first}$ due to $cos(\theta \pm 360°) = cos(\theta)$. Moreover, we make the third linear array and first linear array form an angle of 45° so $x_3^{third} = -x_3^{first}$ due to $\cos(\theta \pm (45° \times 4)) = -\cos\theta$. $x_3^{third}$ indicates the $x_3$ of the third array in the same wavefield as shown in Fig. 2.15. It is thought that by using these three arrays, a diversity in sensitivity of the CCFs can be obtained. The estimation process is that (1) we use these three arrays to obtain three estimations; (2) we extinguish any obviously abnormal solutions; (3) we take the average of the rest to obtain the final solution. To confirm the availability, we apply some examples of arrays to do the estimation as shown in Fig. 2.15. Two cases (a) and (b) with different direction of unidirectional wave are examined. In each case, there are the first, second and third linear arrays. The angle between first and second is 90° and the angle between first and third is 45°. The green and blue dots indicates the estimation in case (a) and (b), respectively. The red curve indicates the theoretical phase velocity. It is observed that the estimation matches with the theoretical one in the frequency range of 2.0 to 4.0Hz, or in the $kr_{max}$ range of 0.5 to 3.0. We can see that by using more linear arrays, an accurate estimation could be guaranteed. It is obvious that the angle between the two linear arrays need not be exactly 90° or 45°. That is because the inversion technique itself allows the estimation to be available in a certain range of the directionality of the wavefield.

### 2.3.3 Results and analysis in a moderately azimuth-dependent wavefield

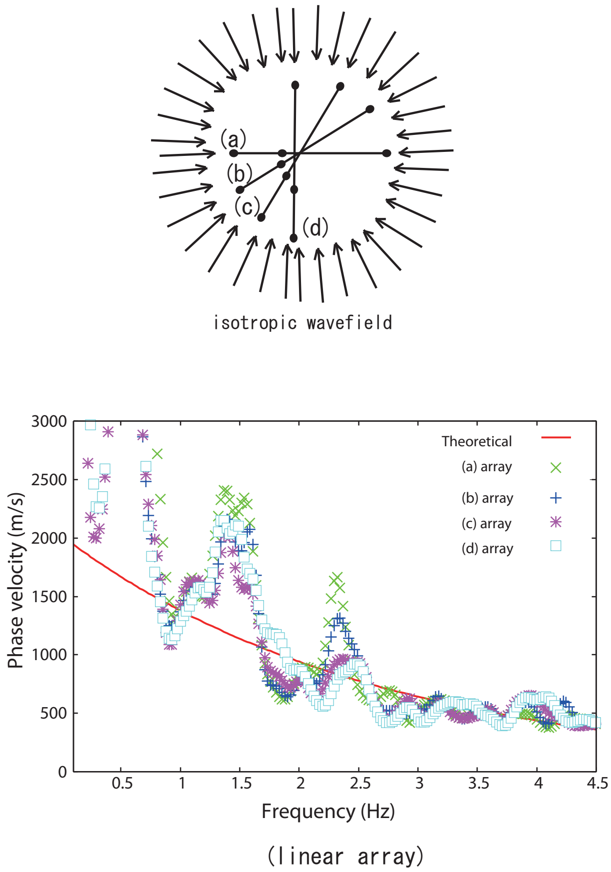


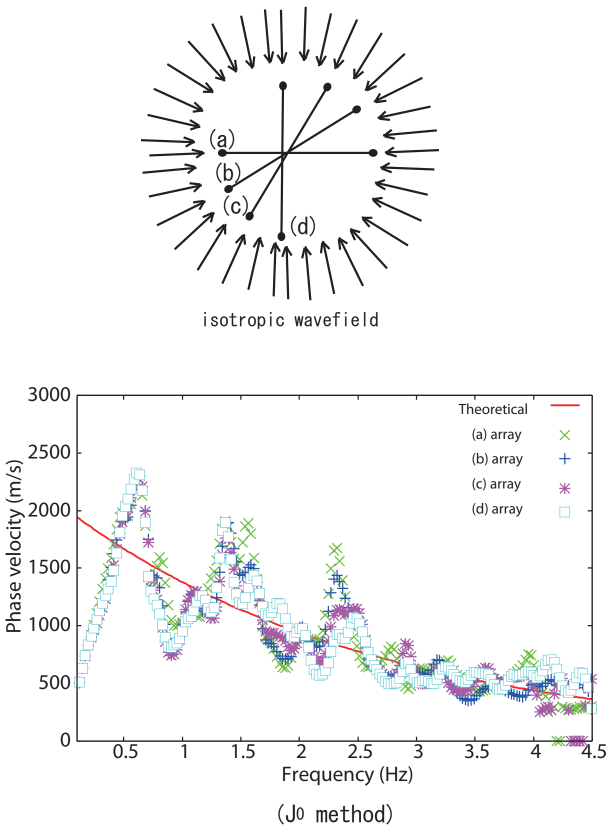


**Figure–2.16** Estimation of 4 linear arrays with different direction in an isotropic wavefield. Each arrow in the upper part indicates one wave from one diretion. Each wave has the same power to constitute an isotropic wavefield. The four linear arrays (a), (b), (c), (d) have different directions the angle interval is $90/4 = 22.5°$. In the lower part, dots of different colour from green to blue indicate the estimation from linear array (a) to (d), respectively. The red curve indicates the theoretical phase velocity.

**Figure–2.17** Estimation of 4 linear arrays with different direction in in the isotropic wavefield by $J_0$ method

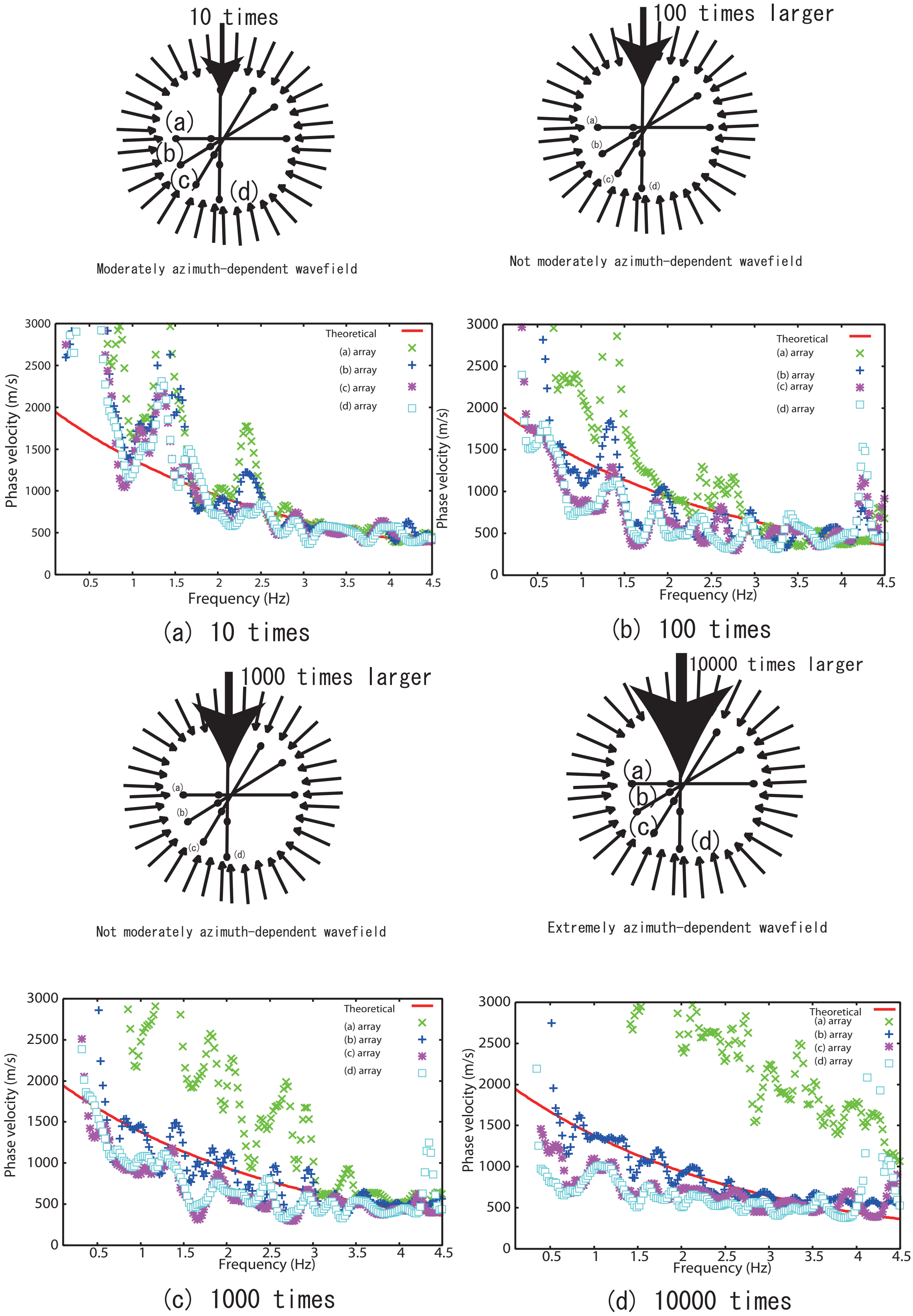


**Figure–2.18** Estimation of 4 linear arrays with different direction in an azimuth-dependent wavefield. There is one wave in certain direction which has obviously larger power than others. With the power increasing from 10 times to 10000 times, the corresponding estimations are shown in (a) to (d), respectively.

In real cases, there is barely such extremely azimuth-dependent wavefield. Past research has shown that when in low-frequency range there is some azimuth-dependent component, in high-frequency range, the wavefield is almost isotropic or moderately azimuth-dependent [41]. We would like to demonstrate that the linear array method works well in such wavefield. We use the same technique as in section 2.3.1 to constitute this kind of wavefield, for simplicity, in all-frequency range. As Fig. 2.16 shows, it is an isotropic wavefield where waves come from 36 directions evenly, namely, one wave each 10°. Each arrow in the upper part indicates one wave from one diretion. The four linear arrays (a), (b), (c), (d) have different directions the angle interval is $90/4 = 22.5°$. In the lower part, dots of different color from green to blue indicate the estimation from linear array (a) to (d), respectively. The red curve indicates the theoretical phase velocity. For a comparison, the estimations in the isotropic wavefield by $J_0$ method is also shown beside in Fig. 2.17. It can be seen that for each array of $J_0$ method, there is actually only 2 sites in Fig. 2.17. As Fig. 2.18 (a) shows, it is a moderately azimuth-dependent wavefield. The only difference with the isotropic one is that the wave from one particular direction has power 10 times larger than wave from other directions. For both wavefields, there is four linear arrays with different directions. The estimations from these linear arrays are shown in the same figures.

We can see that for both wavefields, the estimations by proposed method are accurate in the frequency range of 2.5 to 4.5Hz, namely, the $kr_{max}$ range of 0.8 to 3.0. It confirms the availability of the proposed method in the isotropic wavefield or in the moderately azimuth-dependent wavefield. In these wavefields, the estimation of linear array is stable regardless of azimuth. Meanwhile, the $J_0$ method works well in the isotropic wavefield as shown in Fig. 2.17, which coincides with what has been mentioned in past research [14,32]. However, it is also observed that for both Figs. 2.16 and 2.18 compared with Fig. 2.10, the estimation in frequency range 1.5 to 3Hz, namely, the $kr_{max}$ range of 0.4 to 1.3 is unstable and sometimes deviate from the theoretical curve. It may be caused by the still not good sensitivity of CCF in relative to $x_1$ of Eq. 2.16. The proposed method uses 3 CCFs, $\gamma_{AB}, \gamma_{AC}, \gamma_{BC}$ to estimate the phase velocity in the frequency domain. At each frequency, $kr$ is different for each CCF because $r_{AB} \neq r_{AC} \neq r_{BC}$. As shown in Fig. 2.11, the sensitivity of CCFs, with respect to $kr$, is lower when $kr$ is smaller. Hence, in the

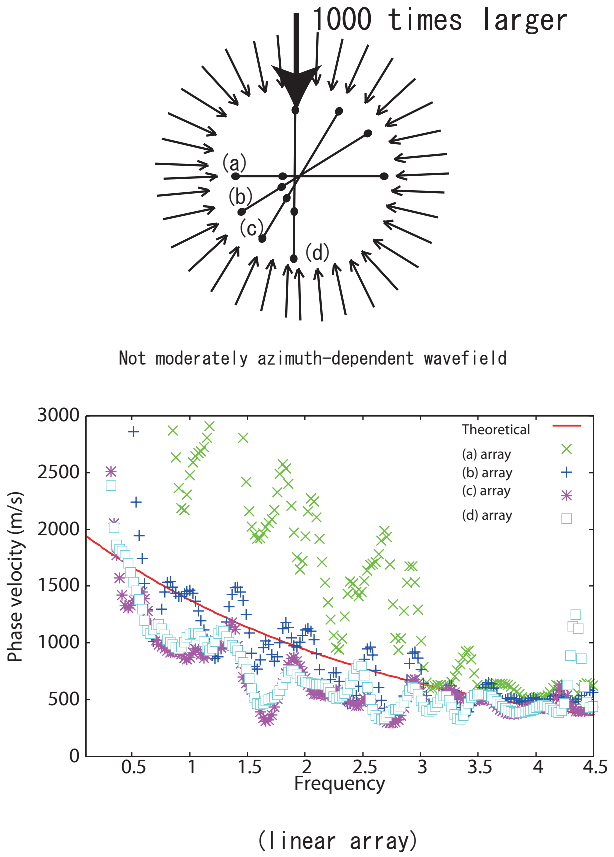


**Figure–2.19** Estimation of 4 linear arrays with different direction in the wavefield of Fig. 2.18 (c) by proposed method

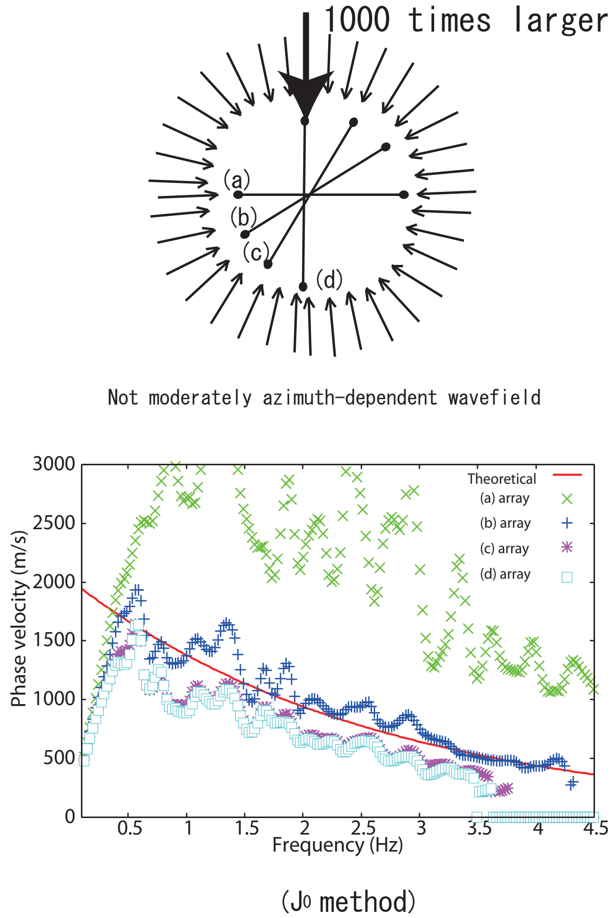


**Figure–2.20** Estimation of 4 linear arrays with different direction in in the wavefield of Fig. 2.18 by $J_0$ method

low frequency range, $kr_{min}$, wherein $r_{min}$ means the shortest distance among the 3 sites, is very small, so that the sensitivity of CCFs with $r_{min}$ is low. In other words, the accuracy in the low frequency range by proposed method is confined by the CCFs with smallest $r$. As a comparison, the SPAC method just uses a “pure” large array for the low frequency range, so it has a more accurate estimation in the low frequency range. This can be seen from the comparison of Fig. 2.16 and Fig. 2.17. In Fig. 2.17, the stability of estimation in low frequency range is better than that in Fig. 2.16 because it uses “pure” large interval array ,though, consisting of only 2 sites. Hence, in these two simulation, the estimation in low frequency range 1.5 to 2.5Hz is easy to be vulnerable to the error of CCF, thus not accurate.

To be more comprehensive, let us set the power of the particular direction as 100 times and 1000 times larger than the wave from other direction. Let us see the result of that in Figs. 2.18 (b) and (c). It can be seen that although the wavefields in these two figures seem being as extreme as in section 2.3.2, the proposed method using very simple linear array still shows very stable estimations. Similarly, in the low frequency range of $kr_{max}$ of 0.5 to 1.3, the estimations of the 4 linear arrays are not consistently stable. It comes from the reasons described before. We can see that in Fig. 2.18 (c), even the power at one direction is about 96 percent of all from the calculation $\frac{1000}{1000+35}$ which is similar to the extreme case as Fig. 2.10 shows mathematically, the proposed method surprisingly works for every direction as effectively as in the isotropic wavefield as shown in Fig. 2.16 despite the unstability in low frequency range. This shows the strong capability/sensitivity of the proposed method along with the inverson technique to extract the phase velocity out using multi-CCFs even in a not moderately azimuth-dependent wavefield.

Another compelling phenomenon is that for the last all four cases, it can be observed that in the frequency range larger than about 4.2Hz, namely, in the $kr_{max}$ range of larger than 2.9, the estimation becomes not accurate. It seems contradicting with the assumption that the estimation range is $kr_{max} < 3.14$. This can be explained by observing Fig. 2.11. It can be seen that when $kr_{max}$ is larger than around 2.8, the slope of the curves becomes flat again, which means the sensitivity decreases and the accuracy of estimation would decrease. This theoretical background matches with the phenomenon. Hence, it can be concluded that for a linear array estimation in this numerical simulation, the convincing effective $kr_{max}$ range is about 1.3 to 2.8 and the corresponding frequency range is about 3.0 to 4.2Hz in our simulations done so far.

For a comparison, we conducted the $J_0$ method here in the wavefield as shown in Fig. 2.18 (c) using the two sites of A and C, the consequent estimation and the comparison with that from the proposed method in shown in Fig.2.19 and Fig. 2.20. It can be seen that using simple $J_0$ method, of course, caused the bad estimations. This phenomenon shows the limited capability of $J_0$ method and the good robustness of proposed method.

As the power of the dominating wave becomes larger and larger until the power at one particular direction is 100000 times larger than others, the estimation is more and more similar to that in Fig. 2.10 as shown in Fig. 2.18 (d). This result makes it clear that if the power of one dominating wave is large enough, this wavefield can be called the extremely azimuth-dependent wavefield and the just one linear array method cannot work well or stably for all directions. However, this kind of case is very rare in real cases. Hence, through these numerical simulation, we can see that the proposed method has very good practical capability to estimate phase velocity of Rayleigh wave using a new and convenient array shape. The compensation using several linear arrays has no need to be adopted in real case. This part of research can be regarded as a good compensation to the Hayashi's research [22, 23] about linear array.

## 2.4 The influence of the array setting on the estimation accuracy of linear array

In the previous section, we used GA as the inversion technique and analyzed the estimations using different kind of synthetically constituted wavefield. However, the array setting we used is barely well interpreted. We just used 3 sites on a line with the intervals, which is seemingly proper. After all, although we mentioned that it is appropriate to use 3 CCFs to calculate the 3 unknowns. It has not been discussed if there is a better or an optimum solution for the accuracy of the final estimation of phase velocity. Hence, in order to discuss more comprehensively about the effective range of the proposed method, these work is necessary. We would do this in three parts: firstly, the influence of the number of sensors (CCFs); secondly, the influence of the intervals of sensors; thirdly, the influence of the incoherent noise.

### 2.4.1 Influence of the number of sensors $N_s$ and the influence of the number of unknowns

In most cases, it is much more difficult to control the intervals among the sensors than to control the number of sensors. Hence, we assume 1: 2: 4: ... as a proper proportion of the adjacent intervals. On the basis of this, we discuss the influence of the number of sensors.

Let us see the equation of CCF again [24]:

$$Re(\gamma_{pq}) = J_0(kr) + 2\sum_{n=1}^{\infty}\{(-1)^n J_{2n}(kr)\sum_{l=1}^{L}\lambda_l \cos 2n\theta_l\}, \tag{2.27}$$

When $N_s = 3$, it becomes:

$$\begin{aligned} Re(\gamma_{pq}) &\approx J_0(kr) - 2J_2(kr)\sum_{l=1}^{L}\lambda_l \cos 2\theta_l \\ &+ 2J_4(kr)\sum_{l=1}^{L}\lambda_l \cos 4\theta_l. \end{aligned} \tag{2.28}$$

As described previously, when $kr < \pi$, the Bessel function with order larger than 6 can be neglected. Hence, there remain only 3 unknowns and for 3 sensors, there are just 3 CCFs, which are expected to solve out the 3 unknowns. On the other hand, if we use more unknowns for example we neglect the order larger than 8, the number of unknowns will become more and it may need more sensors to constitute more CCFs for the estimation accuracy:

$$\begin{aligned} Re(\gamma_{pq}) &\approx J_0(kr) - 2J_2(kr)\sum_{l=1}^{L}\lambda_l \cos 2\theta_l \\ &+ 2J_4(kr)\sum_{l=1}^{L}\lambda_l \cos 4\theta_l \\ &- 2J_6(kr)\sum_{l=1}^{L}\lambda_l \cos 6\theta_l. \end{aligned} \tag{2.29}$$

In order to confirm all this, let us do the similar simulation as above with different number of sensors and different forms of Eq. 2.28 for different number of unknowns. In order to be unifying, we use the moderately azimuth-dependent wavefield as in Fig. 2.18 (c), which is with the largest power 1000 times of the other wave. In addition, in order to make this series of analysis more convincing, easy understanding and practical, we classify the conditions in the first place by the number of sensors. We will consider the conditions in case of the sensor number of 2, 3 and 4. For each case, we would classify in more dimensions according to different application of Eq. 2.28. And finally we will summarize all these analysis. For the convenience to describe, we use $N_j$ to show the order of Bessel function up to which we used. For example, $N_j = 1$ means using just $J_0$ term and $N_j = 3$ means using up to $J_4$ term.

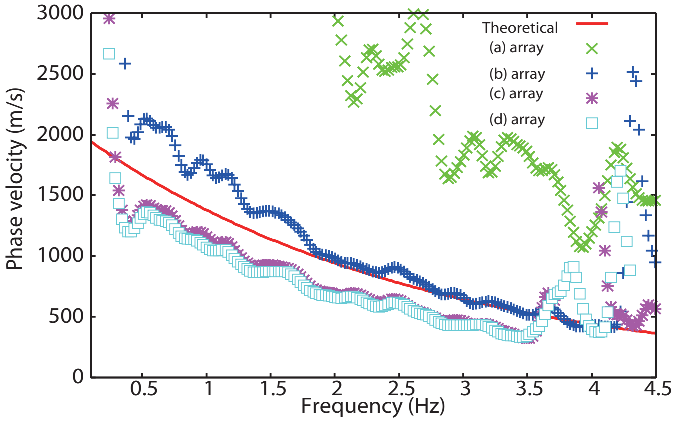


(a) Nj=1

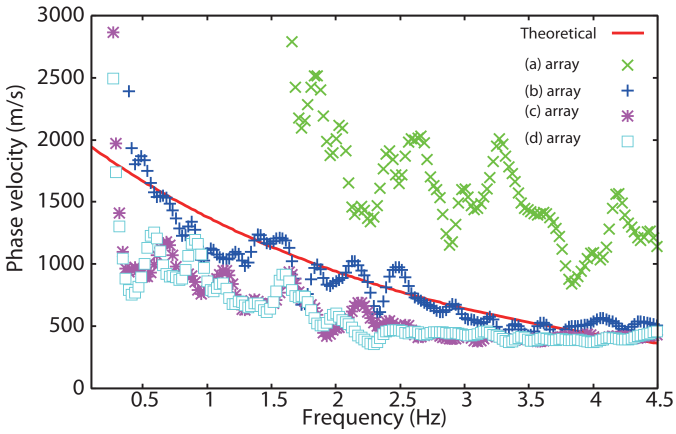


(b) Nj=2

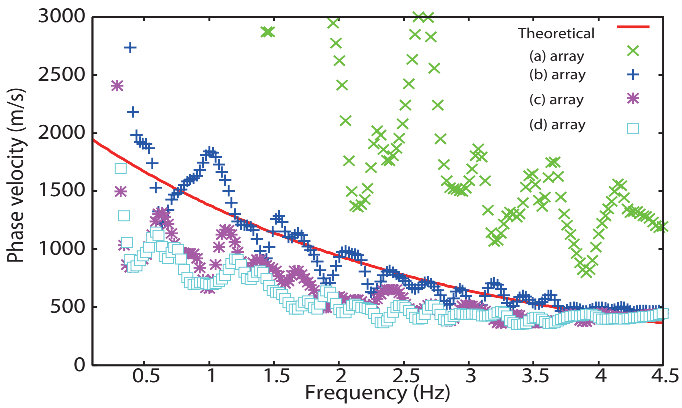


(c) Nj=3

**Figure–2.21** Estimation of 4 2-site linear arrays with different direction in an extremely azimuth-dependent wavefield. Every linear arrays uses only 2 sites. Estimations in different value of $N_j$, 1, 2 and 3, are shown in (a), (b) and (c), repectively. Dots of different colour from green to blue indicate the estimation from linear array (a) to (d), respectively. The red curve indicates the theoretical phase velocity

- **2-site case**

For only 2 sites, the possibility is quite limited. We tested three conditions in this case: (1) using only $J_0$ term; (2) using up to $J_2$ term; (3) using up to $J_4$ term as done so far. As for wavefield, we used the wavefield as in Fig. 2.18 (c) without loss of generality. The estimation is shown in Fig. 2.21. Every linear arrays uses only 2 sites. Estimations in different value of $N_j$, 1, 2 and 3, are shown in (a), (b) and (c), repectively. dots of different colour from green to blue indicate the estimation from linear array (a) to (d), respectively. The red curve indicates the theoretical phase velocity. It can be shown that for 2 two-site estimation, whatever we choose as $N_j$, the estimation is not only bad but also not consistent and shows no clear tendency. It is similar to the $J_0$ method but it used the proposed inversion technique to "try" to extract the phase velocity out using the information from just one CCF. It is very easy understanding because the information is too little for just one CCF. Even though this case is too obvious to be available, we still would like to demonstrate it because it helps to describe well about the limit of the "2-site" method.

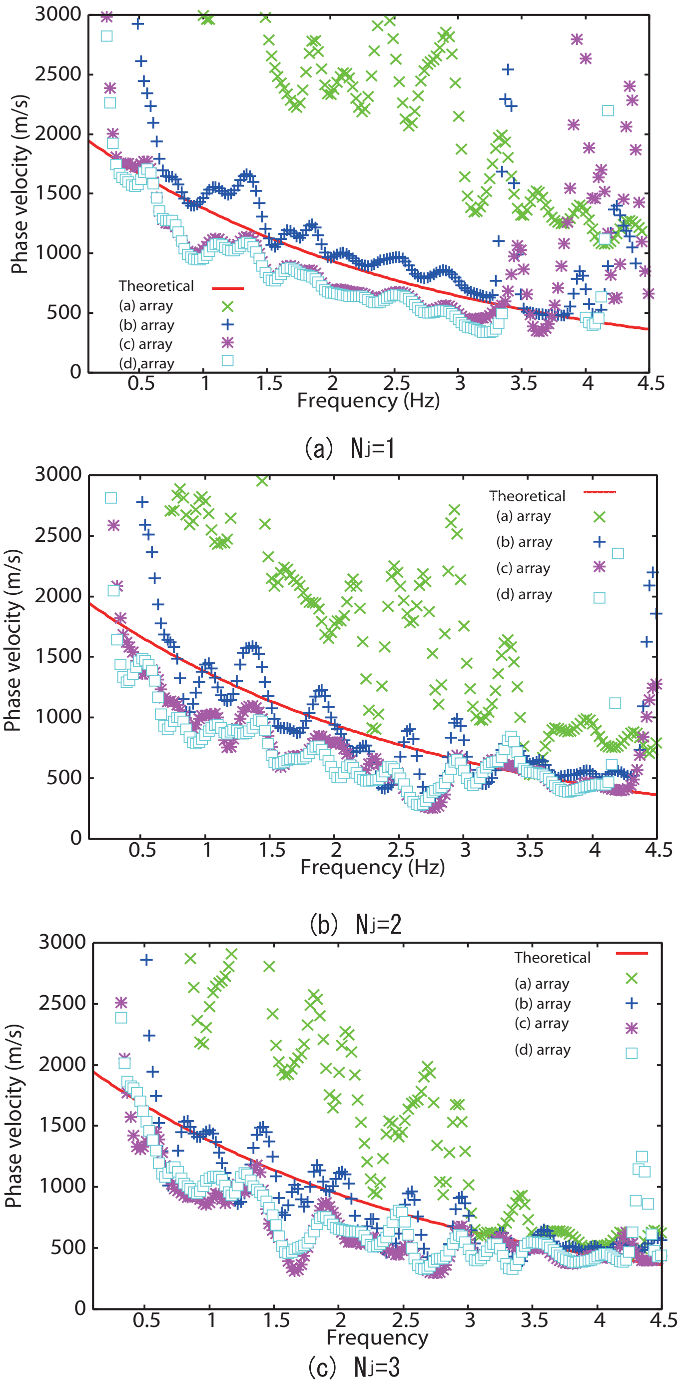


**Figure–2.22** Estimation of 4 3-site linear arrays with different direction in an extremely azimuth-dependent wavefield. Every linear arrays uses 3 sites. Estimations in different value of $N_j$, 1, 2 and 3, are shown in (a), (b) and (c), repectively.

- **3-site case**

For the case of 3 sites, it is possible to apply 3 CCFs to do estimations. If we use 3 CCFs, it is just the same as shown by lots of analysis in the last section. Here, in order to emphasize the necessity to use 3 CCFs, we do more numerical simulations about this. The estimations of using 1 CCF ($N_j = 1$) and 2 CCFs ($N_j = 2$) are demonstrated together with that using 3 CCFs ($N_j = 3$) in Fig. 2.22. Applying the intrinsics of Eq. 2.27, it can be shown that as the $N_j$ becomes larger, the accuracy in high frequency range becomes more and more accurate because when $N_j$ is small, even we have lots of information, namely, 3 CCFs, the high-error theory, which does not considering the contribution of the $J_2$ and $J_4$ term which is high in high-frequency range, would cause the unstable and wrong answer. And both 3 cases show bad estimations in low frequency range. According to the results in the last section, it is because of the low sensitivity of CCFs in low frequency range. This test shows the significance of using 3 CCFs in proposed method to obtain a stable estimation with an acceptable accuracy.

- **4-site case**

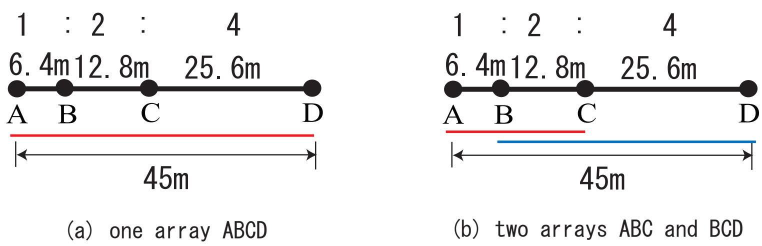


**Figure–2.23** (a) a 4-site linear array with interval ratio of 1:2:4; (b) The same 4-ste array as in (a), however, it can be regarded as 2 3-site arrays.

For the case of 4 sites, it is expected that if we make $N_j = 3$, the accuracy would be improved because there are more CCFs from more pairs of sites with different intervals. Using the conclusion drawn in the next subsection first, we make the intervals of 4 sites as 1 : 2 : 4 as shown in Fig. 2.23 (a). The Eq. 2.18 is modified as:

$$z = exp(\frac{-[g^2(x, AC) + g^2(x, BD) + g^2(x, AD) + g^2(x, BC) + g^2(x, CD) + g^2(x, AB)]}{2 \times 0.05^2 \times (\sqrt{2\pi} \times 0.05)} \tag{2.30}$$

It can be seen that 6 CCFs are used in the fitness equation. Then, the estimation of phase velocity can be calculated and the result is shown in Fig. 2.24 (a). Estimation of 4 4-site linear arrays with different direction in an extremely azimuth-dependent wavefield. Every linear arrays uses 3 sites. The red curve indicates the theoretical phase velocity. The curves with 4 different colors shows the estimation from (a), (b), (d), (d) array with

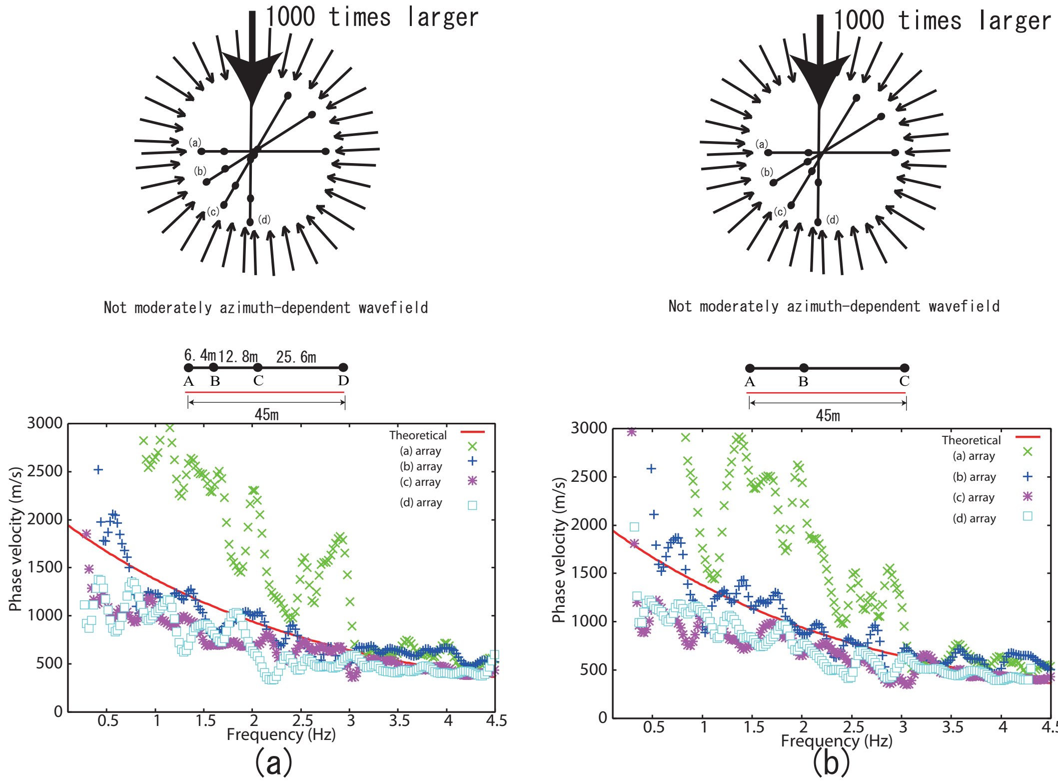


**Figure–2.24** (a) Estimation of 4 4-site linear arrays with different direction in an extremely azimuth-dependent wavefield. Every linear arrays uses 3 sites. The red curve indicates the theoretical phase velocity. The curves with 4 different colors shows the estimation from (a), (b), (d), (d) array with different direction, repectively. In the wavefield, there is one wave in certain direction which has obviously larger power than others (1000times); (b) The estimations from 3-site arrays for comparison

different direction, repectively. In the wavefield, there is one wave in certain direction which has obviously larger power than others, which is 1000times larger. The estimations from 3-site arrays using 3 CCFs are shown in Fig. 2.24 (b) for comparison. It can be observed that there is no obvious improvement of the result in (a) than that in (b) by using 3 more CCFs. The reason, we suppose, it that the CCFs with relatively small intervals like CCF(AB), CCF(BC) contribute little to the estimation. This would be discussed more in the next subsection.

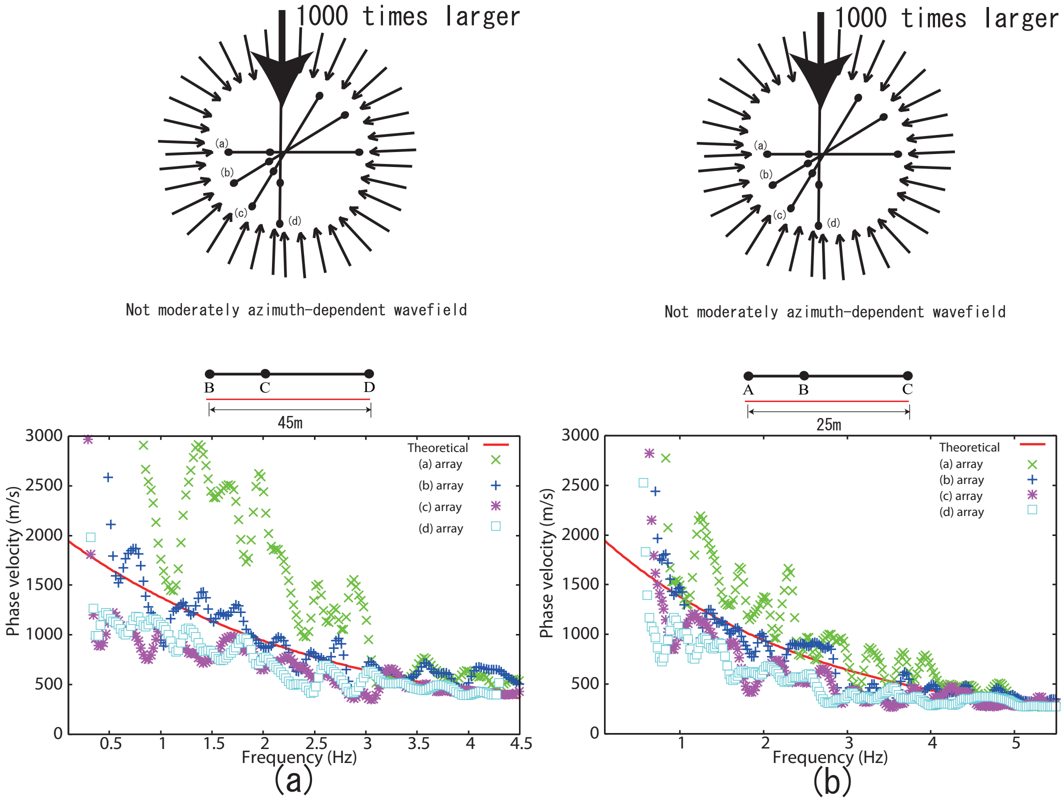


**Figure–2.26** Estimation of 4 3-site linear arrays with different direction in an extremely azimuth-dependent wavefield. Every linear arrays uses 3 sites. The red curve indicates the theoretical phase velocity. The curves with 4 different colors shows the estimation from (a), (b), (d), (d) array with different direction, repectively. In the wavefield, there is one wave in certain direction which has obviously larger power than others (1000times): (a) a large-scale linear array with $r_{max}$ of 45m; (b) a small-scale linear array with $r_{max}$ of 25m.

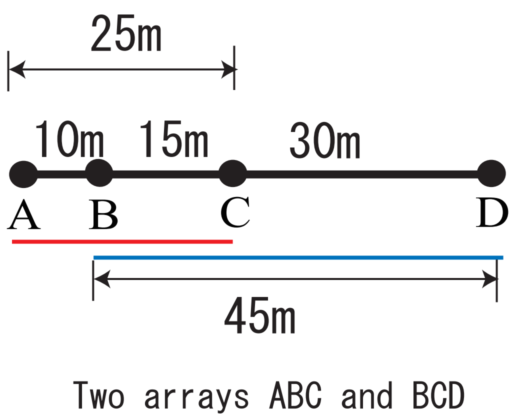


**Figure–2.25** a 4-site linear array regarded as 2 3-site arrays with $r_{max}$ of 25m and 45m, respectively.

There is another way to apply the advantage of 4-site array to the most advantage. As we discussed in section 2.3.3, the effective range is narrowed compared with SPAC method, namely, the $kr_{max}$ range of 1.3 to 2.8 and the frequency range of 3.0 to 4.2Hz. Hence, if we regard the 4-site array as two 3-array arrays, which have different $r_{max}$, the combination of estimations from the two 3-site arrays can produce a broader effective frequency range. For example, as Fig .2.23 (b) shows, the array ABCD can be divided into ABC and BCD, they both have the interval ratio of 1 : 2 but they have different $r_{max}$. If we use the proposed method to both arrays in Fig. 2.25, the combination of their estimations is shown in Fig. 2.26 (a) and (b). Estimation of 4 3-site linear arrays with different direction in an extremely azimuth-dependent wavefield. Every linear arrays uses 3 sites. The red curve indicates the theoretical phase velocity. The curves with 4 different colors shows the estimation from (a), (b), (d), (d) array with different direction, repectively. In the wavefield, there is one wave in certain direction which has obviously larger power than others, which is 1000times larger. (a) shows the estimations using a large-scale linear array with $r_{max}$ of 45m and (b) shows a small-scale linear array with $r_{max}$ of 25m. It can be seen that the effective frquency range is 3.0 to 4.2Hz for BCD array and 4.0 to 5.5 for ABC array. The total effective frequency range becomes 3.0 to 5.5Hz. It can be concluded that by applying the 4-site array in a “smart” way, the broader frequency range can be obtained. Be careful here that, the $kr_{max}$ range for each 3-site array is still 1.3 to 2.8.

### 2.4.2 Influence of the intervals among sensors

From the last subsection, we know that the 3-site linear array is the most fundamental and efficient array setting to apply the proposed method. It is a very simple shape. However, we have not discussed so far about the decisions of the intervals and its influence of the estimations. In this subsection, we will do numerical simulations continuingly in a 3-site linear array to do the related examination about it.

We set the $r_{max}$ to be 45m still and divide AB and BC in different ways because if referring to the left column in Fig. 2.10 the intervals are fixed to be 15m and 30m which has a ratio of 1: 2. The estimations are shown in Fig. 2.27. In order to be clear and easy describing, we set a parameter called $R_l$:

$$R_l = \frac{r_{BC}}{r_{AB}} \tag{2.31}$$

as an indicater of the array setting. We choose the value of $R_l$ to be 1.0, 1.5, 2.0 2.5, 3.0, 5.0 and 10.0 and the estimation results are shown in Figs. 2.27. Estimations with different value of $R_L$, 1.0, 1.5, 2.0, 2.5, 3.0, 5 and 10, are shown in (a), (b), (c), (d), (e), (f) and (g), repectively.

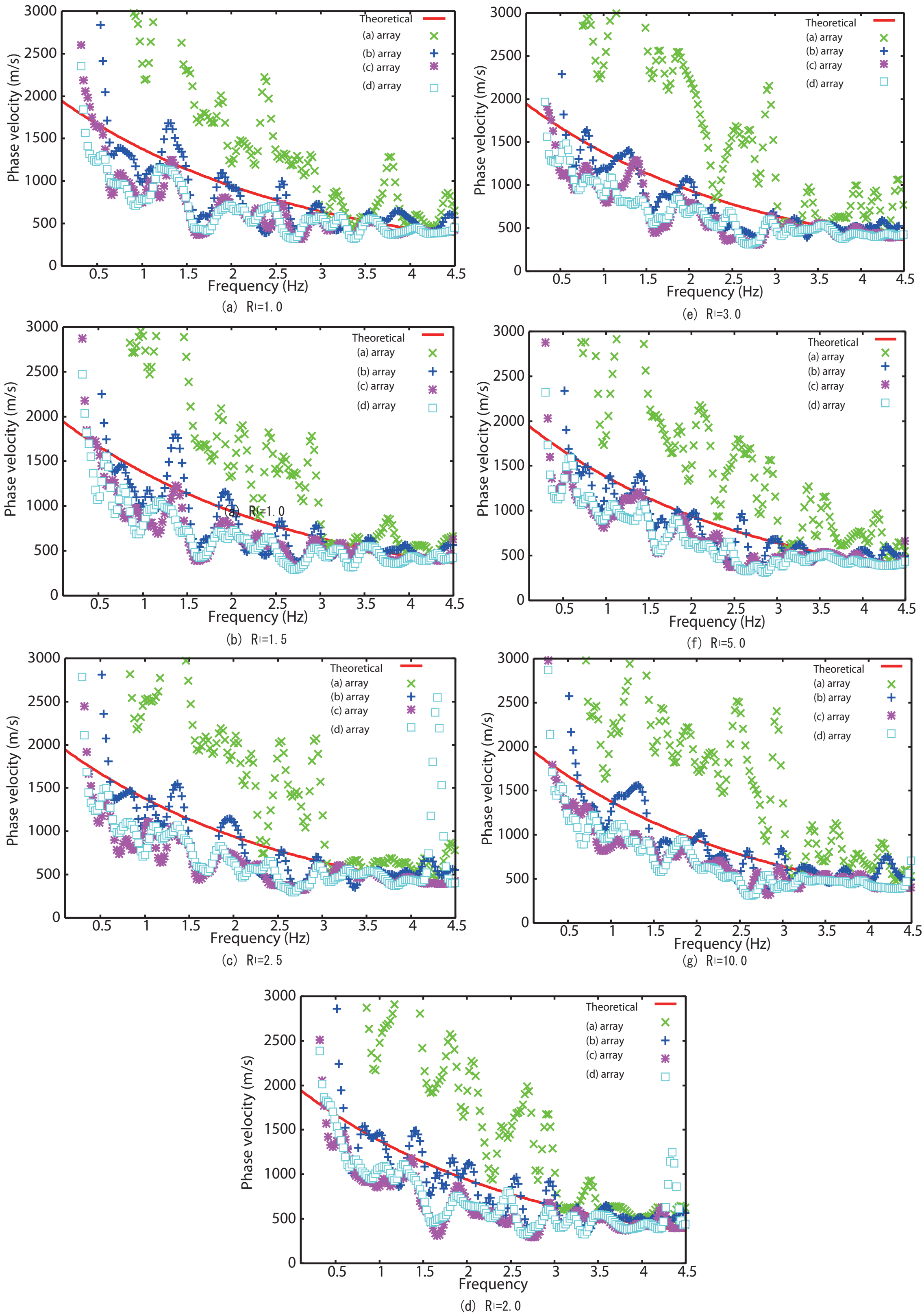


**Figure–2.27** Estimation of 4 3-site linear arrays with different direction in an extremely azimuth-dependent wavefield. Estimations with different value of $R_L$, 1.0, 1.5, 2.0, 2.5, 3.0, 5 and 10, are shown in (a), (b), (c), (d), (e), (f) and (g), repectively.

It can be seen that when $R_l = 1.0$, the estimation is unstable and bad in the frequency range of 3.0 to 4.0Hz, namely, $kr_{max}$ range of 1.3 to 2.8. It is easy understanding because when $R_l = 1.0$, it is intrinsically just 2 CCFs because the CCFs of AB and BC are the same due to the same interval. Hence, the accuracy is insufficient. In case of $R_l = 1.5, 2.0$, and 2.5, the estimation is relatively good especially for $R_l = 2.0$ or 2.5. When $R_l = 3.0$ or $R_l > 3.0$, the estimation becomes unstable again. This can be explained too: as the $R_l$ becomes larger, the ability of CCF with smallest interval, $r_min = \frac{r_{max}}{1+R_l}$, to contribute to the final estimation is more and more shifted to the low frequency range, thus causing the insufficiency of accuracy in high frequency range. However, be careful that after all, these analysis are based on the particular inversion technique we have used so far, which is GA with population of 10000 and evolution times of 20 plus PSO. Hence, we can summarize that under the current condition of inversion accuracy, the choise of interval in the case 3-site linear array should not be with too large of small $R_l$ value. It is recommended to be chosen as 1.5 to 2.5, best as around 2.0.

### 2.4.3 Influence of the incoherent noise the estimation

Here we discuss how the incoherent noise would have effect on the estimation results. This is very realistic in real cases that at each observation site, there are noise that is randomly happening. In order to do the analysis with a unifying standard, we assume the power of noise at each site to be the same and uncorrelated with each other. Hence we firstly assume the power of the noise using an ordinary indicator called the noise/signal ratio, $\epsilon(\omega)$, which is:

$$\epsilon = \frac{\int n(\omega)}{\int s(\omega)} \tag{2.32}$$

wherein the $n_\omega$ and $s_\omega$ indicate the power of noise and signal in frequency range, respectively. It is obvious that the cross spectra between each pair of sites will not change because the noise is uncorrelated with the signal and other noise. However, the power spectra at each site would be $(\epsilon + 1)$ times the original one. Hence finally, the estimation value of CCF $\gamma^e_{pq}$ would be:

$$\gamma^e_{pq} = \frac{1}{1+\epsilon}\gamma_{pq}, \tag{2.33}$$

which would be cause the value to be underestimated. It is difficult to judge simple about the tendency of the error of phase velocity because the inversion technique is not as simple as SPAC method. Hence, let us do the corresponding simulation about this. We add the noise wave to each site with the same power and see how the estimation will change in case of different $\epsilon(\omega)$. The result is shown in Fig. 2.28. Estimations with different value of $\epsilon$ from small to large are shown in figures (a) to (f), repectively.

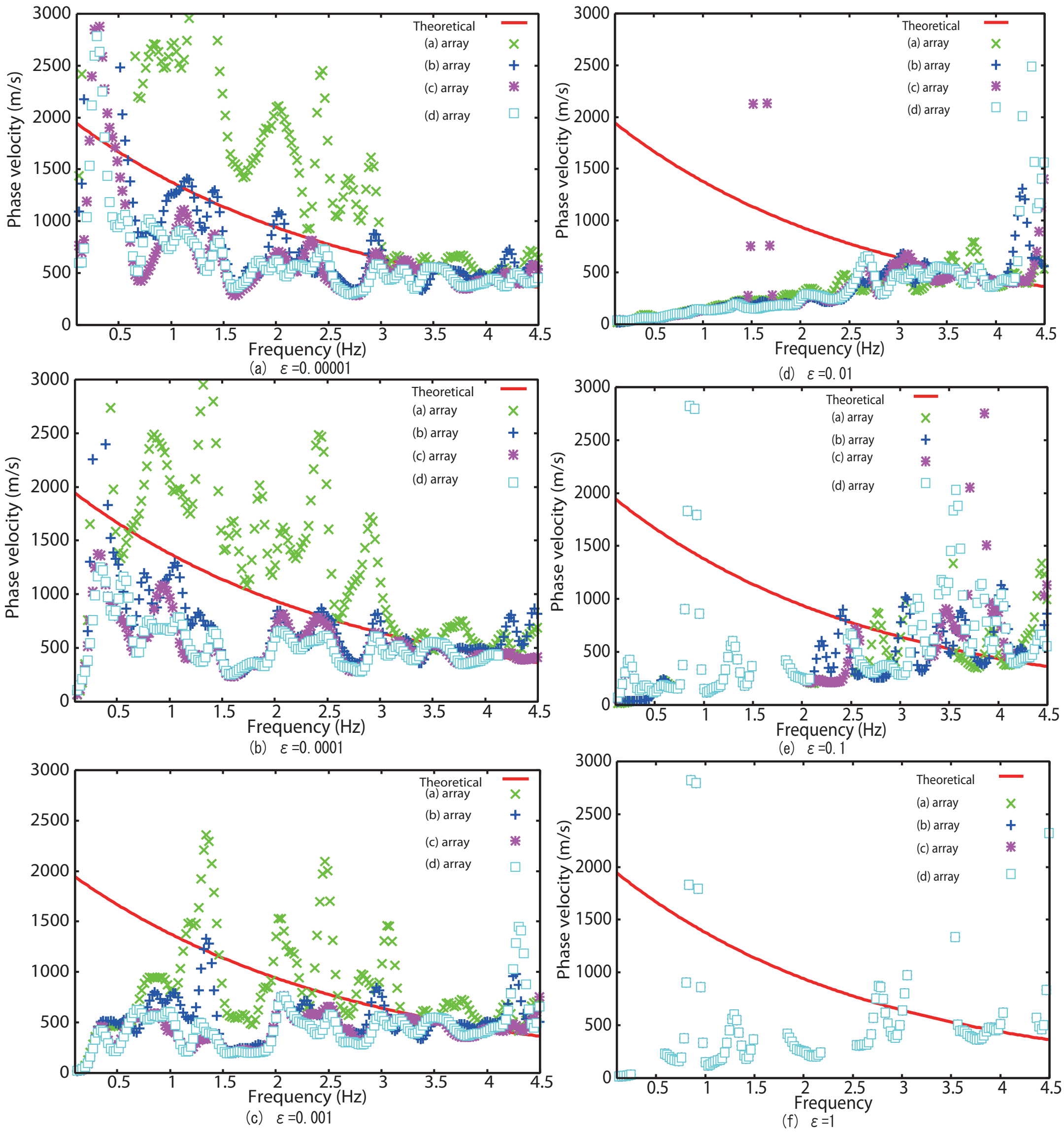


**Figure–2.28** Estimation of 4 3-site linear arrays with different direction in an extremely azimuth-dependent wavefield. Estimations with different value of $\epsilon$ from small to large are shown in figures (a) to (f), repectively.

It can be observed that (1) firsly, of course as the N/S ratio becomes larger, the estimation becomes worse and worse as expected. (2) Secondly, until the N/S ratio reaches 0.1, the estimation in frequency range of 3.0Hz to 4.2Hz, namely, $kr_{max}$ range of 1.3 to 2.8 is still quite consistently good and stable which shows the robustness of the accuracy in this range dealing with the uncorrelated noise. (3) Thirdly, the accuracy in the low frequency range is fragile because the sensitivity of estimation in this range is low.

### 2.4.4 Summary

From the above numerical simulations, there are some conclusions drawn as below.

- As for the site number, using 3-sites with $N_j = 3$ is optimal.
- As for the site intervals, the $R_L$ between 1.5 and 2.5 has best stability.
- When the signal/noise ratio is below 0.01, there is almost no bad influence on the estimations. When it increases over 0.1, the estimations would have large fluctuations.

## 2.5 Field test

### 2.5.1 Observation

We have applied the proposed technique to field tests in order to confirm the availability of the method. An observation was conducted on October 23, 2013 in the parking lot of Zoorasia Yokohama Zoological Gardens (ZRS) in Yokohama City, Japan as shown in Fig. 2.29(a). There is one KiK-net site[1] just nearby and the soil profile is available as shown in Fig. 2.29(b). We deployed 7 seismometers, whose type is KVS-300, moving-coil-type velocity sensors with a 2-Hz natural period, constituting two linear arrays as shown in Fig. 2.29(c). The two linear arrays form an angle of 60° so that the SPAC method could be applied for comparison. For both linear arrays, there are 4 sites with the intervals of 5m, 15m and 38m. For the SPAC method, observations with different array radiis, namely, 5m, 20m and 58m could be conducted .

[1]http://www.kyoshin.bosai.go.jp/cgi-bin/kyoshin/db/siteimage.cgi?0+KNGH10+kik+def

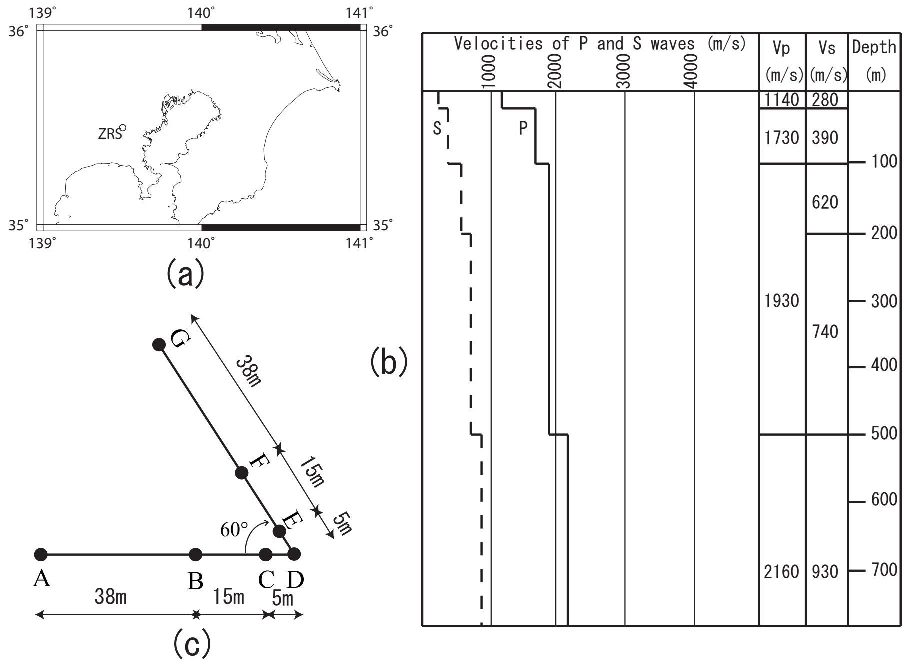


**Figure–2.29** Field tests. (a) Location of the field tests (b) Boring soil data (c) Arrangement of sensors.

The array sizes are decided by considering both the need for SPAC method and proposed method. The theoretical dispersion curve, the red curve, is shown in Fig. 2.30. If we choose the objective frequency range for estimation as 1.0 to 8.0 Hz, it is 700 to 40m in wavelength. According to the effective wavelength range of SPAC method, $2r$ to $10r$ in which $r$ is the array radius, we set the largest array size as $70m$ and the smallest array size as 20m. However, the biggest size is limited by the real size of the parking lot so we set the largest size as $58m$. However, if we conduct the proposed method using the interval of $38m$ and $20m$, the effective range would be limited by the largest intervals of $58m$, which would be too narrow. Hence, we set another site C or E between BD or DF. The intervals are set to be $5m$ and $15m$, which have an appropriate difference because we want 3 CCFs with different intervals.

For the proposd method, for simplicity, we only choose $BD$ as the linear array with intervals of $BD$, $BC$ and $CD$. Correspondingly, we choose $FD$ as the second linear array. For $J_0$ method, we choose $BD$ and $FD$ correspondingly. Measurements were conducted over a duration of 30 minutes at a sampling rate of 200Hz.

### 2.5.2 Results and discussions

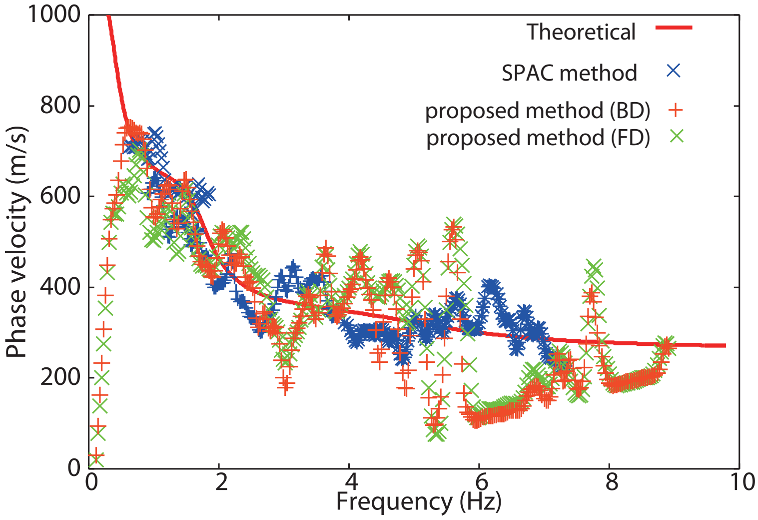


**Figure–2.30** Comparison between estimation of phase velocity using SPAC method and estimation using the proposed method in the field test. The red curve indicates the theoretical dispersion curve calculated from the soil profile. Blue dot indicates the estimation using SPAC methods from 3 equilateral arrays. Red dots and Green dots indicates the estimations from linear array BD and FD using proposed method, respectively. They are all in frequency range.

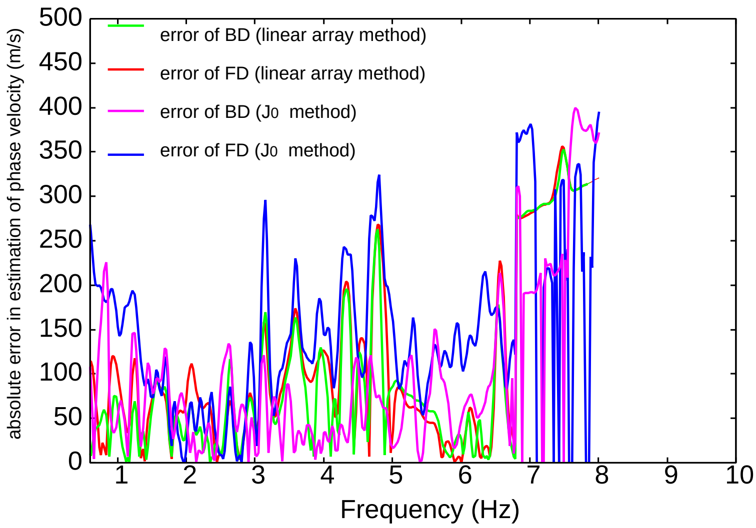


**Figure–2.32** The absolute difference $E_1$ between the estimated phase velocity and the theoretical velocity in each estimation. The horizontal axis is the frequency while the vertical axis shows the absolute error. Curves with color green, red, pink and blue indicate the error of linear array method using BD, linear array method using FD, $J_0$ method using BD and $J_0$ method using FD, respectively.

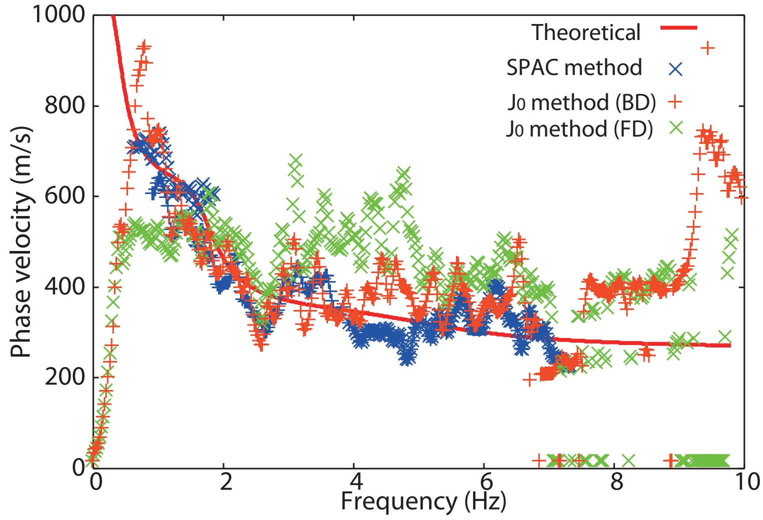


**Figure–2.31** Comparison between estimation of phase velocity using SPAC method and estimation using the $J_0$ method in the field test.The red curve indicates the theoretical dispersion curve calculated from the soil profile. Blue dot indicates the estimation using SPAC methods from 3 equilateral arrays. Red dots and Green dots indicates the estimations from 2-site BD and FD using $J_0$ method, respectively. They are all in frequency range.

**Table–2.1** The mean over all frequency range of the relative difference $\bar{E_1^{re}}$ between the estimated phase velocity and the theoretical velocity in each estimation corresponding to Fig. 2.32. They are grouped by high-frequency range and low-frequency ranges.

| | Frequency range ($kr$ range) | BD (linear) | FD (linear) | BD ($J_0$) | FD ($J_0$) |
|---|---|---|---|---|---|
| $\bar{E_1^{re}}$ | 1 to 3Hz (0.2 to 1.3) | 10% | 13% | 11% | 21% |
| | 3 to 8Hz (1.3 to 2.8) | 31% | 32% | 30% | 47% |

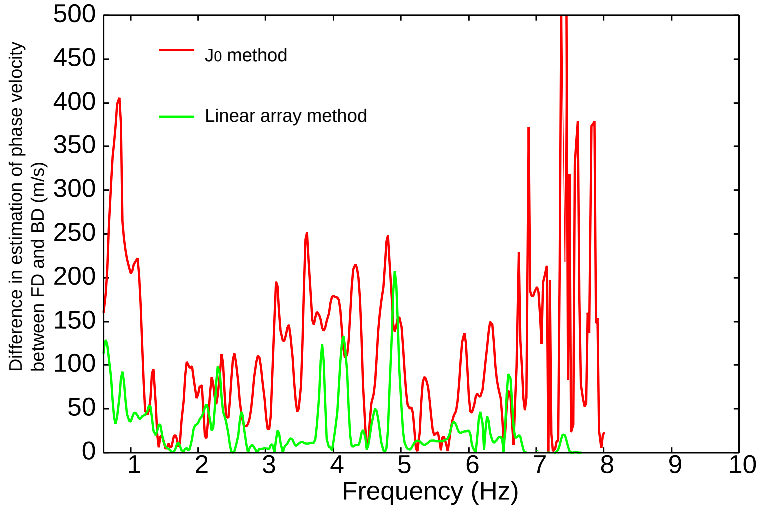


**Figure–2.33** The absolute difference $E_2$ between the estimated phase velocity from BD and FD in proposed method and $J_0$ method. The horizontal axis is the frequency while the vertical axis shows the absolute difference between BD and FD in each method. Red and Green curves indicate the absolute difference between estimations from BD and FD in $J_0$ method and linear array method, respectively.

**Table–2.2** The mean of relative difference $\bar{E_2^{re}}$ over all frequency range of the absolute difference between estimations from BD and FD in each estimation

| | Proposed method | $J_0$ method |
|---|---|---|
| $\bar{E_2^{re}}$ | 10% | 31% |

We extracted a certain number of segments from the seismograms, worth 40.96$s$, which have a filtered range of 0.2 to 10.0Hz. Then, we took the average of the cross-spectra and the power spectra and smoothed them with a Parzen window with a bandwidth of 0.2Hz. The resulting cross spectra and power spectra are substituted into Eq. 2.11 to apply the SPAC method and into Eqs. 2.17 and 2.18 to apply the proposed method. The results are shown in Fig. 2.30 with analytical dispersion curve obtained from the soil profile as shown in Fig. 2.29. The red curve indicates the theoretical dispersion curve calculated from the soil profile. Blue dot indicates the estimation using SPAC methods from 3 equilateral arrays. Red dots and Green dots indicates the estimations from linear array BD and FD using proposed method, respectively. They are all in frequency range. The results from $J_0$ method using $BD$ and $FD$, respectively, are shown in Fig. 2.31. Red dots and

Green dots indicates the estimations from 2-site BD and FD using $J_0$ method, respectively. Besides, in order to see the similarities between each estimation and the theoretical phase velocity, the absolute error $E_1$ for each estimation is shown in Fig. 2.32. The horizontal axis is the frequency while the vertical axis shows the absolute error. Curves with color green, red, pink and blue indicate the error of linear array method using BD, linear array method using FD, $J_0$ method using BD and $J_0$ method using FD, respectively. $E_1$ is calculated by $E_1 = |c_{esti} - c_{theo}|$ in which $c_{esti}$ is the estimated phase velocity and $c_{theo}$ is the theoretical one. The mean of the relative error $\bar{E_1^{re}}$ over all frequency range of 0.5 to 8.0Hz is calculated and shown in Table 2.1. They are grouped by high-frequency range and low-frequency ranges. The $\bar{E_1^{re}}$ is calculated by $\bar{E_1^{re}} = \frac{\int E_1}{\int c_{theo}}$. Also, we calculated the absolute difference $E_2$ between the estimation from BD and FD in both methods to show the robustness of each method. The result is shown in Fig. 2.33. The horizontal axis is the frequency while the vertical axis shows the absolute difference between BD and FD in each method. Red and Green curves indicate the absolute difference between estimations from BD and FD in $J_0$ method and linear array method, respectively. $E_2$ is calculated by $E_2 = |c_{BD} - cFD|$ in which $c_{BD}$ is the estimated velocity from BD array and $c_{FD}$ is the estimated velocity from FD array. The corresponding mean of relative difference $\bar{E_2^{re}}$ over all frequency range is calculated in Table 2.2. $\bar{E_2^{re}}$ is calculated by $\bar{E_2^{re}} = \frac{\int E_2}{\int c_{BD}}$

For the SPAC method, it is observed that the estimation matches the theoretical one well in the frequency range of 0.6 to 7.0Hz, namely, $kr$ range of 0.2 to 3.2. It matches with the past research [14]. For the proposed method, the estimation matches well in the frequency range of 1.0 to 6.0Hz for the linear array as shown in Fig. 2.30. In the $kr_{max}$ range, it is 0.5 to 2.8, respectively. Let us go back to see the estimations in the numerical simulation shown in Figs. 2.16 and 2.18. We can see that in numerical simulation, the estimation has different accurate range, which is $kr_{max}$ range of 1.3 to 2.8. In this field test, the estimation in $kr$ range of 1.3 to 2.8, namely, frequency range of 3.0 to 8.0Hz has quite large fluctuation. One reason to cause the difference is the difference of wavefield. In the field test, the wavefield cannot be perfectly stationary or as simple as that in the numerical simulation. The uncorrelated noise or the coherent noise, namely, not caused by plane Rayleigh wave, in high frequency range also may have bad influence on the result. As shown in Figs. 2.30 and 2.32, in high frequency range, there is quite large fluctuation. It may comes from the defect of the inversion technique. The influence caused by uncorrelated noise and the defect of inversion technique would be discussed later. Though, it can be seen that in $kr$ range of 1.3 to 2.8 the mean value

However, we can see that the estimation from the two linear arrays coincides with each other, which demonstrates the robustness of the proposed method agaist the azimuth. On the other hand, the $J_0$ method behaves quite differently according to the azimuth as shown in Fig. 2.31. The difference between two methods is obvious by seeing Fig. 2.33 and Table 2.2. The accuracy of $J_0$ method is also worse than the proposed method as shown in Fig. 2.32 and Table 2.1.

Though it seems that one of the two estimations using $J_0$ method coincides with the theoretical one, the lack of robustness makes it difficult to be available in real cases. The proposed method is not available in any wavefield as discussed in the former section. However, because of taking $J_2$ and $J_4$ terms into consideration, it can be applied with more stability and reliability than $J_0$ method in real cases. This is confirmed at least by this field test.

## 2.6 Summary

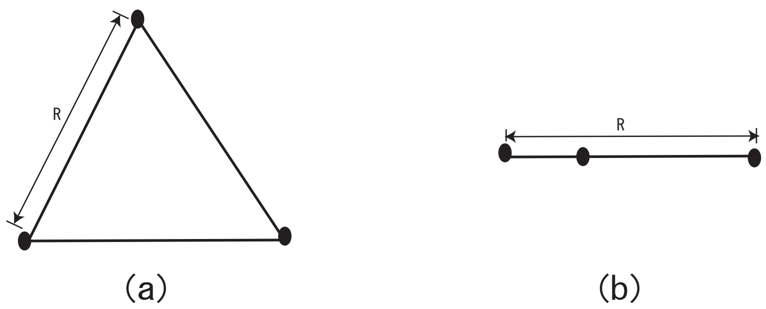


**Figure–2.34** (a) SPAC method with simple shape (b) linear array

In this chapter, we have proposed a new method for estimating the phase velocity of Rayleigh waves. Using the discrete formula of CCF, we can use a linear array to do the estimation. This can be applied to many urban areas where the circular arrays are difficult to set. There are several conclusions drawn below.

- In case of extremely azimuth-dependent wavefield (uni-directional wave), the proposed method is available when the angle between the wave and linear array is at least smaller than 60°. Compared to $J_0$ method, the proposed method has wider applicable range.

- In case of moderately and not moderately azimuth-dependent wavefield, only one linear array is enough to obtain accurate simulation. Compared to $J_0$ method, the proposed method has wider applicable range. The stable available range of $kr_{max}$ is analyzed to be 1.3 to 2.8.

- Lots of discussions have been done on the possible factors which may have influence of the estimation accuracy. Through these analysis, we confirm the necessity of using at least 3 CCFs and up to $J_4$ term in order to obtain an acceptable accuracy. And the intervals of linear array also should be carefully chose. The best $R_l$ value should be around 2. The case in which incoherent noise exists is also analysed.

- Through the field test, the proposed method can obtain the same accurate estimation as SPAC method and is stable regardless of azimuth while the $J_0$ method does not work properly.

- As a whole, the research of the linear array method can be regarded as a improvement or complement to the past research about developing microtremor methods with simple arrays. Though it has narrower effective frequency range than SPAC method and even cannot be said to have more convenient shape than SPAC method as shown in Fig. 2.34, it offers another choice of very shape, which is simple, in practical observations. Even as the same linear array method, it has firmer theoretical background than $J_0$ method and L-shape method. The site number required is much smaller than ReMi method but be careful again that it is meaningless to compare ReMi method with microtremor method applying just Rayleigh or Love waves.

Moreover, as for the mainly mentioned microtremor survey method in this chapter, SPAC method, $J_0$ method and the proposed method. We draw a table to describe their stablity, effective scope and convenience as Table 2.3 shows.

**Table–2.3** The comparison of SPAC method, proposed method and $J_0$ method in convenience, effective scope and stability

| | SPAC method | Proposed method | $J_0$ method |
|---|---|---|---|
| Effective scope (in $kr$ range) | 0.6 to 3.1 | 1.3 to 2.8 | 0.6 to 3.1 |
| Minimal requirement of array setting | 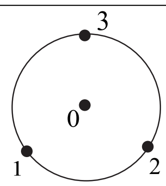 | 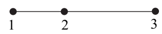 |  |
| Available wavefield | any | not 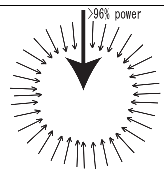 | only 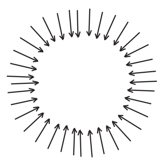 |

# 3

# A new perspective of vertical spectral ratio between 2 sites by the seismic interferometry

## 3.1 Introduction

Since Aki [10] proposed a new approach to estimate phase velocities of surface waves, spatial auto-correlation (SPAC) method has been a very useful tool to estimate ground structure because of its simple post-process. After that, many researchers both in and out of Japan continued to publish papers to extend Aki's theory and developed a variety of array methods [11,14,18,24,28,29,37]. However, in all those improved methods, the layers under surface can only be assumed to be horizontal while in fact, the layers are likely to be inclined. In other words, the lateral heterogeneity cannot be detected using all the array methods above. Hence, it is expected to obtain more detailed information of ground structure such as inclination by making better use of the records.

In recent years, the seismic interferometry (SI) theory has also been widely used to estimate ground structure. It is proved that in an elastic medium the Fourier transform of azimuthal average of the cross correlation of motion between two sites is proportional to the imaginary part of the Green's function (IOG) between the two sites in frequency domain [33,48–53,60]. Hence, it becomes possible to calculate the ratio of imaginary part of different Green's function by taking the ratio of corresponding cross correlation to analyze ground structure more particularly because Green's function indicates intrinsic property of the medium.

The horizontal-to-vertical spectral ratio (H/V) method has been proved equivalent to the ratio of IOG in the horizontal and vertical direction in diffuse wavefield [33, 61]. We can say that the H/V spectral ratio is successfully reinterpreted and becomes more revealing using seismic interferometry. Moreover, seismic interferometry is consistent with the SPAC method [32,56,62] in diffuse wavefield, which forms the base of using seismic interferometry theory to array methods based on the SPAC method. Hence, it is available to just apply H/V spectral ratio method to each site in array methods to distinguish the difference of ground structure among all observation sites.

On the other hand, we consider using spectral ratio of only vertical component between two sites to detect the lateral heterogeneity. There are two advantages compared with H/V spectral ratio method: first, only vertical component is used in both array method and the calculation of spectral ratio, which is more convenient for observation and data analysis; second, the spectral ratio taken between two sites has the potential to demonstrate the lateral heterogeneity more clearly and directly than taking H/V spectral ratio site to site and doing comparison. According to seismic interferometry, the spectral ratio taken between two sites is equivalent to the corresponding ratio of IOG. IOG is independent of the wavefield and can be calculated out as long as the ground structure between two sites are known [63, 64]. Hence, inversely, by knowing the vertical component spectral ratio, the difference of ground structure between two sites, namely, the lateral heterogeneity is expected to be detected.

It must be claimed that the application of spectral ratio between two sites is not a new idea. At first, the Fourier amplitude spectra of horizontal components at a site has been used to identify the resonance peak of the soil layer, which is proposed by Kanai and Tanaka [65]. Afterwards, the method to apply spectral ratio between two sites has also been developed decades ago by Kagami et al. [66]. If one site is on the rock (reference site) and one is on soil, by taking the spectral ratio between them, the resonance of the soil layer can be detected. However, there are three disadvantages of this theory: first, this method is based on the assumption that the motion at the reference site should be representative of the excitaion arriving at the interface of soil layer and base [9]; second, this method confines the two sites to be on the soil and on the rock, which lacks the generality to detect the lateral heterogeneity; third, this theory is based on the assumption of 1D ground

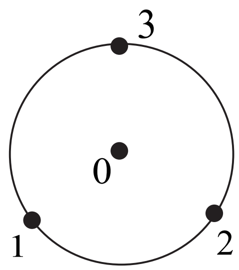


**Figure–3.1** Geometry used in conventional SPAC method

structure. Moreover, horizontal components are usually used in this method. Instead, we regard vertical component spectral ratio between two sites as the ratio of imaginary part of Green's function. The wavefield just needs to be diffuse and the two sites have no limitations. Hence, it not only gives a new perspective of the spectral ratio between two sites but also becomes a general indicator of lateral heterogeneity.

In this chapter, first we will introduce the theoretical background and propose the new perspective of vertical component spectral ratio between two sites. For convenience, we use the ratio of power spectra to replace spectral ratio or we say, ratio of Fourier spectra. Then, we will use a simple inclined 2-layered model based on finite difference method (FDM) [67] to discuss how the vertical component ratio of IOG between 2 sites will behave under simple lateral heterogeneity. Next, we use FDM to create a diffuse wavefield in the same model. In this wavefield, we calculate the vertical component spectral ratio among sites in a linear array and examine whether they coincide with the theoretical ratio of IOG, respectively.

## 3.2 Theoretical background

In this chapter, the basic knowledge of array methods and seismic interferometry will be introduced and our new concept of combining them two will be proposed.

### 3.2.1 A simple introduction of array methods

For simplicity, we introduced the typical array method, SPAC method here. Given an equilateral-triangle array and vertical time series records of microtremors at four sites under the assumption of temporally and spatially stationary wavefield, the azimuthal-average of spatial auto-correlation coefficients $\rho(\frac{r\omega}{c(\omega)})$ can be calculated as:

$$\rho(\frac{r\omega}{c(\omega)}) = \frac{1}{3}\sum_{j=1}^{3}\frac{S_{0j}(\omega)}{\sqrt{S_{00}(\omega)S_{jj}(\omega)}}, \tag{3.1}$$

where $\omega$, $r$ and $c(\omega)$ are the angular frequency, radius of the circular array and phase velocity, respectively. $S_{jj}(\omega)$ and $S_{0j}(\omega)$ are the power spectra of vertical component of microtremors at site $j$ ($j = 0, 1, 2, 3$) and the cross spectra of the vertical records between site $j$ and 0. The site 0 is center of the array and sites 1, 2, and 3 are located on the circle as shown in Fig. 3.1.

Practically, $S_{jk}(\omega)$ is obtained by the product of Fourier transformation $F(\omega, X_j)$ of records at two sites as

$$S_{jk}(\omega) = F(\omega, X_j)F^*(\omega, X_k), \tag{3.2}$$

where $X_j$ is a location of site $j$ and $^*$ stands for the complex conjugate.

Afterwards, a dispersion curve can be obtained and the property of under-surface layers are estimated using certain inversion technique.

### 3.2.2 Seismic interferometry

The retrieval of Green's function from cross correlation is called seismic interferometry. This mechanics has been widely used to estimate long-distance ground structure. In order to satisfy the condition of seismic interferometry, the wavefield must be diffusive, in other words, the energy is equipartitioned among all the possible states like wave kind or propagation direction. The provement of seismic interferometry for homogeneous elastic medium in 2D scalar case is shown below. [51]

We assume we are dealing with SH waves in a homogeneous elastic medium. Propagation takes place in $x$-$z$ plane as shown in Fig. 3.2. The antiplane displacement $v(\overrightarrow{X}, t)$ satisfy the wave equation:

$$\frac{\partial^2 v}{\partial x^2} + \frac{\partial^2 v}{\partial z^2} = \frac{1}{\beta^2}\frac{\partial^2 v}{\partial t^2} \tag{3.3}$$

where $\beta$ is shear wave velocity and $t$ is time. $k$ is the wavenumber $k = \frac{\omega}{\beta}$. A typical

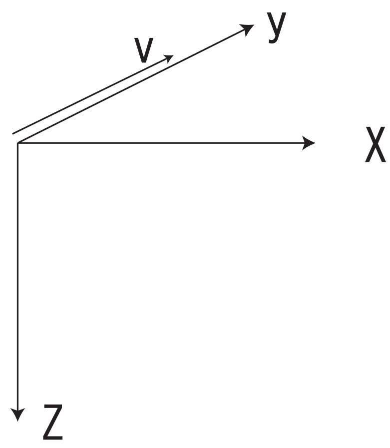


**Figure–3.2** The $X - Z$ plane and the direction of $v$

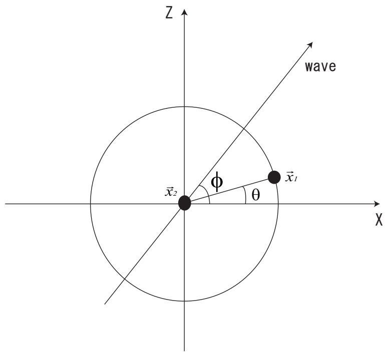


**Figure–3.3** The azimuthal relationship between $\overrightarrow{x}$ and the wave direction in the $X - Z$ plane

homogeneous plane wave can be written as:

$$v(\overrightarrow{X}, \omega, t) = F(\omega, \phi)exp[-ik(xn_x + zn_z)]exp(i\omega t) \tag{3.4}$$

in which $k$ is the wavenumber, $F(\omega, \phi)$ is complex waveform, $\phi$ indicates the azimuth of wave, $\omega$ is circular frequency, $\overrightarrow{x} = (x, z)$ and $n_x$ and $n_z$ is direction cosines which define wave propagation. $i$ indicates $\sqrt{-1}$.

Then take two different position $\overrightarrow{X_1}$ and $\overrightarrow{X_2}$, assuming $\overrightarrow{X_2}$ is at the origin, and calculate the cross spectra:

$$\begin{aligned} &v(\overrightarrow{X_2}, \omega)v^*(\overrightarrow{X_1}, \omega) \\ &\quad = F(\omega, \phi)F^*(\omega, \phi)exp(ikrcos[\phi - \theta]), \end{aligned} \tag{3.5}$$

where $\theta$ indicates the azimuth of $\overrightarrow{X_1}$ as for $x_1 = rcos\theta$ and $z_1 = rsin\theta$ as shown in Fig. 3.3.

Assume the spectral density $F(\omega)$ roughly independent of $\phi$, then an azimuthal average over $\phi$ is:

$$\begin{aligned}&< v(\overrightarrow{X_2},\omega)v^*(\overrightarrow{X_1},\omega) >\\&= |F(\omega)|^2\tfrac{1}{2\pi}\int_0^{2\pi} exp(ikrcos[\phi-\theta])d\phi\\&= |F(\omega)|^2 J_0(kr)\end{aligned} \tag{3.6}$$

where $J_0$ is Bessel function of the first kind of order zero.

Considering now the Green's function in the frequency domain:

$$G_{yy}(\overrightarrow{X_1},\overrightarrow{X_2},\omega) = \frac{1}{4}i\mu[J_0(kr) - iY_0(kr)]. \tag{3.7}$$

To introduce the basic concept of Green's function firstly, $G_{lm}(\overrightarrow{X_1},\overrightarrow{X_2},\omega)$ indicates the $l$ direction response at $\overrightarrow{X_1}$ when a unit force in $m$ direction is exerted at $\overrightarrow{X_2}$. Then, in Eq. 3.7, $Y_0(kr)$ indicates the Neumann function in the frequency domain. $\mu$ indicates the shear modulus. $yy$ shows the response and exerted force are both in $y$ direction. From Eqs.(3.6) and (3.7), substituting the energy density of SH wave $E_{SH} = \rho\omega^2|F(\omega)|^2/2$, where $\rho$ is the density of medium, into it, finally we obtain:

$$\begin{aligned}&< v(\overrightarrow{y},\omega)v^*(\overrightarrow{x},\omega) >\\&= -8E_{SH}k^{-2}\Im[G_{yy}(\overrightarrow{x},\overrightarrow{y},\omega)]\end{aligned} \tag{3.8}$$

Above shows the approvement of 2D scalar case in homogeneous layered medium. However, even in inhomogeneous medium and in 3D vector case, the retrieval of Green's function is still available [53].

To be more general, it has been demonstrated [51] that in an elastic medium, the averaged cross correlation of motions at sites 1 and 2, whose locations are $X_1$ and $X_2$, can be written as:

$$\begin{aligned}&< F_\ell(\omega,\overrightarrow{X_1})F_m^*(\omega,\overrightarrow{X_2}) >\\&= -2\pi E_s k^{-3}\Im[G_{\ell m}(\overrightarrow{X_1},\overrightarrow{X_2},\omega)],\end{aligned} \tag{3.9}$$

where $\ell$ and $m$ indicate one of three directions, $(x, y, z)$. Be careful here that we changed to the way of using $x, y, z$ to show the 3 directions. $k$ and $E_s$ are wave number of shear wave and the averaged energy density of shear wave, respectively. $< \cdot >$ stands for an expectation and $\Im[\cdot]$ for the imaginary part. For the convenience for indication from now on, we abbreviate the symbol $\rightarrow$ to stand for vector, so the equation becomes:

$$
\begin{aligned}
&< F_\ell(\omega, X_1) F_m^*(\omega, X_2) > \\
&\quad = -2\pi E_s k^{-3} \Im[G_{\ell m}(X_1, X_2, \omega)],
\end{aligned}
\tag{3.10}
$$

Similar with the SPAC method, many other researchers also has written reports about the retrieval of Green's function by different methods. For example, Wapenaar and Fokkema [50] has also pointed out the same result as Eq. 3.10 under the different assumption. Normally, it is considered that the assumption of equipartition, i.e.,

> In the phase space the available energy is equally distributed with a fixed average amount among all the possible states.

is necessary for the retrieval of the elastodynamic Green's function from the diffusive wavefield [51]. However, in Wapenaar and Fokkema's paper, diffusive wavefield is not necessary assumption while 'uncorrelated point sources' becomes the condition. The relationship between the two assumption remains to be discussed. However, it is beyond the scope of this paper. In this article, we create diffusive wavefield for the use of Eq. 3.10. The diffusive wavefield will be made by setting random sources of random number at random sites at each timestep. The details will be explained in Chapter later.

### 3.2.3 A new perspective of ratio of power spectra between two sites

Now we constitute a vertical component ratio of power spectra through Green's function. Both of $\ell$ and $m$ of Eq. 3.10 are set as vertical direction, which is $z$, and sites 1 and 2 as the same sites. Hence, it becomes

$$
< F_z(\omega, X_1) F_z^*(\omega, X_1) >= -2\pi E_s k^{-3} \Im[G_{zz}(X_1, X_1, \omega)] \tag{3.11}
$$

The left-hand side becomes the power spectra at one site and according to the right-hand side, the power spectra contains information about both the strength of the wavefield, $E_s$,

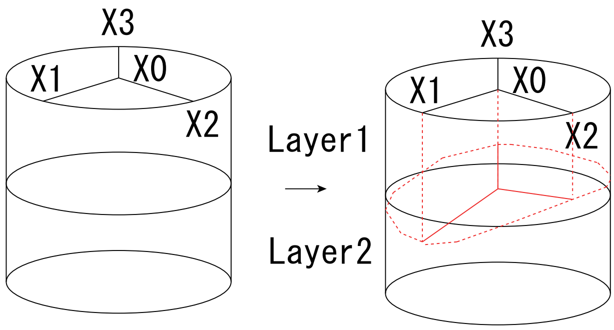


**Figure–3.4** The simple image of how the vertical spectral ratio helps to detect the lateral heterogeneity

and intrinsic property of ground structure, $\Im[G_{zz}(X_1, X_1, \omega)]$. Now it is required to extract out only the required part which is the Green's function and remove unknown values of parameters such as $E_s k^{-3}$. Hence we take the ratio of the power spectra at center of the array and an azimuthal site. As a result, the corresponding ratio of IOG can be obtained as

$$\frac{S_{jj}(\omega)}{S_{00}(\omega)} = \frac{\Im[G_{zz}(X_j, X_j, \omega)]}{\Im[G_{zz}(X_0, X_0, \omega)]} \tag{3.12}$$

and it is expected to analyze the lateral heterogeneity between two sites.

If we apply Eq. (3.12) to SPAC method in the simplest equilateral-triangle case, for example, three ratios $\frac{S_{11}(\omega)}{S_{00}(\omega)}, \frac{S_{22}(\omega)}{S_{00}(\omega)}, \frac{S_{33}(\omega)}{S_{00}(\omega)}$ can be obtained to analyze the lateral heterogeneity. Moreover, it is convenient and efficient to calculate this ratio because the power spectra is just the intermediate result in the process of SPAC method. Of course, this concept is not limited to SPAC method but available to any pair of sites in the diffuse wavefield. A simple image of applying these ratios to improve the 2-D layered structure is shown in Fig. 3.4.

### 3.2.4 Simulation of seismic wave using finite difference method

In order to simulate proper wavefield to examine the validity of the new method, we use the code for finite difference method developed by Sakai [68]. All the details are written in his paper. However, it is worth introducing some basic concept of this method here so that it will be easy to understand the way of using it later in this chapter. In case of wave propagating in elastic medium, the equation of motion and the stress-strain equation must

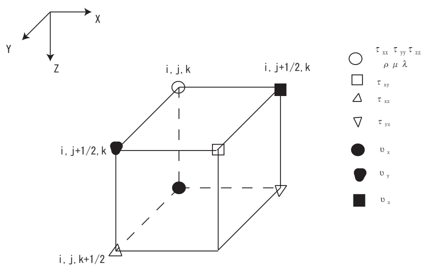


**Figure–3.5** Staggered grid

be satisfied as shown below:

$$\rho u_{i,tt} = \tau_{ij,j} + f_i \tag{3.13}$$

$$\tau_{ij} = \lambda u_{k,k}\delta_{ij} + \mu(u_{i,j} + u_{j,i}), \tag{3.14}$$

where $t$ indicates time, $\delta_{ij}$ indicates the Kronecker's delta, u displacement. $\rho$ density of medium, $\Lambda$ and $\mu$ the Lame constants, $f$ the body force. $u_{i,tt}$ demonstrates the 2nd order differential of $u$ with respect to $t$, namely, $\dfrac{\partial^2 u}{\partial t^2}$, $\tau_{ij,j}$ indicating $\dfrac{\partial \tau_{ij}}{\partial x_j}$.

Transforming the displacement to velocity, it becomes:

$$v_{i,tt} = b(\tau_{ij,j} + f_i) \tag{3.15}$$

$$\tau_{ij,t} = \lambda v_{k,k}\delta_{ij} + \mu(v_{i,j} + v_{j,i}) \tag{3.16}$$

where $b$ indicating the reciprocal of $\rho$. $\lambda$ and $\mu$ show the Lame constants.

From Eqs.(3.15) and (3.16), we can find that all the spatial differential is the first order. In order to make the finite difference method work with good precision, we use the staggered grid and central differential method. Fig.3.5 shows the arrangement of each variable at each position.

In Eq(.3.15) and Eq.(3.14), the differential with respect to time is also of first order so that either stress or velocity can be discretized in the same way. It is shown below how Eq.(3.15) will be discretized with respect to time and position.

$$
\begin{aligned}
{v_x}_{i+\frac{1}{2},j,k}^{n+\frac{1}{2}} &= {v_x}_{i+\frac{1}{2},j,k}^{n-\frac{1}{2}} + \Delta t[\bar{b_x}(D_x\tau_{xx} + D_y\tau_{xy} + D_z\tau_{xz} + f_x)]_{i+\frac{1}{2},j,k}^{n} \\
{v_y}_{i,j+\frac{1}{2},k}^{n+\frac{1}{2}} &= {v_y}_{i,j+\frac{1}{2},k}^{n-\frac{1}{2}} + \Delta t[\bar{b_y}(D_x\tau_{xy} + D_y\tau_{yy} + D_z\tau_{yz} + f_y)]_{i,j+\frac{1}{2},k}^{n} \\
{v_z}_{i,j,k+\frac{1}{2}}^{n+\frac{1}{2}} &= {v_z}_{i,j,k+\frac{1}{2}}^{n-\frac{1}{2}} + \Delta t[\bar{b_x}(D_x\tau_{zx} + D_y\tau_{zy} + D_z\tau_{zz} + f_z)]_{i,j,k+\frac{1}{2}}^{n},
\end{aligned}
\tag{3.17}
$$

where the superscript shows the time and the subscript show the position. $\Delta t$ indicates the time interval for iteration. $D_i$ is the approximation of partial differential in $i$ direction. $\bar{b}_i$ is the average of reciprocal of density obtained in $i$ direction.

Similarly, Eq.(3.16) is dicretized. The normal stress is:

$$
\begin{aligned}
{\tau_{xx}}_{i,j,k}^{n+1} &= {\tau_{xx}}_{i,j,k}^{n} + \Delta t[(\lambda + 2\mu)D_x v_x + \lambda(D_y v_y + D_z v_z)]_{i,j,k}^{n+\frac{1}{2}} \\
{\tau_{yy}}_{i,j,k}^{n+1} &= {\tau_{yy}}_{i,j,k}^{n} + \Delta t[(\lambda + 2\mu)D_y v_y + \lambda(D_x v_x + D_z v_z)]_{i,j,k}^{n+\frac{1}{2}} \\
{\tau_{zz}}_{i,j,k}^{n+1} &= {\tau_{zz}}_{i,j,k}^{n} + \Delta t[(\lambda + 2\mu)D_z v_z + \lambda(D_y v_y + D_x v_x)]_{i,j,k}^{n+\frac{1}{2}},
\end{aligned}
\tag{3.18}
$$

The shear stress is:

$$
\begin{aligned}
{\tau_{xy}}_{i+\frac{1}{2},j+\frac{1}{2},k}^{n+1} &= {\tau_{xy}}_{i+\frac{1}{2},j+\frac{1}{2},k}^{n} + \Delta t[\bar{u}_{xy}^{H}(D_y v_x + D_x v_y)]_{i+\frac{1}{2},j+\frac{1}{2},k}^{n+\frac{1}{2}} \\
{\tau_{xz}}_{i+\frac{1}{2},j,k+\frac{1}{2}}^{n+1} &= {\tau_{xz}}_{i+\frac{1}{2},j,k+\frac{1}{2}}^{n} + \Delta t[\bar{u}_{xz}^{H}(D_z v_x + D_x v_z)]_{i+\frac{1}{2},j,k+\frac{1}{2}}^{n+\frac{1}{2}} \\
{\tau_{yz}}_{i,j+\frac{1}{2},k+\frac{1}{2}}^{n+1} &= {\tau_{yz}}_{i,j+\frac{1}{2},k+\frac{1}{2}}^{n} + \Delta t[\bar{u}_{yz}^{H}(D_y v_z + D_z v_y)]_{i,j+\frac{1}{2},k+\frac{1}{2}}^{n+\frac{1}{2}}
\end{aligned}
\tag{3.19}
$$

In staggerred grid, every variable is well arranged at certain position, the spatial differential of variable $f(x)$ is obtained from adjacent $f(x \pm \frac{1}{2}dx)$, $f(x \pm \frac{3}{2}dx)$, $f(x \pm \frac{5}{2}dx)$ and so on.

$$
D_x f(x) = \frac{1}{\Delta x}\sum_{m=1}^{\frac{M}{2}} a_m[f(x + (m - \frac{1}{2})dx) - f(x - (m - \frac{1}{2})dx)]
\tag{3.20}
$$

where $M$ is the order of finite difference approximation and $a_m$ is the approximation coefficient. In my research, $M = 2$ with respect to time and $M = 4$ with respect to space.

According to Sakai [68], in 3-dimensional analysis with the order of finite difference approximation $M = 4$, the stability condition is:

$$
\Delta t < 0.495\frac{dh_{min}}{v_{max}}
\tag{3.21}
$$

where $dh_{min}$ is the minimum grid interval of $x, y, z$ axis and $v_{max}$ is the maximum P-wave velocity.

**Table–3.1** The parameters of the 2-layered medium

| Layer | P-wave velocity [m/s] | S-wave velocity [m/s] | Density [t/m$^3$] | Thickness [m] |
|---|---|---|---|---|
| 1 | 800 | 400 | 1.5 | 720 to 1280 |
| 2 | 1800 | 1200 | 2.0 | $\infty$ |

As for the result of calculation, records of frequency higher than certain value $f_c$ are cut out because the mesh size is limited after all. With the order of finite difference approximation $M = 4$, $f_c$ satisfies:

$$f_c = \frac{v_{min}}{5dh_{max}} \tag{3.22}$$

in which $dh_{max}$ is the maximum grid interval of $x, y, z$ axis and $v_{min}$ is the minimum S-wave velocity.

## 3.3 The influence of lateral heterogeneity on the ratio of IOG

### 3.3.1 For a particular layered medium with normal medium property

It has been mentioned before that IOG indicates intrinsic property of ground structure. It is also the reason why we want to use the ratio of them to detect the lateral heterogeneity. Hence, it is indispensable to consider the influence of lateral heterogeneity on the ratio of IOG in the first place. In this article, we consider the simplest case of lateral heterogeneity: unidirectional inclined 2-layered medium, namely, 2D base model. We use FDM to simulate this model [67].

Before doing that, we examine the availability of the code base on FDM by carrying out a small test as shown in Fig. 3.6. The simplest 2-layered medium with no lateral heterogeneity is simulated using $200 \times 200 \times 50$ meshes with mesh size of $320m \times 320m \times 320m$

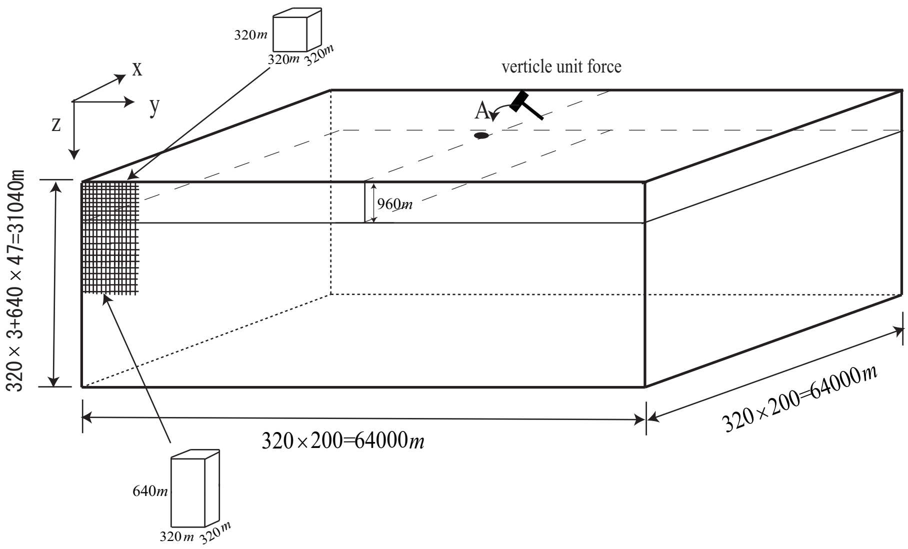


**Figure–3.6** The profile of the simple horizontally 2-layered medium for testing the validity of the code based on FDM. A unit force is exerted on site A to satisfy the definition of Green's function.

in the first layer and $320m \times 320m \times 640m$ in the second layer. In order to demonstrate the layered velocity structure, nonuniform grids are used as shown in Fig. 3.6. Besides, nonreflecting boundary condition is used to avoid the reflecting wave, in which 20 meshes wide at boundary [69]. Quite large size of mesh size is used here in order to simulate as large area as possible to mitigate the effect of reflecting of long-wavelength wave. The time interval is set to be $0.008s$ and the cutoff frequency is $0.25Hz$ and the higher frequency part is cutted off [70]. The duration for simulation is 130 seconds. The parameters of medium are shown in Table 3.1. Site A is located at the center of surface as the test site. A vertical unit force is exerted on A so the response at A should be equivalent to $G_{zz}(X_A, X_A)$ according to the definiton of Green's function. Their imaginary parts match well with each other when $f > 0.09Hz$ as shown in Fig. 3.7. The red curve shows the numerical IOG and the green one shows the one from numerical simulation using FDM. This lower cut-frequency is considered to be steming from the long-wavelengh resolution limit of FDM because the mesh size and mesh number is limited thus having bad reflection effect. Hence, we can say this proves the availability of this code based on FDM.

Next, we will use this code to simulate the unidirectionally inclined 2-layered medium. The profile is shown in Fig. 3.8. The related parameters are the same as shown in Table 3.1. As Fig. 3.8(a) shows, 8 sites, A to H, are located on the surface with even intervals

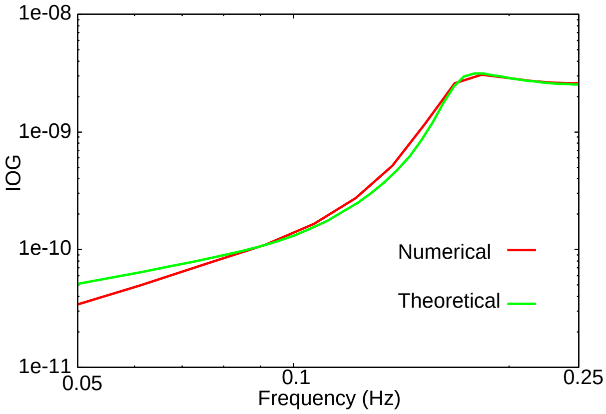


**Figure–3.7** Imaginary part of Green's function from numerical simulation and theoretical calculation. The red curve shows the numerical IOG and the green one shows the one from numerical simulation using FDM.

**Table–3.2** The first layer's thickness at each site

| Site name | A | B | C | D | E | F | G | H |
|---|---|---|---|---|---|---|---|---|
| Equivalent thickness (m) | 720 | 800 | 880 | 960 | 1040 | 1120 | 1200 | 1280 |

in the direction of inclination. One site by one site, a vertical unit force is exerted and the $G_{zz}(X_\chi, X_\chi)$, $\chi$=A to H is obtained. The first layer's thickness of each site is shown in Table 3.2. As described before, the mesh size is set to be quite large so that the inclination can only be simulated roughly. For example, the first layer's thickness under site H and G is actually the same as Fig. 3.8(b) shows. For convenience, we calculated the equivalent thickness of each site using the linear interpolation as shown in Fig. 3.8(b).

If it is horizontally layered medium, of course the ratios of IOG between any pair of sites are to be 1. In a complicated 3D medium, this ratio is expected to depend on the particular condition of lateral heterogeneity between two sites. In this simple case of unidirectionally inclined layered medium, the ratio should depend on the difference of first layer's thickness if one of the sites is fixed. In order to observe this, we take ratio of IOG between $\chi$ and $A$ which is $\frac{\Im[G_{zz}(X_\chi,X_\chi,\omega)]}{\Im[G_{zz}(X_A,X_A,\omega)]}$ in which $\chi$= B to H. The ratios are plotted in Fig. 3.9. The solid curves with different color show the ratio of IOG from H/A to B/A, repectively. Due to the resolution limit of the numerical simulation, there are some ratios with the same value: for example, $\frac{IOG(H)}{IOG(A)}$ and $\frac{IOG(G)}{IOG(A)}$. Despite this minor defect, it is observed that as the difference

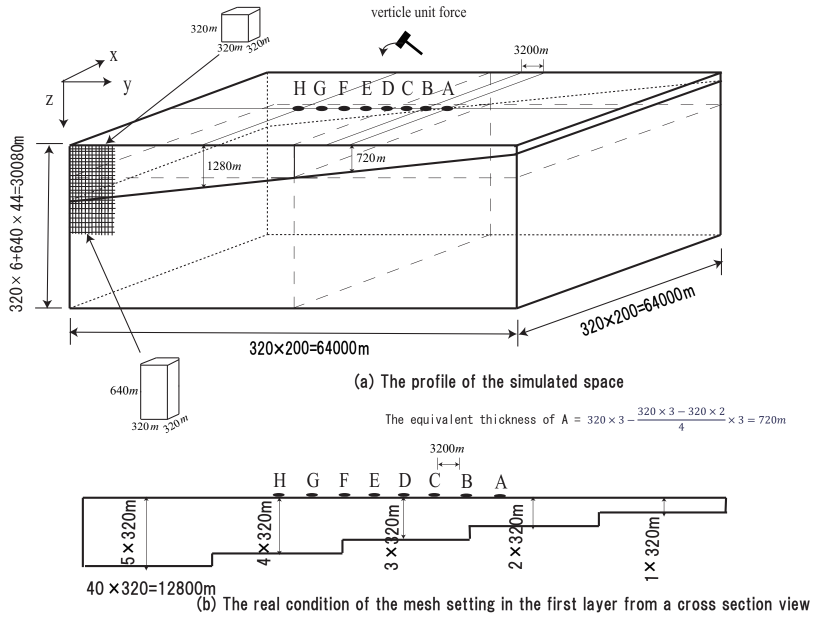


**Figure–3.8** The profile of the unidirectionally inclined 2-layered medium for calculating Green's function: (a) 8 sites of A to H in a line with different first layer's thickness (b) The cross section of the first layer: the stair shape of the mesh arrangement to roughly simulate the inclination; the mesh number and size at each stair

of first layer's thickness becomes larger, the peak frequency, the frequency where the ratio reaches maximum, shifts to smaller value and the amplitude shifts to larger value.

In a word, in a unidirectionally inclined 2-layered medium, there is a peak frequency in the ratio of IOG, which depends on the difference of first layer's thickness between two sites if one of the sites is fixed. This forms the theoretical base of making use of ratio of IOG to detect the lateral heterogeneity.

### 3.3.2 Sensitivity analysis for ratio of imaginary part of Green's function

In this subsection, we all discuss more comprehensively about the influence of the lateral heterogeneity on IOG using more samples of models. Moreover, the thickness of each layer is used as the main indicator showing the difference of ground structure at two different sites. If this difference can be identified using the ratio in Eq.3.12, the estimation of ground structure will be improved as Fig.3.4 shows. Hence, it is required to examine the sensitivity

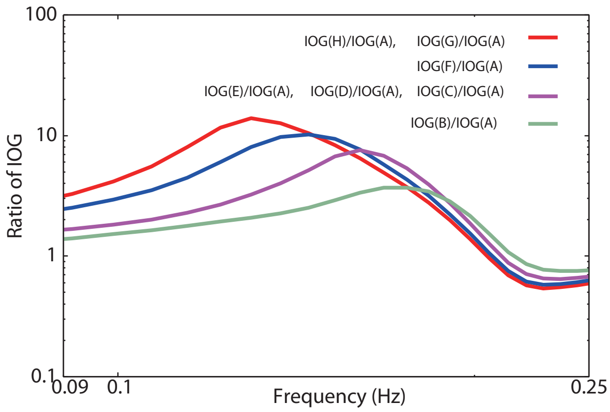


**Figure–3.9** Ratios of IOG between site $\chi$ and A, $\chi$ indicates B to H: the peak frequency shifts to smaller value as $\chi$ moves from B to H; some ratios overlap due to the limited resolution of numerical simulation which uses relatively large mesh size.

of ratio of imaginary part of Green's function with respect to the difference of thickness.

For simplicity, to confirm it, the right hand side of Eq.3.12 is calculated theoretically using the method proposed by Hisada [63, 64] for a simple model of ground structure on the basis of the model used in section 3.1. In Hisada's program, we set the delta time to be 0.07s, number of time to be 512 and the maximum frequency to be 5Hz.

We calculate 6 groups of data as shown in Table 3.3. For each group, the ratio of imaginary part of Green's function between Model i, that i=2,3,4,5,6,7 and Model 1 is calculated in the frequency domain. For example, in Group 1, the thickness of the first layer for Model1 until Model7 is 40,41,42,45,50,55,60 respectively. We calculate out the Green's function of them one by one and take the ratio of that of 41 and 40, 42 and 40, 44 and 40 until 60 and 40. Hence 6 ratios are obtained for each group to see the variation of ratio with the difference of thickness. For Group 1,2 and 3, the difference of thickness among models is the same but the starting thickness 40m, 80m and 120m are different so that the dependance of ratio on the thickness itself can be seen. The group 4,5,6 are under total different model but the setting of thickness is the same as group 1,2,3 so that we can see the variance of the ratio with respect to the property of ground structure. Fig.3.10 shows the ratio of imaginary part of Green's function in frequency domain from group 1 to group 6. The horizontal axis indicates frequency. The vertical axis indicates the ratio of IOG calculated using Hisada's program. Figures (a) to (f) show the result for group 1 to 6, respectively. The curves with colour from red to yellow indicate ratio of IOG

Model2/Model1 to Model7/Model1, respectively.

**Table–3.3** Two-layered models of ground structure

| Group | Layer | P-wave velocity [m/s] | S-wave velocity [m/s] | Density [t/m$^3$] | Thickness [m] Models | | | | | | |
|---|---|---|---|---|---|---|---|---|---|---|---|
| | | | | | 1 | 2 | 3 | 4 | 5 | 6 | 7 |
| 1 | 1 | 400 | 70 | 1.2 | 40 | 41 | 42 | 45 | 50 | 55 | 60 |
| | 2 | 2000 | 1000 | 2.5 | $\infty$ | | | | | | |
| 2 | 1 | 400 | 70 | 1.2 | 80 | 81 | 82 | 85 | 90 | 95 | 100 |
| | 2 | 2000 | 1000 | 2.5 | $\infty$ | | | | | | |
| 3 | 1 | 400 | 70 | 1.2 | 120 | 121 | 122 | 125 | 130 | 135 | 140 |
| | 2 | 2000 | 1000 | 2.5 | $\infty$ | | | | | | |
| 4 | 1 | 800 | 400 | 1.5 | 40 | 41 | 42 | 45 | 50 | 55 | 60 |
| | 2 | 1800 | 1200 | 2.0 | $\infty$ | | | | | | |
| 5 | 1 | 800 | 400 | 1.5 | 80 | 81 | 82 | 85 | 90 | 95 | 100 |
| | 2 | 1800 | 1200 | 2.0 | $\infty$ | | | | | | |
| 6 | 1 | 800 | 400 | 1.5 | 120 | 121 | 122 | 125 | 130 | 135 | 140 |
| | 2 | 1800 | 1200 | 2.0 | $\infty$ | | | | | | |

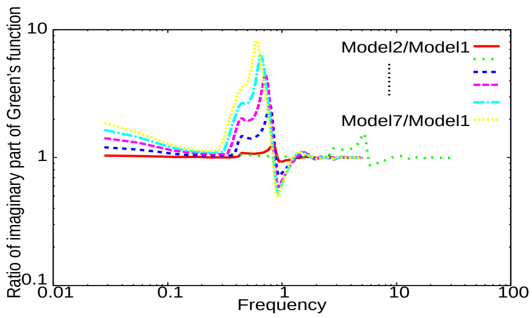


(a) Group1

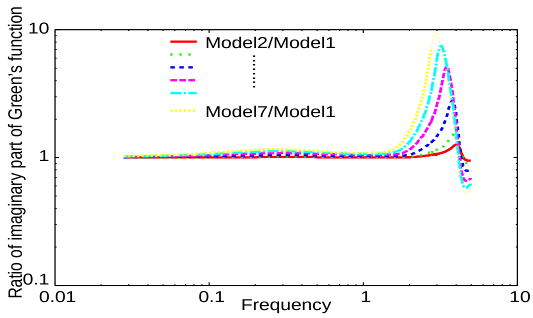


(b) Group4

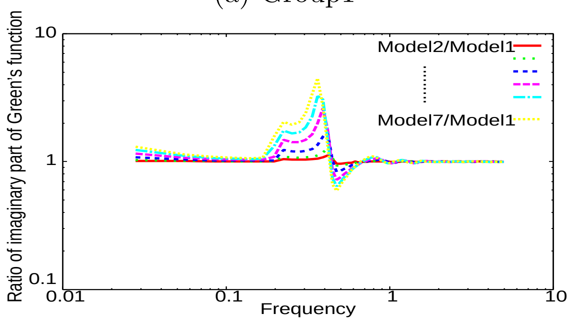


(c) Group2

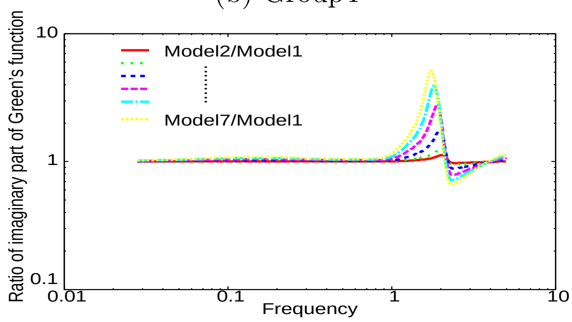


(d) Group5

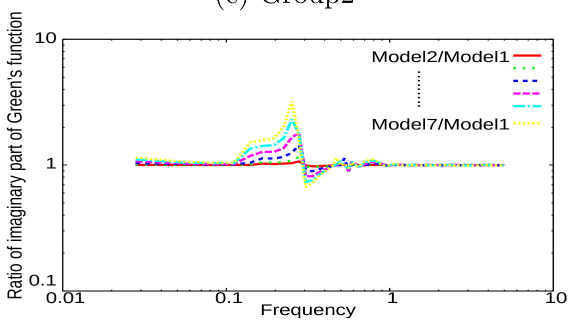


(e) Group3

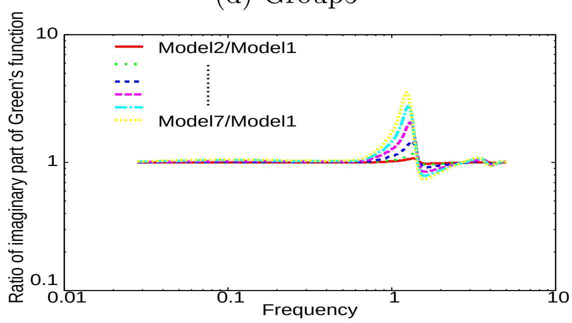


(f) Group6

**Figure–3.10** The ratio of imaginary part of Green's function between Model 2-7 and Model1. The horizontal axis indicates frequency. The vertical axis indicates the ratio of IOG calculated using Hisada's program. Figures (a) to (f) show the result for group 1 to 6, respectively. The curves with colour from red to yellow indicate ratio of IOG Model2/Model1 to Model7/Model1, respectively.

There are totally 6 groups of data. In order to analyze the ratio variation with the thickness more particularly, we take the difference of thickness as one variable $\Delta D$ and the frequency which gives the peak value as the function of the variable $f_p$. Hence, for six groups of data, we can draw six curves in one figure as shown in Fig.3.11. The horizontal axis indicates the difference of thickness and the vertical axis shows the peak frequency. Curves with different colour from red to yellow show the $\Delta D - f_p$ relationship in group 1 to 6, respectively

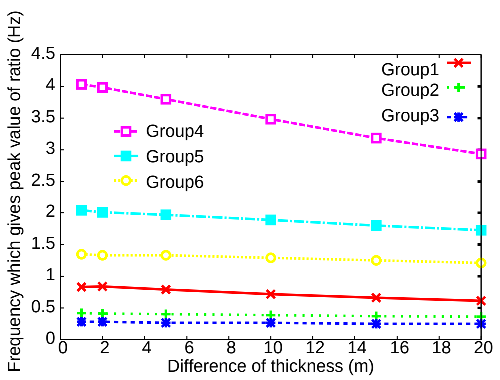


**Figure–3.11** Comparison of six groups of data about the $\Delta D - f_p$ relationship. The horizontal axis indicates the difference of thickness and the vertical axis shows the peak frequency. Curves with different colour from red to yellow show the $\Delta D - f_p$ relationship in group 1 to 6, respectively

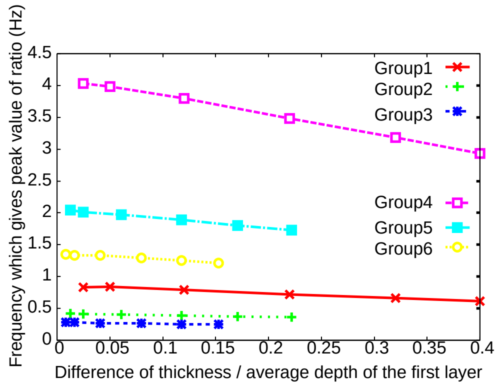


**Figure–3.12** Comparison of six groups of data about the $\frac{\Delta D}{\overline{D}} - f_p$ relationship. The horizontal axis indicates the difference of thickness and the vertical axis shows the peak frequency. Curves with different colour from red to yellow show the $\frac{\Delta D}{\overline{D}} - f_p$ relationship in group 1 to 6, respectively

For each curve of Fig.3.11, the $f_p$ decreases with the $\Delta D$ increasing. Hence, for a normal observation of equilateral-triangle array, the thickness difference between each pair of sites can be duduced by comparing the $f_p$. Comparing among group 1,2,3 or group 4,5,6, it is found that the deeper the second layer is, the smaller the slope will be. It means the sensitivity of ratio with respect to the difference of thickness becomes lower with the depth of the second layer increasing. Hence the new method proposed in this article is more useful to calculate shallow ground structure. Another conclusion is that with the depth of second layer increasing, the ratio becomes smaller. Comparing group 1,2,3 with group 4,5,6, the magnitude of ratio and the $f_p$ depends on factors including the S-wave velocity, P-wave velocity, the average of the layer's thickness of two sites and the differnce of the thickness between two sites.

To conform whether there is any relationship between $f_p$ and $\frac{\Delta D}{\overline{D}}$ in which $\overline{D}$ is defined as the average thickness of 2 models:

$$\overline{D} = \frac{D_{Model1} + D_{Modelj}}{2}(j = 2, 3, 4, 5, 6, 7) \tag{3.23}$$

Another figure is drawn as Fig.3.12 shows. It is almost the same as Fig.3.11. Hence, the

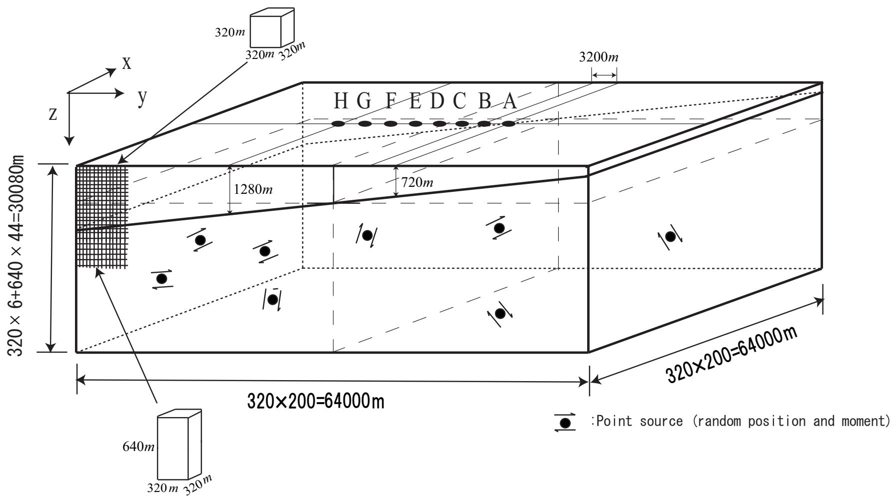


**Figure–3.13** The profile of the unidirectionally inclined 2-layered medium for simulating a diffuse wavefield: the 8 sites in a line is the same as in the last simulation; point sources of shear dislocation type are produced at random time and with random direction and magnitude to create a diffuse wavefield

ratio is not simply dependant on $\frac{\Delta D}{D}$.

Anyway, the ratio of imaginary part of Green's function depends on many elements. It is hard to estimate properties of ground structure once from the ratio. However, after obtaining a rough structure by SPAC method which means the S-wave velocity, P-wave velocity and average thickness are known, it becomes easy to estimate more details like $\Delta D$ according to the $\Delta D - f_p$ relationships.

## 3.4 A numerical simulation

In this chapter, the same FDM code is used to create a diffuse wavefield in the same model as above as shown in Fig. 3.13. In this wavefield, the validity of Eq. 3.12 will be examined among the observation sites.

### 3.4.1 Observation sites

The observation sites A to H are set in a line, which is the same as the previous section. The concept of vertical component spectral ratio is not limited to any array shape but

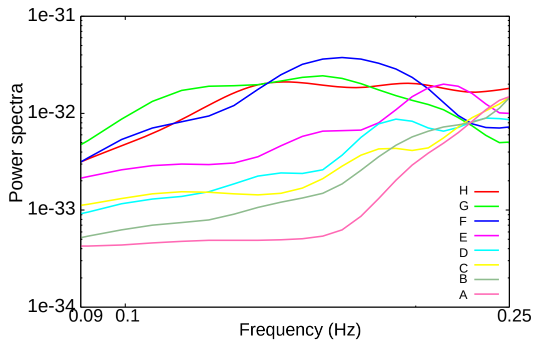


**Figure–3.14** Power spectra of vertical component at site A to H. Curves with different colors show the power spectra at different sites.

available at any any pair of sites. Even though the sites are arranged in a line just for simplicity, the simulation does not lose generality for any array methods.

### 3.4.2 To create a diffuse wavefield

In order to create a diffuse wavefield, we refer to the noise synthetics generation measure in the article by Cornou et al. [71]. Point sources of shear dislocation type with random strike, dip, rake angles and seismic moment are exerted on mesh at random position of $(x, y, z)$, where x, y and z are mesh number in three directions, using stress approach [72]. The number of sources is about 1250 per 10 seconds.

### 3.4.3 Examination on the new perspective of vertical component ratio of power spectra

Next, we observe the behaviour of the vertical component ratio of power spectra to see whether it coincides with that of ratio of imaginary part of Green's function. For simplicity, we take ratios between $\chi$ and $A$, $\chi$=B to H, in which $A$ works as a reference site, which is similar with the former section and the other 7 sites are with different first layer's thickness. Power spectra for each site is calculated as shown in Fig. 3.14 and the ratios are obtained quickly. The theoretical ratios of IOG, respectively, are calculated, using the same technique as in the previous section, from synthetic waveforms obtained by a 3D numerical simulation with a same observation direction as a dip direction. The result

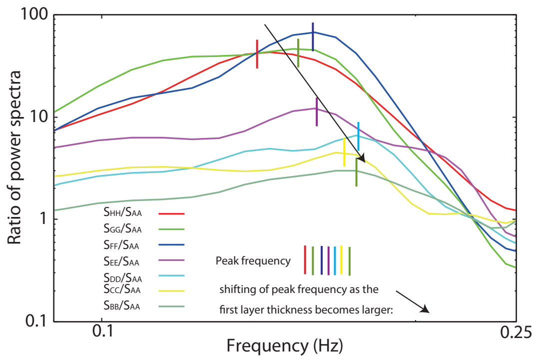


**Figure–3.15** Ratio of power spectra of vertical component between site $\chi$ and A, $\chi$ indicates B to H: the peak frequency is marked by vertical line; the black arrow indicates the shifting of peak frequency as $\chi$ moves from H to B

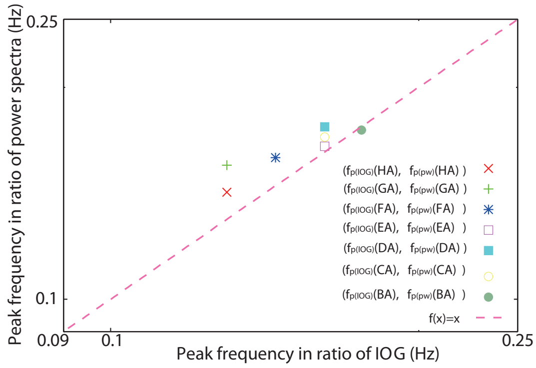


**Figure–3.16** The consistency check of the peak frequency from two kinds of ratios: the $f_{p(IOG)}$ indicates the peak frequency in the ratio of IOG and the $f_{p(pw)}$ indicates the peak frequency in the ratio of power spectra; different symbol indicates this comparison between different pair of sites; the $f(x) = x$ line helps to see the status of consistency clearly

is shown in Fig. 3.15. The solid lines indicate the ratios of power spectra while different colours indicate different pairs of sites. the peak frequency is marked by vertical line; the black arrow indicates the shifting of peak frequency as $\chi$ moves from H to B. Compared with the ratios in Fig. 3.9, it is observed that the amplitude do not match. Moreover, there is the large fluctuation of the amplitude in Fig. 3.15 among ratios. This comes from the fluctuation of power spectra at each site as shown in Fig. 3.14. Firstly, The different amplification factor at different site (they have different first layer's thickness) is considered to be partly the cause. The limited accuracy of numerical simulation is the second cause. Then, we analyze the consistency of the peak frequency from two kinds of ratios between each pair of sites in Fig. 3.16. The $f_{p(IOG)}$ indicates the peak frequency in the ratio of IOG and the $f_{p(pw)}$ indicates the peak frequency in the ratio of power spectra. Different symbol indicates this comparison between different pair of sites; the $f(x) = x$ line helps to see the status of consistency clearly. It is observed that they match quite well. There exist some discrepancy between the peak frequency from two kind of ratios. Firstly, this may be caused by the resolution limit of the numerical simulation due to the too big mesh size relative to the site intervals. Secondly, the wavefield is of course not perfectly a diffuse wavefield, which would have bad influence on the result. The setting of source type and source number remain a future work. Neglecting this, it is more meaningful to observe that the peak frequency of ratio decreases as the $\chi$ becomes farther from $A$ as shown in Fig. 3.15. This tendency coincides with that in Fig. 3.9. In a word, this result proves the availability of Eq. 3.12 in this simulated wavefield.

Combining Fig. 3.14, Fig. 3.15, and Fig. 3.16, it is observed that by taking vertical component ratio of power spectra between two sites, a peak frequency can be obtained which actually comes from the ratio of IOG between two sites. As for this unidirectionally inclined 2-layered medium, the peak frequency changes as the difference of first layer's thickness changes if one of the sites is fixed. These suggest that by applying the vertical component ratio of power spectra between two sites, it is possible to detect and even estimate the lateral heterogeneity, in this case the inclinaton, in the arrays' area using certain inversion techniques of theoretical Green's function.

### 3.4.4 Discussion

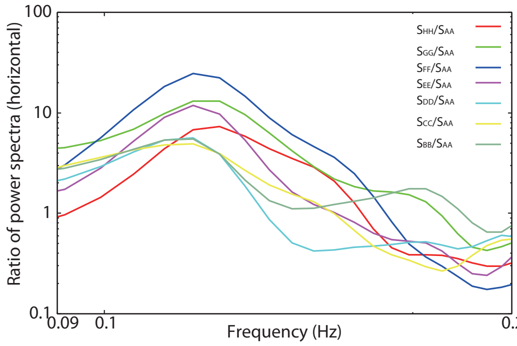


(a) The ratios of power spectra (horizontal component) among sites

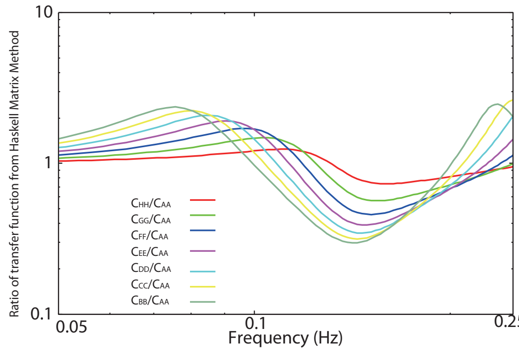


(b) The ratios of transfer function from Haskell Matrix Method among sites

**Figure–3.17** Ratio about horizontal component between site $\chi$ and A ($\chi$ indicates B to H): (a) ratio of power spectra of horizontal component: the peak frequency almost does not shift as $\chi$ moves from H to B (b) ratio of transfer function from Haskell Matrix Method: $C_{\chi\chi}$ indicates the transfer function at site $\chi$; peak frequency shifts quickly as $\chi$ moves from H to B

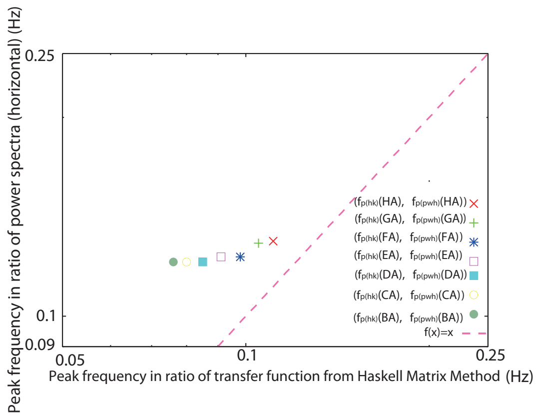


**Figure–3.18** The consistency check of the peak frequency from two kinds of ratios: the $f_{p(hv)}$ indicates the peak frequency in the ratio of transfer function from Haskell Matrix Method and the $f_{p(pwh)}$ indicates the peak frequency in the horizontal component ratio of power spectra; different symbol indicates this comparison between different pair of sites; the $f(x) = x$ line helps to see the status of consistency clearly

The availability and the potential of the vertical component spectral ratio between two sites have been demonstrated above. However, as mentioned in the section of introduction, the idea of taking spectral ratio between two sites is not new. The significance of the proposed perspective may be underestimated. Hence, some typical and old concepts about the spectral ratios between 2 sites would be reviewed. Then, we examine their availability to detect the lateral heterogeneity in the 2D model in the simulated diffuse wavefield.

By taking the horizontal spectral ratio between one site and the reference site, the S-wave resonance frequency can be obtained if the motion at the reference site is representative of the excitaion arriving at the interface of soil layer and base [66]. It is clear that this concept can not be applied to interpret the ratios between 2 sites in our numerical simulation, because both sites are on the same surface. On the other hand, in Kanai's theory [65], the ideal 1D base model is assumed for each site, namely, horizontally layered medium and the horizontal component Fourier amplitude itself is representative of the transfer function of SH wave. Even this concept is based on 1D model and simply vertically S-wave wavefield, it may be doubted that the spectral ratio based on Kanai's theory is enough to detect the lateral heterogeneity in 2D model and full-wave wavefield. Therefore, although Kanai did not apply this idea to the ratio between two sites, we would like to carry this classic concept out for confirmation. Accordingly, the peak frequency obtained from horizontal component ratio of power spectra between two sites is equivalent to the ratio of SH wave transfer function between two sites. In order to examine whether this concept works in this numerical simulation, we calculate the transfer function of SH wave using Haskell Matrix Method for each site and take the ratios between the same 7 pairs of sites as in previous subsection. The comparison with the horizontal component ratio of power spectra is shown in Fig. 3.17. Fig. 3.17 (a) shows the ratio of power spectra of horizontal component and Fig. 3.17 (b) shows the ratio of transfer function from Haskell Matrix Method. $C_{\chi\chi}$ indicates the transfer function from Haskell Matrix Method at site $\chi$ ($\chi$ is A to H). The peak frequency from two kinds of ratios are compared in Fig. 3.18. The $f_{p(hv)}$ indicates the peak frequency in the ratio of transfer function from Haskell Matrix Method and the $f_{p(pwh)}$ indicates the peak frequency in the horizontal component ratio of power spectra. It is obvious that the two ratios deviate from each other very much.

This result suggests that in this numerical simulation, the horizontal component ratio of power spectra between two sites can not be explained by simply the ratio of transfer function obtained from 1D base model well. It is bacause in Kanai's theory, the 2D base model and the condition of full wave are not taken into consideration. Here we do not mean to prove the unavailability of the conventional method. However, it is meaningful to say that in a complicated base model, it is better to use the Green's function theory based on the assumption of full wave to explain the ratio of power spectra between two sites. In

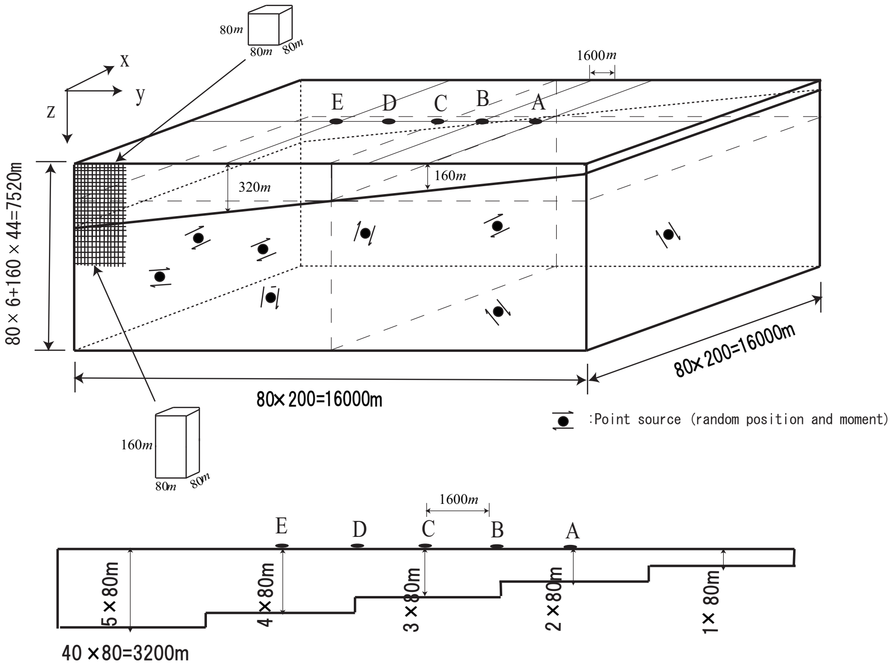


**Figure–3.19** The profile of the unidirectionally inclined 2-layered medium for simulating a diffuse wavefield: the 5 sites in a line are shown by black dots; point sources of shear dislocation type are produced at random time and with random direction and magnitude to create a diffuse wavefield; The depth of first layer under each site is also shown in the section profile in the lower half

this article, the vertical component ratio of power spectra between two sites in a 2D base model is successfully interpreted using the IOG.

Moreover, $f_{p(pwh)}(\chi A)$ almost does not change as the site $\chi$ moves from $H$ to $B$. This means $f_{p(pwh)}$ has no sensitivity to the lateral heterogeneity. Hence, it is difficult to use it to estimate ground structure. However, this is not the point of this article, which remains to be discussed in the future.

### A second example using numerical simulation

We showed one numerical example above to demonstrate the availability of the ratio of power spectra among sites in the created diffuse wavefield. For a more comprehensive confirmation, here we carry out one more numerical simulation which is almost the same as the previous one except for the depth of first layer as Fig. 3.19 shows. And for simplicity, we only choose 5 sites on the surface as the observation sites. In order to realize the smaller size of mesh. We coordinated the parameters in Sakai's program of FDM. As a result, the

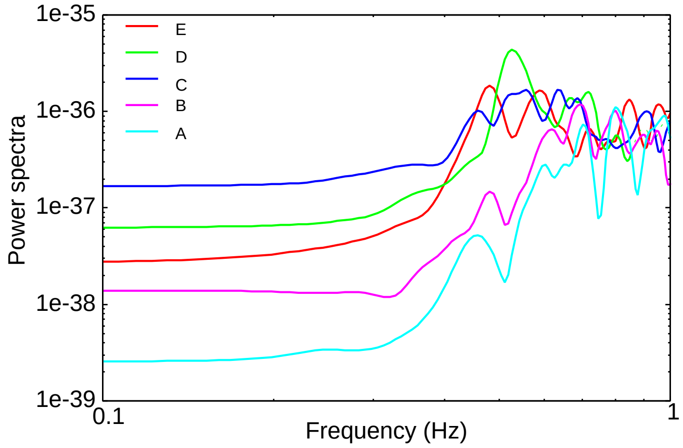


**Figure–3.20** Power spectra of vertical component at site A to E

**Table–3.4** The first layer's thickness at each site

| Site name | A | B | C | D | E |
|---|---|---|---|---|---|
| Equivalent thickness (m) | 160 | 200 | 240 | 280 | 320 |

time interval is set to be 0.004$s$ and the cutoff frequency is 1.00Hz. We calculated the ratio of IOG and power spectra between site $\chi$ and $A$, $\chi$=B to E, respectively. The first layer's thickness at each site is shown in Table 3.4. The power spectra itself at each site is shown in Fig. 3.20. And the estimations are shown in Fig. 3.21 and Fig. 3.22. Similarly as the previous example, the peak frequency of each pair sites match with the ratios of IOG very well as shown in Fig. 3.21 and Fig. 3.22. Although there is some deviations at ratio of CA and DA, it is acceptable considering the limit of resolution of FDM. Do not forget the depth at C and D is calculated using the concept of "equivalent depth" and interpolation method. Anyway, we do this example just to make the conclusion we will draw in this chapter more convincing.

## 3.5 Summary

Using seismic interferometry theory, we propose a new perspective of the vertical component ratio of power spectra between 2 sites in diffuse wavefield. Through theoretical analysis and numerical simulation, there are several conclusions to be drawn.

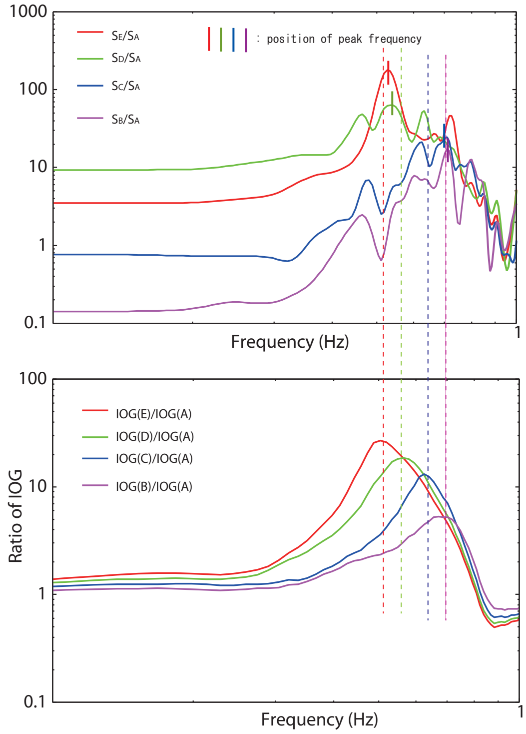


**Figure–3.21** Ratio of power spectra of vertical component between site $\chi$ and A ($\chi$ indicates B to E): the peak frequency is marked by vertical line

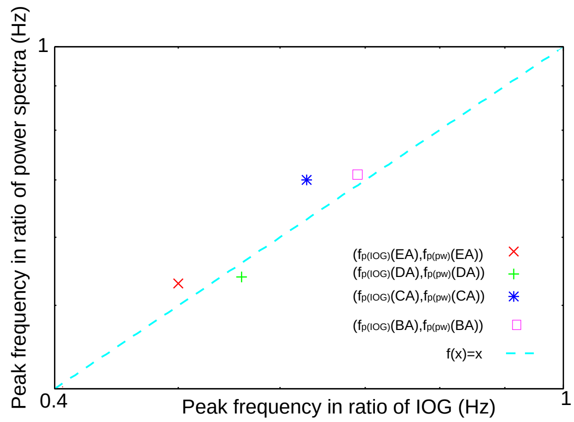


**Figure–3.22** The consistency check of the peak frequency from two kinds of ratios: the $f_{p(IOG)}$ indicates the peak frequency in the ratio of IOG and the $f_{p(pw)}$ indicates the peak frequency in the ratio of power spectra; different symbol indicates this comparison between different pair of sites; the $f(x) = x$ line helps to see the status of consistency clearly

(1) There exists a peak frequency in the vertical component ratio of power spectra between two sites. It depends on the particular condition of lateral heterogeneity between 2 sites.

(2) In a simple unidirectionally inclined 2-layered medium in diffuse wavefield, the peak frequency depends simply on the difference of first layer's thickness and the average thickness of first layer. As for a ratio $\frac{S_{xx}}{S_{aa}}$, where first thickness of site $x$ bigger than that of site $a$, with the site $a$ fixed, the peak frequency decreases as the site $x$ becomes farther.

(3) In an inclined 2-layered medium, by taking the vertical component ratios of power spectra among sites at arrays, the peak frequency can be a good indicator of lateral heterogeneity by applying the equivalence with that from the ratio of IOG.

(4) In this numerical simulation, it does not work well to interpret the horizontal component ratio of power spectra using the ratio of transfer function of SH wave. Hence, it proves that in the condition of full wave and in complicated base model, it is better to use Green's function theory to interpret the spectral ratio between 2 sites.

(5) This chapter demonstrates a new interpretation of the vertical component ratio of power spectra and proves its potential of detecting lateral heterogeneity in a simple numerical simulation using the peak frequency. It remains as a future work to develop the inversion technique to estimate the particular condition of lateral heterogeneity from the peak frequency among sites in a 2D base model or more complicated model.

# 4

# Range estimation using a simple linear array for 2D layered medium

## 4.1 Introduction

In this chapter, we will combine the results obtained from the chapter 2 and chapter 3 to constitute a comprehensive methodology which has good significance in the estimation of 2-D ground structure. The content in chapter 2 and chapter 3 seems having no relashipship. Hence, we will firstly make a summary of them two and point out the potential of applying them two to a more magnificent objective. Afterward, we would create a framework of the new methodology or technique and solve the problems. Finally, the availability would be confirmed using numerical simulation.

## 4.2 A summary and extension of the chapter 2 and 3

For chapter 2, we described the necessity of developing a method for microtremor survey with a convenient/easy conducting array shape and proposed a method, whose availability has been confirmed by numerical simulation and field tests. By using a 3-site linear array with proper intervals in the diffuse wavefield, it is able to estimate the phase velocity of Rayleigh wave in the $kr_{max}$ range of 1.3 to 2.8 with very good stability and accuracy. This method is born from the original SPAC method. Its available range in frequency range is limited while it is much easier to conduct in real cases.

For chapter 3, we described the insufficiency of the microtremor related method in dealing with 2D ground structure. Then, we proposed a new perspective about the vertical component spectral ratio between two sites using SI. It is very convenient tool because only vertical components need to be obtained. Moreover, the equivalence with the ratio of IOG and the wide applicable range of SI itself made it possible to detect more about the complexity of the ground structure. We demonstrated by numerical simulation that this ratio is significant in detecting the lateral heterogeneity in a simple 2D ground strucure. And by applying the property of this ratio , which is the peak frequency, there is great potential to make an inversion technique to identify the simple lateral heterogeneity and do a more comprehensive estimation of ground structure.

For vertical component spectral ratio, there is not any requirement about the positions of the pair of sites. It is mentioned that the concept can be applied to any array methods including SPAC method and so on. Hence, of course, it can be applied to the method proposed in chapter 2. Moreover, in chapter 3, we described the lateral heterogeneity using the simplest model of unidirectionally inclined 2 layered medium and the sites chosen are just on a line. It becomes very natural to use a linear array and at the same time applying the vertical component spectral ratio among them to detect the inclination. Although we just assumed the simplest case, it is significant as the starting of research about 2D model exploration using microtremor survey method. In the next part, we would still use the simplet assumption as in chapter 3: (1) 2D 2-layered model; (2) unidirectionally inclined; (3) a diffuse wavefield to constitute and confirm the new methodology.

## 4.3 The range estimation of 2D layered medium using one simple linear array

Here we already have a very rough image of how to combine these two concepts. Still, there is some trouble very obvious in this way. Firstly, the two methods, linear array and vertical component spectral ratio is based totally different assumptions. That is the former one assumes a horizontally layered medium while the latter one has a huge range of availability because it can be applied to any kind of inhomogeneous medium. Hence, it is questionalble whether we can make them “live together”. Secondly, it seems very beautiful to estimate lots of information of the 2D ground structure using just 3 sites on a line. Is is really practical? It must be shown particularly that in what kind of case, even under the very simple assumption of unidirectionally layered medium, it is available to make the beautiful dream true. Moreover, in cases that this concept cannot be realized, we will consider other potential in microtremor survey by combining these two concepts.

### 4.3.1 Discussion on the application of linear array method in a inclined layered medium

As we decribed before, we plan to use linear array method to make a rough, not necessarily very accurate, estimation about the ground structure. This rough estimation we would obtain can only be horizontally layered medium because the linear array method, born from SPAC method, is just based on this assumption. However, the strucure we want to know is the inclined layered medium. Because we still have a tool, the vertical component spectral ratio, to make more detailed estimation about the inclination/lateral heterogeneity, in the first stage, it is enough to just have a estimation with first layer's thickness close to the "average depth" of the first layer of the real inclined medium.

In order to confirm this, we have a numerical simulation first as shown by Fig. 4.1. The meth size is the same as in the chaper 3. The cut-off frequency is $1Hz$. The time interval is $0.004s$ and the observation duration is around 64 seconds. We, on purpose, set the inclination to be steep and see how the linear array behaves. The linear array has 4 sites in this case in order to constitute two 3-site linear arrays to cover more frequency range by linear array ABC and BCD. The dispersion curve is shown in Fig. 4.2. The blue curve and purple curve indicate the theoretical dispersion curve of horizontally layered medium with thickness of 320m and 224m, respectively. The red and green dots indicate the estimation from small and large linear array, ABC and BCD, respectively. As shown, we add the theoretical dispersion curve in assuming horizontally layered medium with different first layer's thickness at A and D. The two theoretical dispersion curves are calculated out to behave as the rough acceptable range of the estimated dispersion curve. Then from the results it can be observed that though it does not accurately match with any of the theoretical curves, it is even not among the acceptable range. But it is still close to the

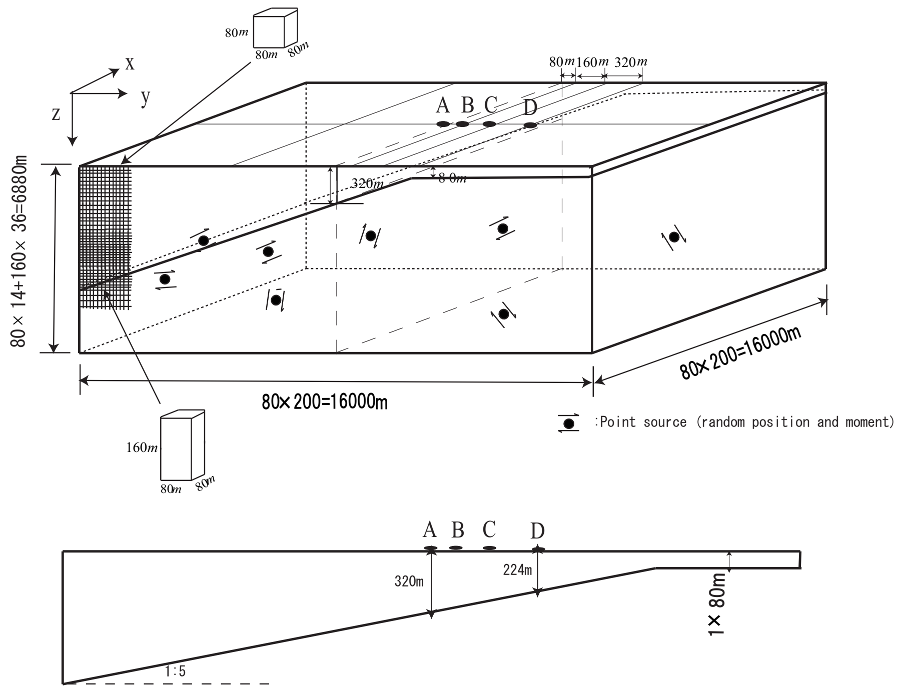


**Figure–4.1** The profile of the unidirectionally inclined 2-layered medium with a big inclination angle for simulating a diffuse wavefield: the 4 sites in a line is the linear array we use to estimate the dispersion curve of the ground structure; point sources of shear dislocation type are produced at random time and with random direction and magnitude to create a diffuse wavefield

320m curve. For we still have after processs by using the vertical component ratio. It can be still said that it satisfy the condition that the estimation can obtain a close and rough estimation about the first layer's depth. Hence, We can draw a conclusion that in a strongly inclined medium, it is available to use linear array method to have a rough estimation.

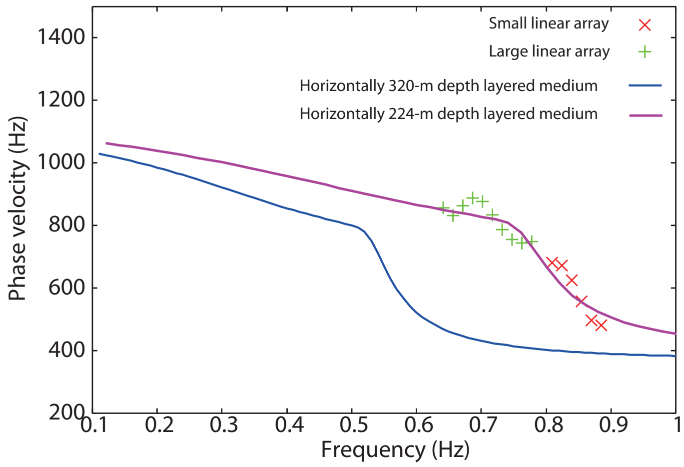


**Figure–4.2** The dispersion curve obtained using the linear array ABC compared with the dispersion curves theoretically obtained by using horizontally layered medium with different depth. The blue curve and purple curve indicate the theoretical dispersion curve of horizontally layered medium with thickness of 320m and 224m, respectively. The red and green dots indicate the estimation from small and large linear array, ABC and BCD, respectively.

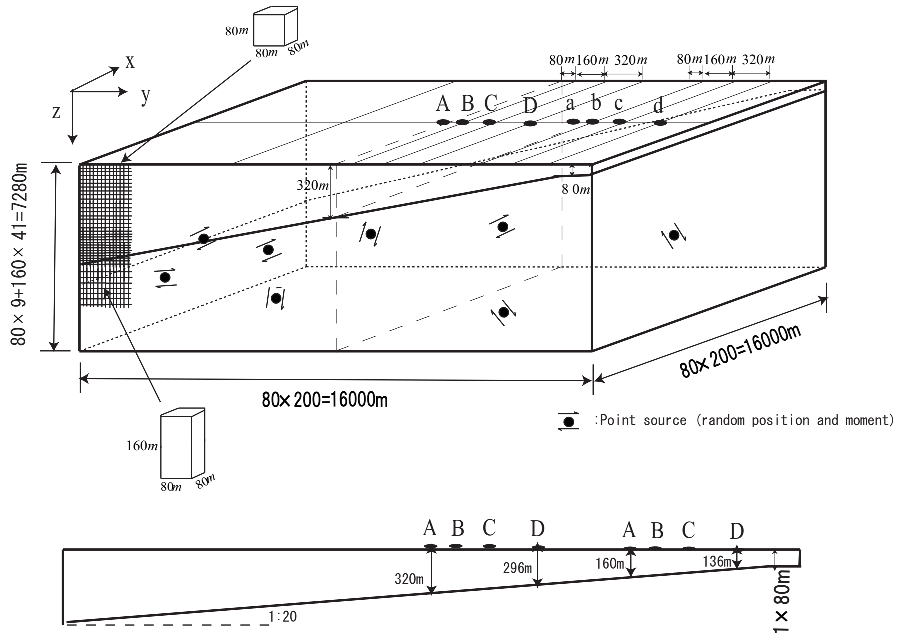


**Figure–4.3** The profile of the unidirectionally inclined 2-layered medium with a relatively slight inclination angle for simulating a diffuse wavefield: there are two sets of 4 sites in a line is the linear array we use to estimate the dispersion curve of the ground structure; point sources of shear dislocation type are produced at random time and with random direction and magnitude to create a diffuse wavefield

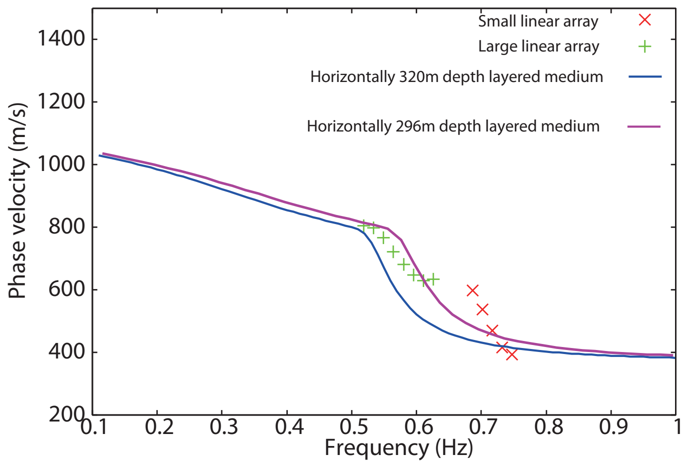


**Figure–4.4** The dispersion curve obtained using the linear array ABCD compared with the dispersion curves theoretically obtained by using horizontally layered medium with different depth. The blue curve and purple curve indicate the theoretical dispersion curve of horizontally layered medium with thickness of 320m and 296m, respectively. The red and green dots indicate the estimation from small and large linear array, ABC and BCD, respectively.

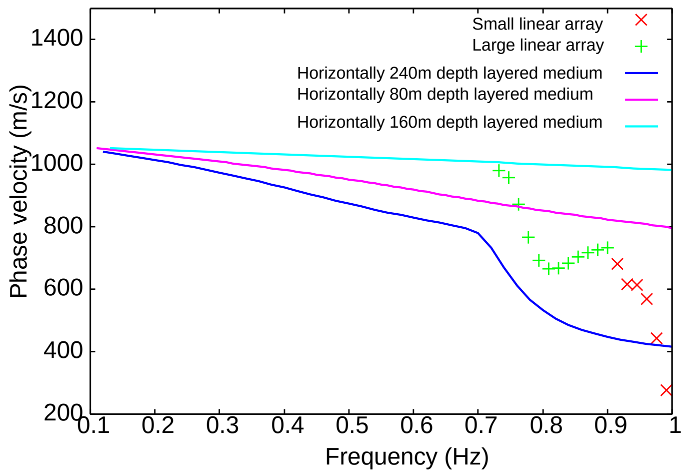


**Figure–4.5** The dispersion curve obtained using the linear array ABC compared with the dispersion curves theoretically obtained by using horizontally layered medium with different depth

To be more comprehensive, we have a second numerical simulation as shown by Fig. 4.3. We, on purpose, set the inclination to be slightly inclined and see how the linear array behaves. In this case, we set two linear arrays with a relatively long distance to see how they behave. The reason we will set two arrays will be explained later on. The dispersion curve is shown in Fig. 4.4 and Fig. 4.5, repectively. It can be observed that in the ABCD linear array result as shown in Fig. 4.4, though it is not accurately match with any of the theoretical curves, it is among them and close to the middel value one (320m). It satisfy the condition that the estimation can obtain a close and rough estimation about the first layer's depth very well. For another linear array abcd as shown in Fig. 4.5, confined by the resolution limit, namely, the cut frequency of FDM, it is quite bad curve. It may come from the complexity of the ground structure ifself or be spoiled by the resulution limit of the FDM. Though, the curve is among the close theoretical dispersion curves.

### 4.3.2 The constitution of the new methodology

On the basis of the results from the previous subsection, now it is time to propose the whole methodology now. For a steeply inclined medium, the small scale linear array, a 4-site linear array with small size, is capable to do the estimation. First, we use the proposed method in chapter 2 to have a initial rough estimation of the layered medium, for example, the first layer's thickness $z$. Then, we set a fluctuation range around $z$. For example, we set the range size to be $[-0.2z, 0.2z]$. Then we use some inversion technique to look for the optimal inclination angle and the average layer thickness. For example, for the initial try, we set $z - 0.1z$ at A and $z + 0.15z$ at D, and calculate the ratio of IOG given these parameters to compare with the ratio of power spectra obtained from observation. If it is larger than that, we may coordinate the thickness at A to be smaller like $z - 0.12z$. We keep trying and finally obtain the optimal 2D model structure. The process is shown in Fig. 4.6.

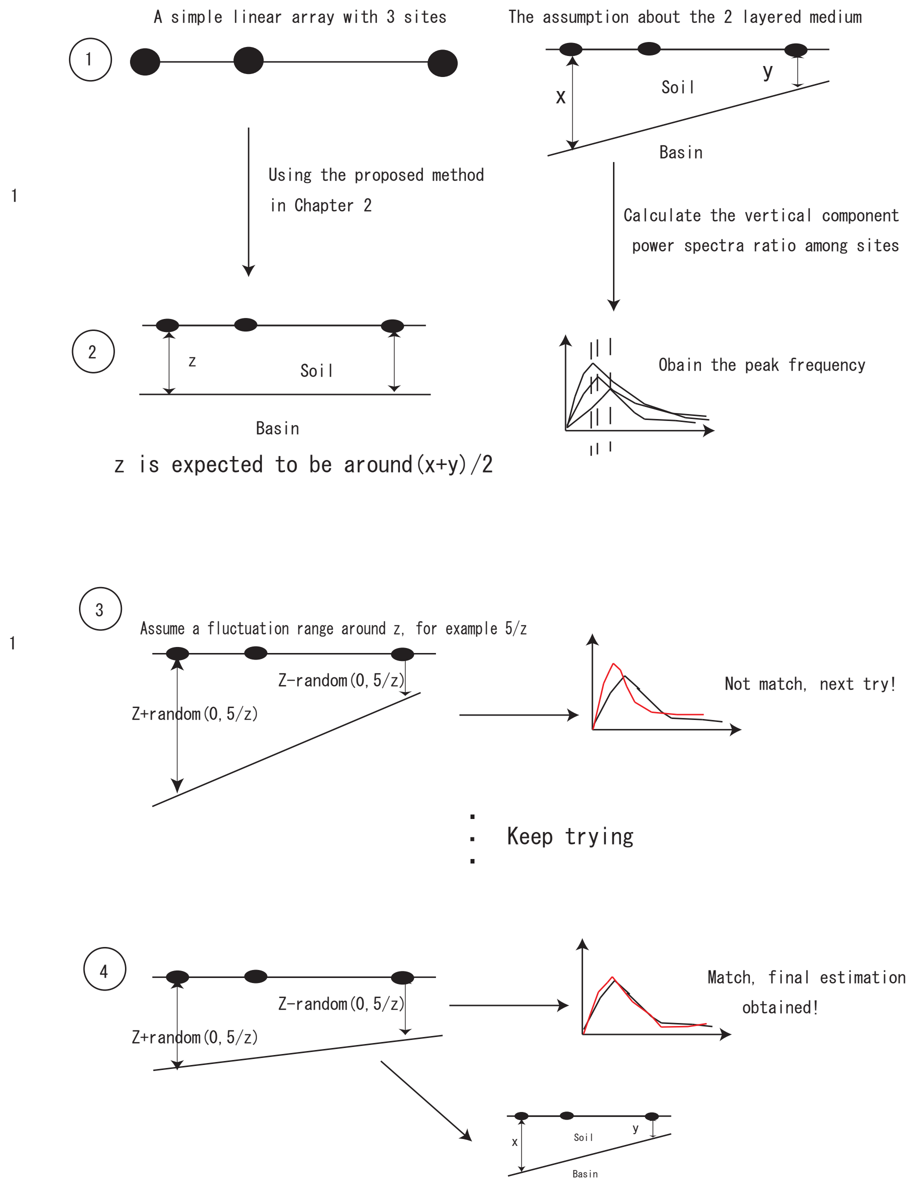


**Figure–4.6** The methodology constituted to estimate 2D model using 3-site/4-site linear array in a strongly inclination case

However, this process is still designed to be naive and rough. According to Figs. 3.10, 3.10, 3.11 and 3.12, it seems that according to the peak frequency and the amplitude, the inclination and the thickness of each site can be estimated accurately if the distance between the sites is fixed. However, it is too ideal because in the real cases, the amplitude is difficult to be used as an indicator because it may be influenced by the incoherent noise at each local site and other factors. Hence, the peak frequency $f_p$ becomes the only indicator. Under these limits, it is almost impossible to develop an inversion technique to estimate the exact 2D model because the number of unknowns, the inclination angle and the thickness, is larger than the known information, only the peak frequency as shown in Fig. 4.7.

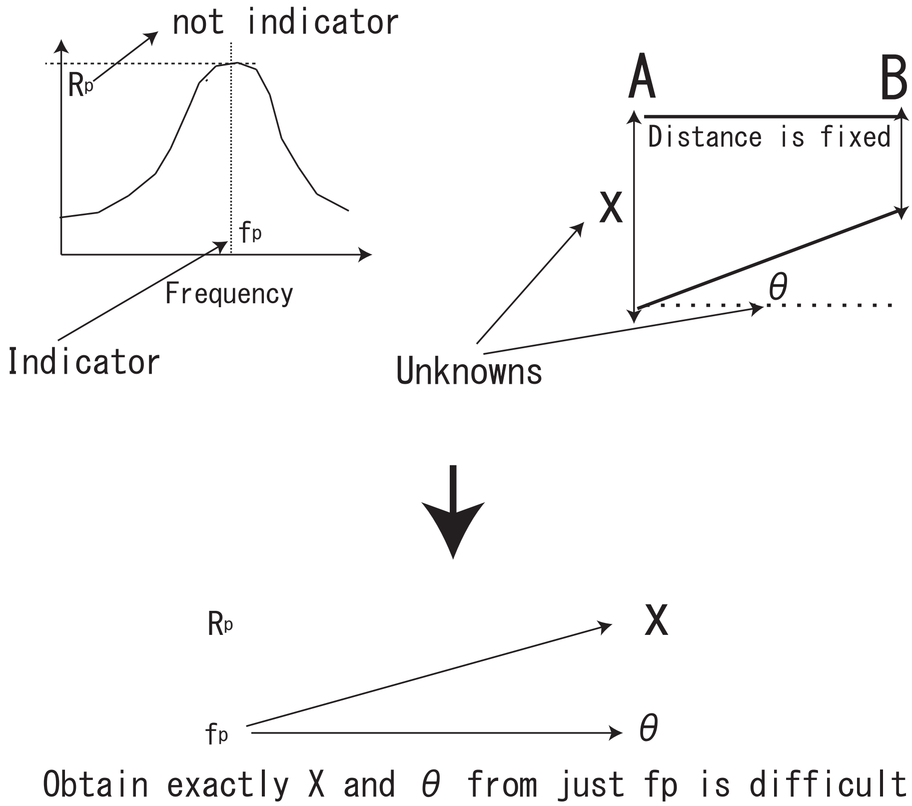


**Figure–4.7** A image showing that with only the help of peak frequency $f_p$, the exact 2D model is difficult to be inversed out.

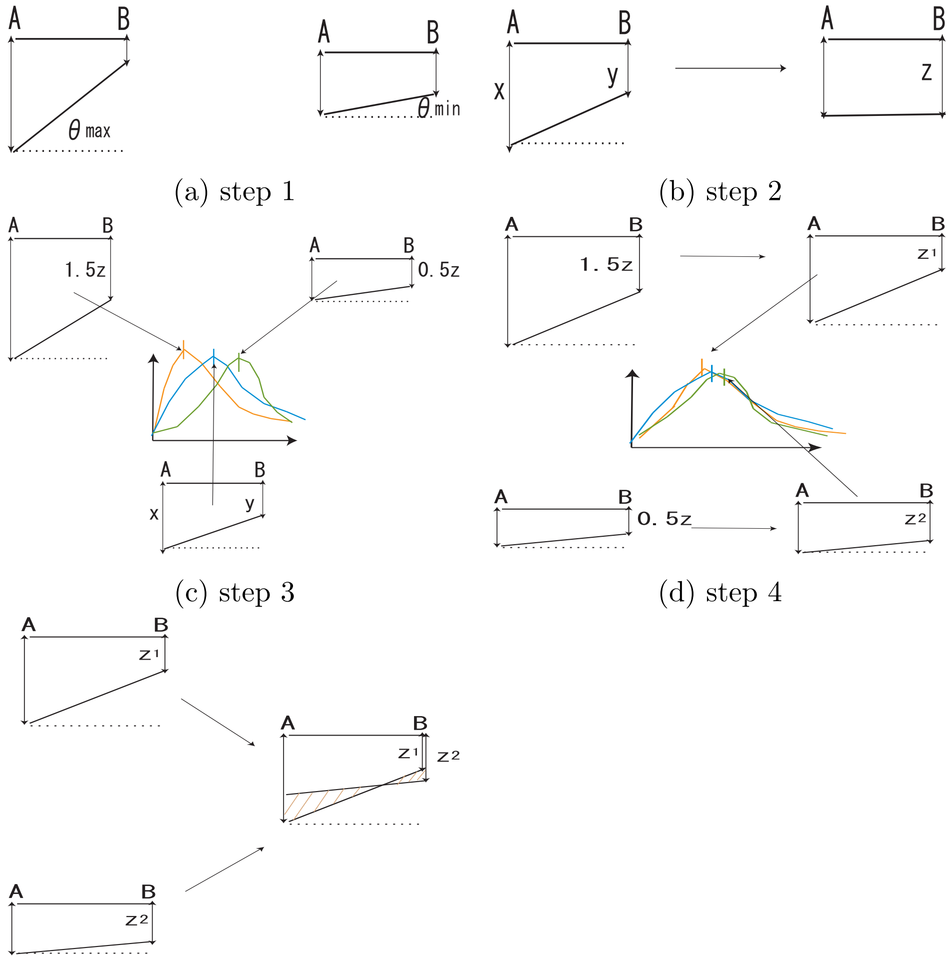


(a) step 1 (b) step 2

(c) step 3 (d) step 4

(e) step 5

**Figure–4.8** The steps of doing a range estimation using a linear array about a 2 layered 2D model: (a) set a maximum inclination angle $\theta_{max}$ and minimum inclination angle $\theta_{min}$; (b) use the linear array method to give a rough estimation of the layer's thickness $Z$; (c) use two models as the starting models with $\theta_{min}$ and $\theta_{max}$, respectively. For the model with $\theta_{min}$, we choose a relatively small value of thickness so that this model can produce an upper limit of peak frequency $f_p$ while for the model with $\theta_{max}$, we choose a relatively large value of thickness so that this model can produce a lower limit of peak frequency $f_p$. Now we list the peak frequency of the vertical spectral ratio between A and D calculated from the field data. It is expected that this ratio which shown by the blue vertical line should be between the lower limit of $f_p$ and upper limit which is shown by the orange vertical line and green vertical line, repectively so that it would be reasonable to do coordination using the two models as the starting ones; (d) coordinate the starting models by coordinating the corresponding thickness of each model to make the $f_p$, the orange vertical line and green vertical line shift to the position as close to blue vertical one as possible so that the coordinated model; (e) obtain the final range estimation

Hence, it is more realistic to do some range estimations about it, which means, we should control some parameters by ourselves. We choose the parameters to be the inclination angle of the layered medium, to be exact, the boundary of the layers. The step is shown in Fig. 4.8. At step 1, we set a maximum inclination angle $\theta_{max}$ and minimum inclination angle $\theta_{min}$ artificially. This has no theoretical backup and is just a tentative assumption. The objective is to calculate the layer's thickness under the assumption of $\theta$ so that we can have a range estimation, namely, a upper limit and a lower limit, finally as shown later. At step 2, we use the linear array method to give a rough estimation of the layer's thickness $Z$, whose applicability has been confirmed by the former subsection.

At step 3, we use two models as the starting models with $\theta_{min}$ and $\theta_{max}$, respectively. For the model with $\theta_{min}$, we choose a relatively small value of thickness so that this model can produce an upper limit of peak frequency $f_p$ while for the model with $\theta_{max}$, we choose a relatively large value of thickness so that this model can produce a lower limit of peak frequency $f_p$. Now we list the peak frequency of the vertical spectral ratio between A and D calculated from the field data. It is expected that this ratio which shown by the blue vertical line in Fig. 4.7 (c) should be between the lower limit of $f_p$ and upper limit which is shown by the orange vertical line and green vertical line, repectively, as shown in Fig. 4.7 (c) so that it would be reasonable to do coordination using the two models as the upper and lower bounds. If the blue line is left to orange one or right to green one, it is necessary to change the starting model, $\theta_{min}$, $\theta_{max}$ or the initial thickness of two models. Under the condition that we believe that the depth of starting model should be near the rough estimation at step 2, it is more reasonable to change $\theta_{max}$ or $\theta_{min}$.

At step 4, we coordinate the starting models by coordinating the corresponding thickness of each model to make the $f_p$, the orange vertical line and green vertical line shift to the position as close to blue vertical one as possible so that the coordinated models, as shown by the two models in the lower half in Fig. 4.8 (d), can be seen as two possible estimations of the 2 layered 2D models. Finally, at step 5, under the assumption that the inclination angle is between $\theta_{min}$ and $\theta_{max}$, it is all right to say the model lies in the range between the the two coordinated models as shown in Fig. 4.8 (e) according to the conclusions drawn in section 3.3.2. Hence, we can say that we obtain a range estimation.

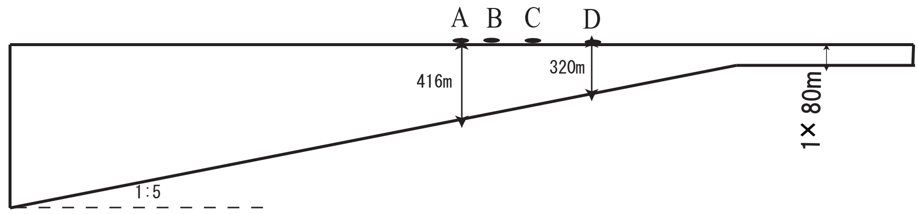


**Figure–4.9** The section profile designed for a 2D 2-layered inclined medium. There are one set of 4 sites in a line is the linear array we use to estimate the dispersion curve of the ground structure. The corresponding depth at A and D are 416m and 320m, respectively. The mesh size is still 80m and the wavefield is created to be diffuse in the same way as that in the former section. The inclination angle is $arctan(1/5)$.

**Table–4.1** The parameters of the 2-layered medium

| Layer | P-wave velocity [m/s] | S-wave velocity [m/s] | Density [t/m$^3$] | $tan\theta$ $\theta$: inclination angle |
|---|---|---|---|---|
| 1 | 800 | 600 | 1.5 | 1:5 |
| 2 | 1800 | 1200 | 2.0 | $\infty$ |

## 4.4 A numerical simulation for confirmation

Now it is time to confirm the methodology proposed in the former section using a FDM numerical simulation. The 2D 2-layered model and the medium property are shown in Fig. 4.9 and Table 4.1. There are one set of 4 sites in a line is the linear array we use to estimate the dispersion curve of the ground structure. The corresponding depth at A and D are 416m and 320m, respectively. The mesh size is still 80m and the wavefield is created to be diffuse in the same way as that in the former section. The inclination angle is $arctan(1/5)$.

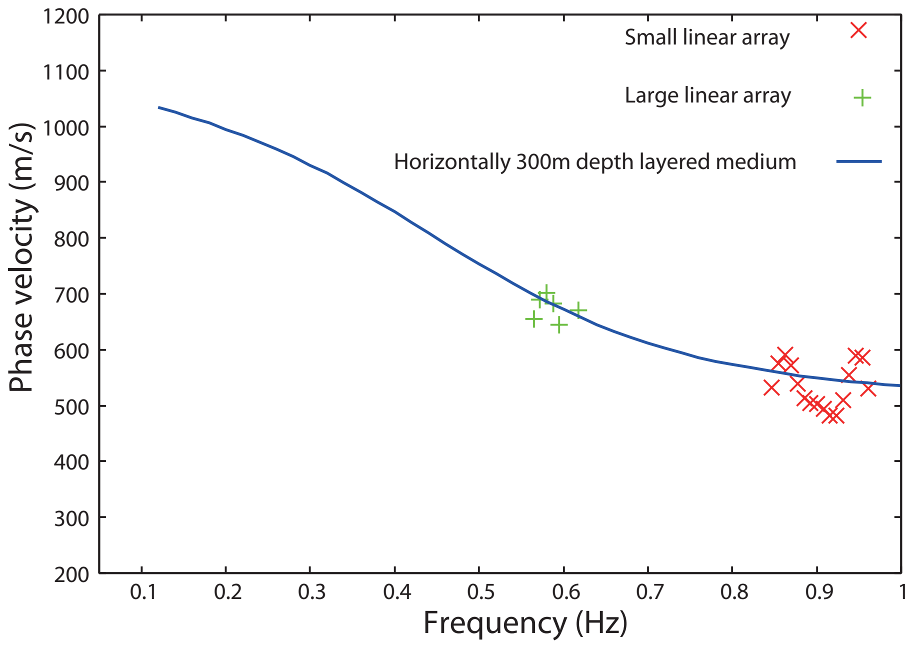


**Figure–4.10** The dispersion curve obtained using the linear array ABCD. The blue curve indicates the theoretical dispersion curve of horizontally layered medium with thickness of 300m. The red and green dots indicate the estimation from small and large linear array, ABC and BCD, respectively.

Now we confirm to the procedure designed in the former section. Firstly, we set the $\theta_{min}$ to be $arctan(1/30)$ and $\theta_{max}$ to be $arctan(1/3)$. Secondly, we apply the linear array method proposed in Chapter 2 to the ABC line and BCD line. And we coordinate the depth of the first layer's thickness to fit the theoretical dispersion curve to the estimations obtained from linear array method. As a result, the depth of 320m is found to be the optimal one, which means that a horizontally 2 layered medium with the first layer's thickness of 320m has a dispersion curve most matching with the estimations from simulation records as shown in Fig. 4.10. The blue curve indicates the theoretical dispersion curve of horizontally layered medium with thickness of 300m. The red and green dots indicate the estimation from small and large linear array, ABC and BCD, respectively. Hence, we suppose it to be a rough estimation of the first layer's thickness in the real inclined structure.

Thirdly, we set the two starting models. One is the model with inclination angle of $\theta_{max}$ and a relatively large depth at D, which we set to be 320m, almost the same as the rough estimation calculated just now. The other one is the model with inclination angle of $\theta_{min}$ and a relatively small depth at D, which we set to be 150m, around one half of the rough estimation. Then, we calculated the theoretical IOG between A and D under these two models using the numerical simulation, the same as in Chapter 3, to obtain the corresponding peak frequencies. Afterwards, we list the vertical spectral ratio between A and D from the simulation records with the two peak frequencies as shown in Figs. 4.11 and 4.12. Fig. 4.11 (a) indicates the model with $\theta_{max}$ and with relatively large depth and (b) indicates the model with $\theta_{min}$ and with relatively small depth. In fig. 4.12, the red vertical line indicates the minimum peak frequency produced from Fig. 4.11 (a) and the green vertical line indicates the maximum peak frequency produced from Fig. 4.11 (b). The red one shows the peak frequency from data which can be regarded as the objective peak frequency for fitting.

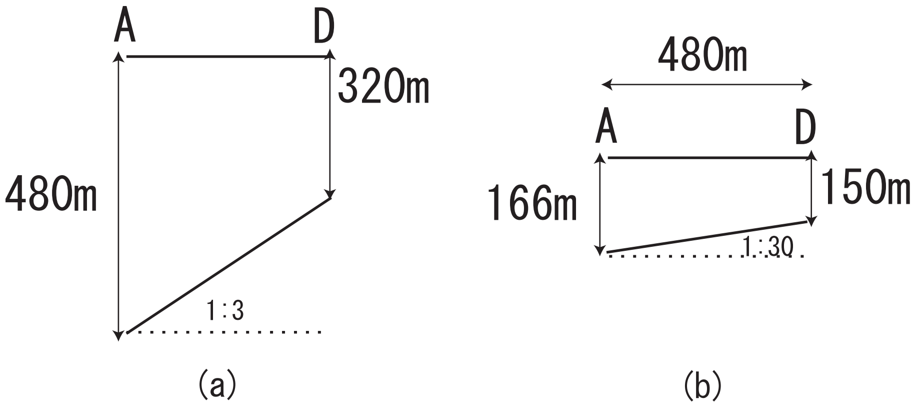


**Figure–4.11** The starting models. (a) indicates the model with $\theta_{max}$ and with relatively large depth and (b) indicates the model with $\theta_{min}$ and with relatively small depth.

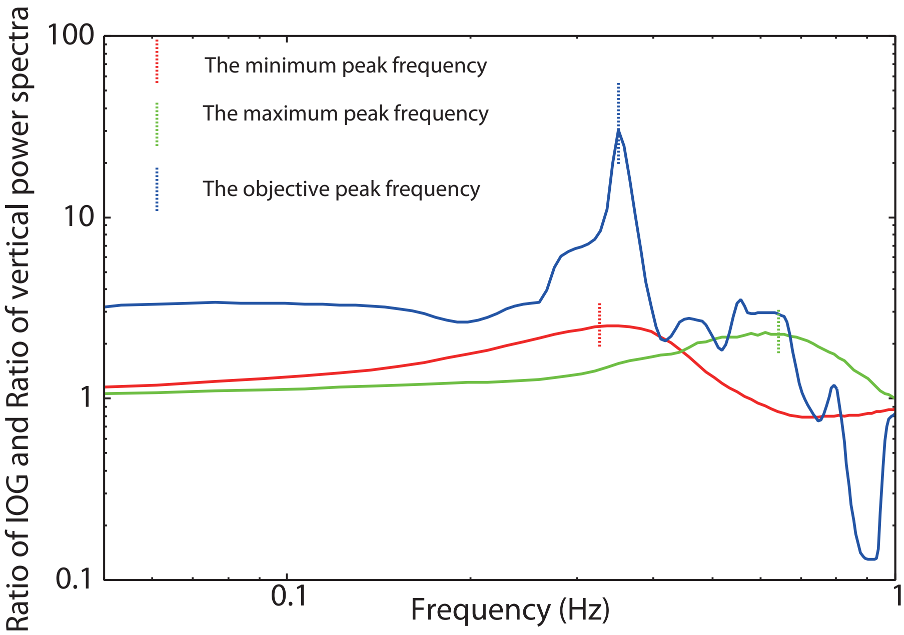


**Figure–4.12** The ratio of IOG and ratio of vertical power spectra. The red vertical line indicates the minimum peak frequency produced from Fig. 4.11 (a) and the green vertical line indicates the maximum peak frequency produced from Fig. 4.11 (b). The red one shows the peak frequency from data which can be regarded as the objective peak frequency for fitting.

Then, we use the two starting models and coordinate the depth of each model to fit for the objective frequency. And as a result, the final models is shown as Fig. 4.13. Fig. 4.13 (a) indicates the coordinated model with $\theta_{max}$ and with relatively large depth and (b) indicates the coordinated model with $\theta_{min}$ and with relatively small depth. The corresponding coordinated peak frequencies are shown in Fig. 4.14. The red vertical line indicates the coordinated peak frequency produced from the coordinated model in the upper part of Fig. 4.13 and the green vertical line indicates the coordinated peak frequency produced from the coordinated model in the lower part of Fig. 4.13. The red one shows the peak frequency from data which can be regarded as the objective peak frequency for fitting.

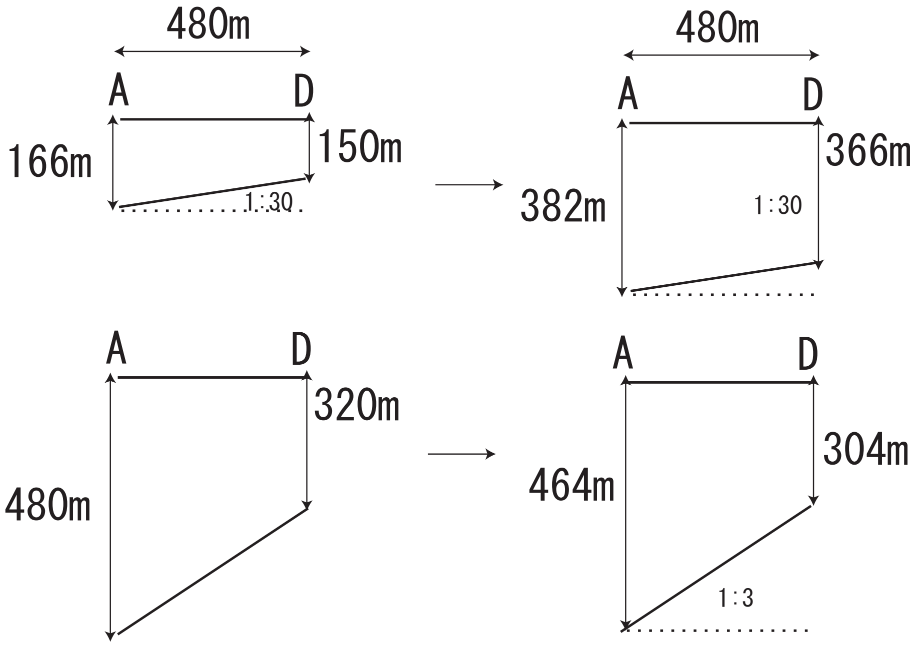


**Figure–4.13** The coordinated models. (a) indicates the coordinated model with $\theta_{max}$ and with relatively large depth and (b) indicates the coordinated model with $\theta_{min}$ and with relatively small depth.

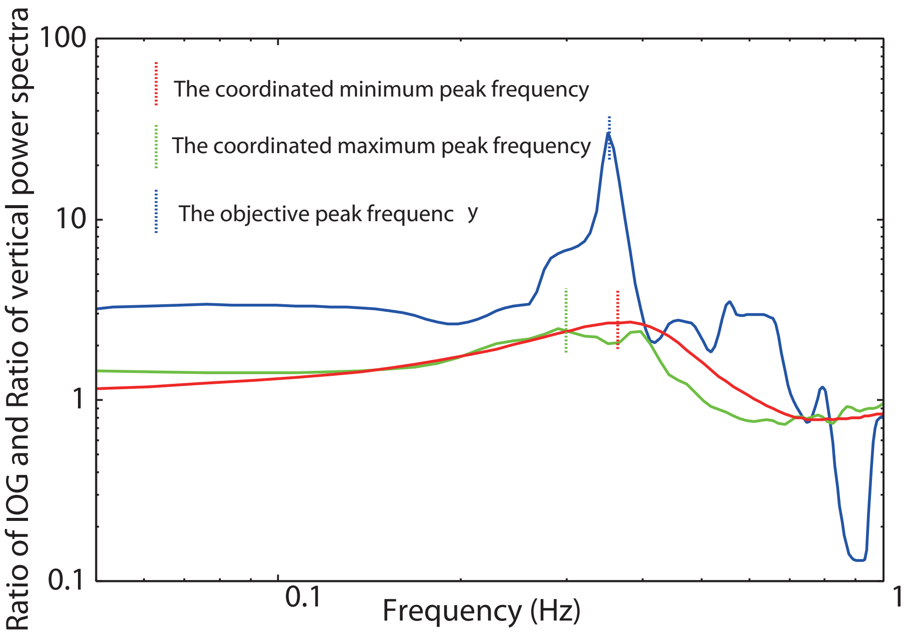


**Figure–4.14** The ratio of IOG and ratio of vertical power spectra. The red vertical line indicates the coordinated peak frequency produced from the coordinated model in the upper part of Fig. 4.13 and the green vertical line indicates the coordinated peak frequency produced from the coordinated model in the lower part of Fig. 4.13. The red one shows the peak frequency from data which can be regarded as the objective peak frequency for fitting.

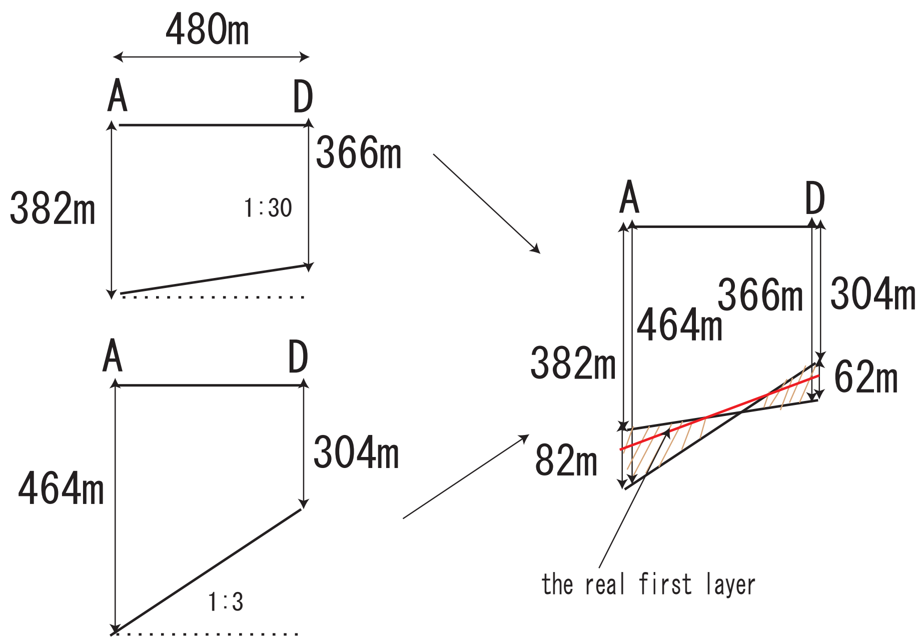


**Figure–4.15** The final range estimation. It is a combination from two coordinated models. The red line indicates the real first layer which has a depth of 416m at A and 320m at D.

The final range estimation is shown in Fig. 4.15. It is a combination from the coordinated models. It can be seen that the real structure: which is indicated by the depth at A and D of 416m and 320m as shown by the red line in Fig. 4.15 lies in the range of 382m to $382 + 82$m and 304m to $304 + 62$m. It is not accurate but a right range estimations. If we calculate the relative error of the range estimation $E_d^{re}$ at each site using the equation:

$$E_d^{re} = \frac{max\{|D - D_{max}|, |D - D_{min}|\}}{D}, \tag{4.1}$$

where $D$ indicates the real depth at site and the $D_{max}$ and $D_{min}$ indicate the upper limit and lower limit of the range estimation, respectively, the $E_d^{re}$ at A and D is to be 12% and 14%, respectively. Hence, we can preliminarily conclude that, through this numerical simulation, the range estimation technique can reach a relative error of 10% to 15% about the depth of first layer at one site of the 2D 2-Layered one-directionally inclined model.

## 4.5 Discussion

### 4.5.1 The reasons causing the technique to fail

In the numerical simulation we conducted just now, it seems like a successful combination of the linear array method and the seismic interferometry, which are detailed described in Chapter 2 and 3, respectively. However, there are several hidden unstable factor which may cause this combination to fail.

Firstly, let us pay attention to Figs. 4.10 and 4.12. It can be seen that the frequency range for us to estimate the rough thickness of first layer, about 0.5 to 1.0Hz, and the frequency range for picking up the peak frequency from the vertical spectral ratio, which is about 0.3 to 0.9Hz. The two ranges seem overlapping over each other. It is not to say that the two ranges must overlap to certain degree. However, it is actually indispensible for the two ranges to satisfy some conditions for the combination technique to succeed.

To be more exact, if we have two fixed sites $A$ and $D$ on the inclined 2D model, the frequency range of peak frequency, $[f_{p1}, f_{p2}]$, is of course decided by the inclination angle and the depth at $A$. Though peak frequency is a single value, we use a small range for the convenience for description. And if the linear array is also among $A$ and $D$, for example, a 3-site ABC array with B between A and D, the effective frequency range for estimation, $[f_{l1}, f_{l2}]$, is also decided by the real dispersion curve and distance between $A$ and $D$, $r_{AD}$. It doesnot matter where $[f_{p1}, f_{p2}]$ lies in because the peak frequency must exist and be significant to identify the inclination. However, the unproper $[f_{l1}, f_{l2}]$ would cause problem. For example, if the ground structure under $A$ and $D$ is a shallow inclined 2D model, but the $r_{AD}$ is not small enough causing $[f_{l1}, f_{l2}]$ to be relatively high frequency range so that impossible to identify the shallow first layer's thickness. This case would be shown in some real field data which would not be written in the thesis for some copyright related problem. I would demonstrate it in another way by presentation.

In the case we just described now, even though we make the $r_{AD}$ smaller to increase the identifying ability of the linear array method about the shallow structure, there is another potential problem that, if the inclination is a small one, too short $r_{AD}$ would cause a too small lateral heterogeneity, namely, the too small difference of the first layer's thickness between $A$ and $D$ so that the peak frequency range $[f_{p1}, f_{p2}]$ would be become invisible, even if it actually exists.

Another factor still lies in the rough estimation of first layer's thickness. The largest inclination angle whose applicability we have exmamined is $arctan(1/5)$ as Fig. 4.2 shows. However, it is possible that when the angle becomes larger, the estimation would be unavailable.

### 4.5.2 Clarification about wave type

The linear array method, introduced in Chapter 2, mainly uses the Rayleigh wave. The vertical spectral ratio, which is developed from SI, is applicable for full-wave type. As discussed in the former subsection, there is no requirement about the $[f_{p1}, f_{p2}]$ because any wave-type satisfies the vertical spectral ratio's theory. That is to say, no matter what $[f_{p1}, f_{p2}]$ the peak frequency lies in, it has the corresponding significance we have described very detailedly in Chapter 3. On the other hand, the wavetype in $[f_{l1}, f_{l2}]$ range is required to be surface wave, in vertical case, the Rayleigh wave.

If $[f_{l1}, f_{l2}]$ overlaps $[f_{p1}, f_{p2}]$ and the wavetype in $[f_{l1}, f_{l2}]$ ranges is mainly Rayleigh wave, which means the wave type vertical spectral ratios uses is also Rayleigh wave. It is, of cource, no problem because vertical spectral ratio is available for all wave types. When they overlap and the wave type contains both body wave and surface wave, the linear array method may fail. When they do not overlap and the wavetype in $[f_{l1}, f_{l2}]$ is mainly Rayleigh wave, the linear array method works. Even if the wave type in $[f_{p1}, f_{p2}]$ contains other types of wave, it does not matter because vertical spectral ratio is a full-wave theory. In a word to summarize above, no matter the two ranges overlap or not, the combination technique works as long as the wave type in $[f_{l1}, f_{l2}]$ is Rayleigh wave.

Normally, it is supposed that when the linear array is a relatively large scale one, surface wave is dominated in $[f_{l1}, f_{l2}]$ range so that linear array method works. However, the quantitative discussion remains a topic. After all, we know nothing before an observation. It is more meaningful to judge it using the real data case by case in the real field test.

### 4.5.3 The applicable scope

Hence, because of the resolution limit of both methods, the applicable scope of the combination technique is quite limited. Even qualitively, it can only be said that if the structure is very shallow and slightly inclined, it tends to be very difficult to apply it. After all, the applicability depends on the real field condition, the observation objective, the real 2D 2-layered model including the S wave velocity, thickness and inclination angle. For now with only one numerical simulation, we can only say that under the medium property of Table. 4.1, thickness of about 200 to 300m, the applicable inclination angle is under $arctan(1/5)$.

On the other hand, in case of slightly inclined shallow medium, it is difficult to use just one linear array to obtain a comprehensive range estimation as concluded above. Hence, we may do several linear observation at different area. The linear array is very environmentally friendly hence can be eligible for this. And similar process is conducted as described before. The only difference is that the ratio of power spectra is taken between sites from different linear arrays. The process is shown in Fig. 4.16. This is different from the proposed combination technique and cannot be said to be more applicable than H/V method or f-k method or SPAC methods. However, the significance lies in that it offers another choice of technique in real field observation.

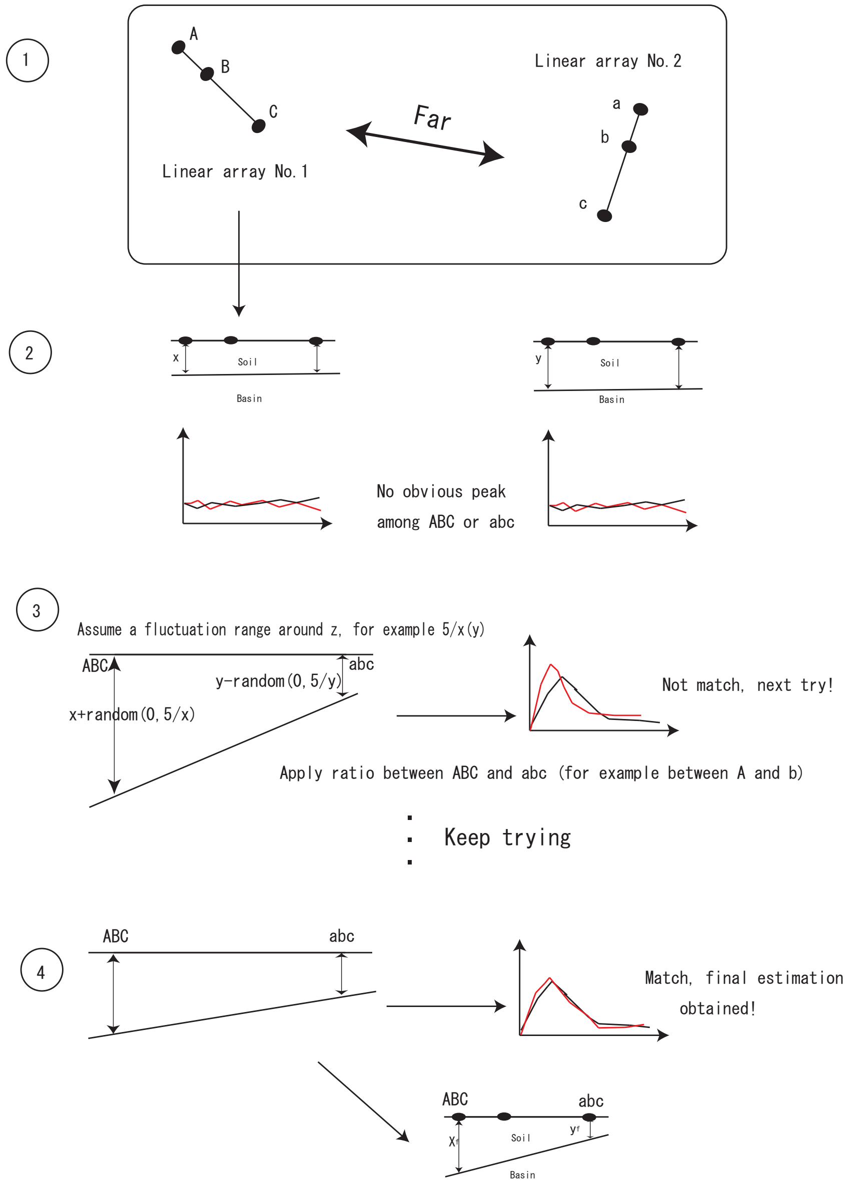


**Figure–4.16** The methodology constituted to estimate 2D model using several linear array in a slightly inclined case

## 4.6 Summary

In this chapter, we have proposed a new methodology based on the results obtained in chapter 2 and chapter 3. This can be applied flexibly in real observations. There are several conclusions drawn below.

- All the analysis are based on the simple assumption of (1) diffuse wavefield; (2) 2D unidirectionally layered medium. Though, it does not lose generality to the possible extensive research.

- Both in steeply inclined and slightly inclined medium, the linear estimation is able to give an acceptable initial estimation about the first layer's thickness for the next step's process.

- A technique for range estimation is proposed and a numerical simulation has been conducted to confirm the availability successfully with a relative error about the depth of 10% to 15%.

- The applicablity of the combination technique is decided by the real 2D model because of the resolution limit of linear array method and vertical spectral ratio. Qualitively, it is difficult to apply it in a shallow, slightly inclined 2D model.

- Under the condition of Table. 4.1 and thickness of about 300m and inclination angle under $arctan(1/5)$, the combination technique is available. It is, after all, the quantitative conclusion we can draw so far.

- If it is a slightly and shallow struture, we can conduct several small-scale linear arrays at different areas and apply the vertical spectral ratio between the sites in different arrays. It offers another choice of technique in real field observation.

# 5

# Conclusion

In order to do more improvement to the existing microtremor array method to make the array setting more flexible and make use of the same records more efficiently, we propose a linear array method and a new, significant perspective about the vertical component spectral ratio among two sites, respectively to make a new methodology to estimate 2D model structure with simple lateral heterogeneity. It not only has the advantage of normal array method of low cost and simpliness but also has more flexible array setting to conduct practically and has the ability to detect the possible inclination under ground. The whole research makes a good complement to the existing research about designing more convenient shape of array methods and the application of microtermor survey method in 3D ground structure.

In the part of linear array method, we proposed this method based on original SPAC method and CCF description. We showed that this method can work well in the most cases in an extremely azimuth-dependent wavefield and work very well and stably even in a not moderately azimuth-dependent wavefield. We did a lot of simulations to check the estimation under different form of linear array (number of sites, intervals) and under incoherent noise. We demontrated that the 3-site with up to $J_4$ term accuracy and with an inverval ratio of 2.0 to 2.5 has the best cost-performance in the $kr_{max}$ range of 1.3 to 2.8. Finally, we confirmed this using a field test. The result showed the stability behaviour of the linear array method. Compared to SPAC method, the accuracy is the almost the same but have narrower effective frequency range. We also demonstrated that the $J_0$ method, though it also seems using a simplified version of linear array, has the theoretical defect and cannot work stably in part kinds of wavefield.

Then, using seismic interferometry theory, we propose a new perspective of the vertical component ratio of power spectra between 2 sites in diffuse wavefield. Through theoretical analysis and numerical simulation, we confirmed there exists a peak frequency in the vertical component ratio of power spectra between two sites. It depends on the particular condition of lateral heterogeneity between 2 sites. In a simple unidirectionally inclined 2-layered medium in diffuse wavefield, the peak frequency depends simply on the difference of first layer's thickness and the average thickness of first layer. The peak frequency decreases as the difference of first layer becomes larger. Based on this, the peak frequency can be a good indicator of lateral heterogeneity by applying the equivalence with that from the ratio of IOG. It proves that in the condition of full wave and in complicated base model, it is better to use Green's function theory to interpret the spectral ratio between 2 sites. As a comparison, we also tried to interpret horizontal component ratio of power spectra using the ratio of transfer function of SH wave. It indicates the old concept based on 1D simple model cannot work well in a 3D case. As a whole, this chapter demonstrates a new interpretation of the vertical component ratio of power spectra and proves its potential of detecting lateral heterogeneity in a simple numerical simulation using the peak frequency.

Finally, we combined the concept of linear array method and vertical component spectral ratio to constitute a complete and reasonable methodology. We discussed the applicability of using linear array method to estimate a rough estimation dealing with inclined 2D layered medium. It is demonstrated that as the inclination angle becomes larger, it becomes complicated to obtain a reasonable dipersion curve. However, because we still have post-process using spectral ratio, it can be accepted as long as the dispersion curve can deduce to a deptp which is close to the average depth. Afterwards, a technique for range estimation about the 2-layered 2D model is proposed and a numerical simulation has been conducted to confirm the availability successfully with a relative error about the depth of 10% to 15%. It is discussed that the applicability of the proposed range estimation technique is limited by the resolution limit of both methods and influenced by the wave types used by linear array method and vertical spectral ratio. It requires the wave type in effective frequency range of linear array method to be mainly Rayleigh wave and it requires the same frequency range to be meaningful to estimating the corresponding objective depth range.

The technique tends to be unavailable in a slightly inclined shallow medium. In this case, we can use several linear arrays at different areas and take the ratios between sites from different arrays to make a large-scale inclination identification. Anyway, it is still difficult to judge until given a particular observation case. More quantitative discussion remains a topic.

# Acknowledgement

Thanks to my superviser Professor Morikawa for the instruction all the time. Thanks to Professor Yamanaka, Midorikawa, Furukawa, Matsuoka for the significant comments. Thanks to all the students in Morikawa Laboratory. Thanks to all my friends and my parents for the support all the way. Thanks to everyone who has been related with me.

# Reference


1) Asten, M.W. and Henstridge, J.D.: Array estimators and the use of microseisms for reconnaissance of sedimentary basins, *Geophysics*, **49**, 1828–1837, 1984.

2) Horike, M.: Inversion of phase velocity of long-period microtremors to the S-wave-velocity structure down to the basement in urbanized areas, *J. Phys. Earth*, **33**, 59–96, 1985.

3) Capon, J.: High-resolution frequency-wavenumber spectrum analysis, *Proc. IEEE*, **55**, 1408–1418, 1969.

4) Taner, M.T., Koehler, F. and Sheriff, R.E.: Complex seismic trace analysis, *Geophysics*, **80**, 73–97, 1969.

5) Niedell, N.S. and Taner, M.T.: Semblance and other coherence measures for multichannel data, *Geophysics*, **36**, 482–497, 1971.

6) Nakamura, Y.: A method for dynamic characteristics estimation of subsurface using microtremor on the ground surface, *Q. Rep. Railway Tech. Res. Inst.*, **30(1)**, 25–30, 1989.

7) Horike, M.: Estimation of phase-velocity and transfer-function of microtremor, *Zisin 2*, **33(4)**, 425–442, 1980.

8) Satoh, T., Kawase, H., Sato, T. and Pitarka, A.: Three-dimensional finite-difference waveform modeling of strong motions observed in the Sendai Basin, *Bull. Seismol. Soc. Am.*, **91(4)**, 812–825, 2001.

9) Lermo, J. and Chavez-Garcia, F.J.: Are microtremors useful in site response evaluation?, *Bull. Seismol. Soc. Am*, **84(5)**, 1350–1364, 1994.

10) Aki, K.: Space and time spectra of stationary stochastic waves, with special reference to microtremors, *Bull. Earthq. Res. Inst.*, University of Tokyo, **35**, 415–456, 1957.

11) Okada, H.: Microtremor survey method, *SEG Geophysical Monograph Series No. 12*, 2003.

12) Henstridge, J.D.: A signal processing method for circular arrays, *Geophysics*, **44**, 179-184, 1979.

13) Ikuo Cho, Taku Tada and Yuzo Shinozaki: A new method to determine phase velocity of Rayleigh waves from microseisms, *Geophysics*, **69**, 1535-1551, 2004

14) Ikuo Cho, Taku Tada and Yuzo Shinozaki: A generic formulation for microtremor exploration method using three-component records from a circular array, *Geophys. J. Int.*, **165**, 236-258, 2006

15) Garcia-Jerez, A., Luzon, F. and Navarro, M.: Computation of dispersion curves for Rayleigh and Love waves using horizontal components of seismic microtremor, *Proc. of the 8th U.S. Nat. Conf. on Earthquake Engineering*, 1377, 2006

16) Garcia-Jerez, A., Luzon, F. and Navarro, M.: An alternative method for calculation of Rayleigh and Love wave phase velocity by using three-component records on a single circular array without a central station, *Gephys. J. Int.*, **173** 844–858, 2008

17) Garcia-Jerez, A., Luzon, F. and Navarro, M.: Determination of elastic properties of shallow sedimentary deposits applying a spatial autocorrelation method, *Geomorphology*, **93** 74–88, 2008

18) Morikawa H., Sawada S. and Akamatsu J.: A method to estimate phase velocity of Rayleigh waves using microtremors simultaneously observed at two sites. *Bulletin of the Seismological Society of America*, **94**, 961-976, 2004

19) Louie, J.N.: Faster, Better: Shear-wave velocity to 100 meters depth from refraction microtremor arrays. *Bull. Seismol. Soc. Am.*, **91**, 347-364, 2001

20) Ohori, M., Nobata, A. and Wakamatsu, K.: A comparison of ESAC and FK methods of estimating phase velocity using arbitrarily shaped microtremor arrays, *Bulletin of the Seismological Society of America*, **92**, 2323-2332, 2002

21) Yokoi, T.. Hayashi, K. and Aoike, K.: A case study on dependence of the complex coherence function on the azimuth SPAC method of microtremor array measurement, *Proceeding of the 114th SEGJ Conference*, 138-141, 2006

22) Hayashi, K.: Effect of array shape on the spatial auto-correlation analysis of microtremor array measurements. *Proceedings of the symposium on the application of geophysics to engineering and environmental problems*, 616-625, 2009

23) Hayashi, K. and Kita, T.: Applicability of a spatial autocorrelation method (SPAC) using a linear array in comparison with triangular and L-shaped arrays. *Proceedings of the symposium on the application of geophysics to engineering and environmental problems*, 543-551, 2010

24) Shiraishi, H., Matsuoka, T. and Asanuma, H. Direct estimation of the Rayleigh wave phase velocity in microtremors. *Geophysical Research Letters*, **33**, L18307, 2006

25) Asten, M.W. On bias and noise in passive seismic data from finite circular array data processed using SPAC methods. *Geophysics*, **71**, V153-V162, 2006

26) Okada, H.: The efficient number of stations required by circular array for the spatial auto-correlation method applied to array observations of microtremors. *Exploration Geophysics*, **37**, BUTSURITANSA, 59, MULTI-TAMSA, 9, 73-85, 2006

27) Margaryan, S., Yokoi, T. and Hayashi, K.: Experiments on the stability of spatial autocorrelation method (SPAC) and linear array methods and on the imaginary part of the SPAC coefficients as an indicator of data quality. *Exploration Geophysics*, **40**, BUTSURITANSA, 62, MULTI-TAMSA, 12, 121-131, 2009

28) Chavez-Garcia F.J., Rodriguez M. and Stephenson W.R.: An alternative approach to the SPAC analysis of microtremors: Exploiting stationarity of noise. *Bulletin of the Seismological Society of America*, **95**, 277-293, 2005

29) Chavez-Garcia F.J., Rodriguez M. and Stephenson W.R.: Subsoil Structure using SPAC measurements along a line. *Bulletin of the Seismological Society of America*, **96**, 729-736, 2006

30) Nazarian, S. and Stokoe, K.H.: In situ shear wave velocities from spectral analysis of surface waves. *Proceedings of the World Conference on Earthquake Engineering*, **8**, San Francisco, Calif, 1984 July 21-28.

31) Park, C.B., Miller, R.D. and Xia, J.: Multi-channel analysis of surface waves. *Geophysics*, **64**, 800-808, 1999

32) Toshiaki, Yokoi and Sos Margaryan: Consistensy of the spatial autocorrelation method with seismic interferometry and its consequence, *Geophysical Prospecting*, **56**, 435-451, 2008

33) Sánchez-Sesma, F.J.: A theory for microtremor H/V spectral ratio: Application for a layered medium, *Geophysical Journal International*, 2011

34) Gouedard, P., Cornou, C. and Roux, P.: Phase-velocity dispersion curves and small-scale geophysics using noise correlation slantstack technique. *Geophys, J. Int*, **172(3)**, 971-981, 2008

35) Chavez-Garcia F.J., Manakou, M.V. and Raptakis, D.G.: Subsoil structure and site effects: A comparison between results from SPAC and HVSR in sites of complex geology. *Soil Dynamics and Earthquake Engineering*, **57**, 133-142, 2014

36) Mastushima, S., Hirokawa, T., Martin, F.D., Kawase, H. and Sanchez-Sesma, F.J.: The effect of lateral heterogeneity on Horizontal-to-Vertical Spectral Ratio of Microtremors Inferred from Observation and Synthetics.*Bulletin of the Seismological Society of America*, **104(1)**, 381-393, 2006

37) Tada, T., Cho, I. and Shinozaki, Y.: New circular-array microtremor techniques to infer love-wave phase velocity. *Bulletin of the Seismological Society of America*, **99(5)**, 2912-2926, 2009

38) Okada, H. and Matsushima, T.: An exploration method using microtremors (1)–A theory to identify Love waves in microtremors. *Proc. of the 81st SEGJ Conference*, 15-18, 1989

39) Matsushima, T. and Okada, H.: An exploration method using microtremors (2)– An experiment to identify Love waves in long-period microtremors. *Proc. of the 82st SEGJ Conference*, 5-8, 2010

40) Tada, T., Cho, I. and Shinozaki, Y.: A two-radius circular array method: Inferring phase velocities of Love waves using microtremor records. *Geophys. Res. Lett*, **33**, L10303, 2006

41) Tada, T., Cho, I. and Shinozaki, Y.: Beyond the SPAC method: Exploiting the wealth of circular-array methods for microtremor exploration. *Bulletin of the Seismological Society of America*, **97**, 2080-2095, 2007

42) Yokoi, T.: New formulas derived from seismic interferometry to simulate phase velocity estimates from correlation methods using microtremor. *Geophysics*, **75(4)**, SA71-SA83, 2010

43) Tokimatsu, K.: Geotechnical site characterization using surface waves. *Earthquake geotechnical engineering: Balkema*, 1333-1368, 1997

44) Asten, M.: The spatial auto-correlation method for phase velocity of microseisms: Another method for characterization of sedimentary overburden. *Earthquake code in the real world: Proceeding of the Australian Earthquake Engineering Society*, Paper 28, 2001

45) Feng, S., Sugiyama, T., Horikawa, H. and Yamanaka, H.: Multi-mode phase velocity inversion with reference to medium response. *Proceedings of the 14th SEG Japan Conference*, 27-30, 2006

46) Asten, M.: Site shear velocity profile interpretation from microtremor array data by direct fitting of SPAC curves. *Third International Symposium on the Effects of Surface Geology on Seismic Motion*, **2**, 1069–1080, 2009

47) Weaver, R.L. and Lobkis, O.I.: Ultrasonics without a source: Thermak fluctuation correlations at MHz frequencies. *Phys. Rev. Lett.*, **87**, 134301, 2001

48) Campillo, M. and Paul, A.: Long-range correlations in the diffuse seismic code. *Science*, **299**, 547-549, 2003

49) Wapenaar, K.: Retrieving the elastodynamic Green's function of an arbitrary inhomogeneous medium by cross correlation. *Physical Review Letters*, **93**, 254301, 2004

50) Wapenaar K. amd Fokkema J.: Green's function representations for seismic interferometry. *Geophysics*, **71**, SI33-SI46, 2006

51) Sánchez-Sesma, F.J., Perez-Ruiz, J.A., Campillo, M. and Luzon, F.: Elastodynamic 2D Green's function retrieval from cross-correlation: Canonical inclusion problem. *Geophysical Research Letters*, **33**, L13305, 2006.

52) Sánchez-Sesma, F.J. and Campillo, M.: Retrieval of the Green's function from cross correlation: The canonical elastic problem, *Bulletin Seismological Society of America*, Vol. 96, No. 3, pp.1182–1191, 2006.

53) Sánchez-Sesma, F.J., Pérez-Ruiz, J.A., Luzón, F., Campillo, M. and Rodríguez-Castellanos, A.: Diffuse fields in dynamic elasticity, *Wave motion*, **45**, 641-654, 2008

54) Snieder, R.: Extracting the Green's function from the correlation of coda waves: A derivation based on stationary phase. *Physics Review*, **E69**, 254301, 2004

55) Perton, M., SanchezSesma, F.J., Rodriguez-Castellanos, A., Campillo, M. and Weaver, R.L.: Two perspectives on equipartition in diffuse elastic fields in three dimensions. *J. Acoust. Soc. Am*, **126**, 1125-1130, 2009

56) Tsai, V.C. and Moschetti, M.P.: An explicit relationship between time-domain noise correlation and spatial autocorrelation (SPAC) results. *Geophys. J. Int*, **172(1)**, 293–301, 2010

57) Li, M., Pang, B., He, Y. and Nian, F.: Particle filter improved by genetic algorithm and particle swarm optimization algorithm. *Journal of Software*, **8(3)**, 666–672, 2013

58) Sakai, K.: A method to estimate ground structure with high accuracy applying the combination of microtremor data and gravity data

59) Kennedy, J. and Eberhart, R.: Particle swarm optimization. *Proc of the IEEE Int Conf on Neural Networks*, Piscataway: IEEE Service Center, 1941-1948, 1995.

60) Wapenaar, K., Draganov, D. and Robertson J.: Introduction to the supplement on seismic interferometry. *Geophysics*, **71**, SI1eSI 4., 2006

61) Kawase, H., Sanchez-Sesma, F.J. and Matsushima. S.: The optimal use of horizontal-to-vertical ratios of earthquake motions for velocity inversions based on diffuse field theory for plane wave. *Bull. Seismol. Soc. Am.*, **101(5)**, 2001–2014, 2011

62) Paul, A., Campillo, M., Margarin, L., Larose, E. and Derode, A.: Empirical synthesis of time-asymmetrical Green function from the correlation of code waves. *J. Geophys. Res.*, **110**, doi: 10.1039/2004JB003521, 2005

63) Hisada, Y.: Efficient method for computing Green's functions for a layered half-space with sources and receivers at close depths. *Bull. Seismol. Soc. Am.*, **84(5)**, 1456, 1994

64) Hisada, Y.: Efficient method for computing Green's functions for a layered half-space with sources and receivers at close depths (Part 2). *Bull. Seismol. Soc. Am.*, **85(4)**, 1080, 1995

65) Kanai, K., and Tanaka, T.: Measurement of the microtremor. *Bull. Earthquake Res. Inst.*, **32**, 199–209, 1954

66) Kagami, H., Okada, S., Shiono, K., Oner, M., Dravinski, M., and Mal, A.K.: Observation of 1 to 5 second microtremors and their application to earthquake engineering.

Part Ⅲ. A two-dimensional study of site effects in S. Femando valley. *Bull. Earthquake Res. Inst.*, **76**, 1801–1812, 1986

67) Pitaka, A.: 3D elastic finite-difference modeling of seismic motion using staggered grids with nonuniform spacing. *Bull. Earthquake Res. Inst.*, **89**, 54–68, 1999

68) Sakai, Y..:Assess seismic response in high-frequency range of Kyoto Basin using finite difference method, 2001

69) Charles, C., Kosloff, D., and Kosloff, R., and Reshef, M.: A nonreflecting boundary condition for discrete acoustic and elastic wave equations. *Geophysics*, **50**, 705–708, 1985

70) Lavander, A.R.: Fourth-order finite-difference P-SV seismograms. *Geophysics*, **53**, 1425–1436, 1988

71) Cornou, C., Ohrnberger, M., Boore, D.M., Kudo, K., and Bard, P.-Y.: Derivation of structural models from ambient vibration array recordings: results from an international blind test. *Jounal of Software*, **8(3)**, 666–672, 2013

72) Coutant, O., Virieux, J., and Zollo, A.: Numerical source implementation in a 2D Finite Difference Scheme for Propagation. *Bull. Seism. Soc. Am.*, **85**, 1507–1512, 1995